STRUCTURE AND FACETING OF LOW-SYMMETRY METAL SURFACES

BY

DONALD ALAN WALKO

B.S., Cornell University, 1993

M.S., University of Illinois at Urbana-Champaign, 1994

THESIS

Submitted in partial fulfillment of the requirements

for the degree of Doctor of Philosophy in Physics

in the Graduate College of the

University of Illinois at Urbana-Champaign, 2000

Urbana, Illinois

STRUCTURE AND FACETING OF LOW-SYMMETRY METAL SURFACES

Donald Alan Walko, Ph.D.
Department of Physics
University of Illinois at Urbana-Champaign, 2000
Ian K. Robinson, Advisor

X-ray diffraction has, within the past two decades, developed into a powerful analytical tool for determining the atomic structure of crystalline surfaces. The dual advantages of high intensity and high resolution have made this technique thrive at synchrotron radiation sources. The experiments in this thesis extend surface x-ray diffraction to metal surfaces with particularly low symmetry: the multilayer surface structure of α-Ga(010), complicated by the low symmetry of the bulk, and Cu(115), a regularly stepped surface which spontaneously facets when exposed to oxygen. The equations describing surface x-ray diffraction are derived, with attention paid to assumptions made during the derivation and limitations of the technique. In particular, the theory of scattering from a rough surface is generalized to permit various models of roughness. The surface diffraction chamber in which these experiments were performed is briefly described, along with the load lock which allows samples to be inserted without opening the entire vacuum chamber to atmosphere.

We have determined the surface structure of α-Ga(010) near its melting point using x-ray diffraction. Due to the low symmetry of the α-Ga bulk structure, two distinct bulk truncations of the (010) surface are possible. Of these two ways, we find the true surface is formed by cutting through dimer bonds (i. e., between metallic bilayers). The contraction of the metallic bonds and expansion of the covalent bonds at the surface imply that the surface is more metallic than the bulk. Our results suggest that α-Ga is fundamentally composed not of Ga_2 dimers, but of corrugated metallic bilayers which can be modeled as deltahedral clusters.

Cu(001) vicinal surfaces facet when exposed to O. We have studied this process on Cu(115), which transforms from a clean surface to 104 and 113 facets, using surface x-

ray diffraction. Unlike α-Ga(010), the low symmetry of these surfaces is due to their high Miller indices, i. e., the stepped nature of the surfaces. The Cu(115) surface exhibits a complex interlayer relaxation accounted for by basic elasticity theory; the vertical displacements of the three surface atoms correlate to those of the subsurface atoms directly below. The O/Cu(104) facets do not, as previously proposed, involve any missing Cu rows, but the top three rows are expanded away from the bulk; the Cu–O chains which stabilize this surface are similar to those present on other O on Cu reconstructions. A complete structure determination was not possible for the O/Cu(113) facets, due to significant disorder, but an unambiguous (3×1) reconstruction was observed.

Besides being instrumental in determining the static structure of surfaces and facets, surface x-ray diffraction allows us to noninvasively observe, *in situ*, the evolution of the faceting surface. We find that the faceting is driven by the formation of O/Cu(104) facets: O exposure induces spinodal decomposition of the (115) surface into (104) and (014) facets, which form spontaneously, and also disordered, stepped facets, whose orientation gradually changes from (115) to (113) as the (104) facets grow. We identify three temperature regimes which have qualitatively different faceting processes, shedding light on the temperature dependence of the equilibrium crystal shape for part of the O-covered Cu system. During the faceting process, the time evolution follows a slow dynamic scaling behavior, consistent with either a logarithmic or power-law dependence.

Throughout this thesis, comparisons are made with results obtained by other surface-sensitive techniques. The complimentarity of these techniques is worth emphasizing; despite the power of surface x-ray diffraction in solving crystal structures, its ability to interpret and explain the properties of these surfaces is greatly enhanced by microscopy, spectroscopy, and other diffraction techniques, as well as theoretical and numerical studies.

To my parents

and to Lynnette.

Acknowledgments

First of all, I would like to thank God for creating, redeeming, and sustaining our world, and for allowing us to explore some small portion of it.

While I would like to thank all my family and friends, who have all, in large or small ways, contributed to this thesis, I would particularly like to mention some of the most important teachers in my life: Mrs. Harold and Mrs. Schaffer, for giving me a great start to my schooling; John Sitterly, for introducing me to the challenge of physics; Ralph Enokian; my sister Karen Walko, who taught me that not everyone learns math and science the same way; and Dr. Eliot Specht, Dr. Cullie Sparks, Dr. Rodney McKee, Dr. Fred Walker, Dr. Sarvjit Shastri, Dr. Ken Finkelstein, Dr. Qun Shen, and Prof. Boris Batterman, for their patience as I began my career as an experimentalist.

Somewhere along the line, the distinction between teacher and collaborator fades, and I am grateful to those I have worked with and learned from. Foremost among these is my advisor, Prof. Ian Robinson; I am thankful for his patience, insight, dedication, and sailboat piloting skills. I also acknowledge my fellow group members for the help they have been to me: Dr. Kevin Whiteaker, Dr. Yong Chu, Dr. Chinkyo Kim, Dr. Jeff Libbert, Dr. David Fanning, Dr. John Pitney, Dr. Odile Robach, Curt Benson, and also quasi-group member Dr. Ken Ritley. I would like to thank E. Tosatti for suggesting the problem of the α-Ga(010) surface structure and for helpful discussions. I am particularly grateful to Christian Grütter and Jörg H. Bilgram for supplying the Ga crystals which made Chapter 2 possible.

Thanks are also due to Holger Meyerheim for supplying the Cu(115) crystal used in the experiments of Chapters 3 and 4. We thank D. P. Woodruff, K. A. R. Mitchell, and Elias Vlieg for discussions on the O/Cu(104) problem. Bill Lenhard has been a wonderful technical resource while I've worked at Brookhaven. The skills of Bill Thrasher, Spencer Schultz, and Alex Noszko were instrumental in the construction of the load lock. I am glad Prof. Peter Bennett, Dr. Paul Partyka, and Glenn Glass have let me participate in their experiments with them. Computer support from Virginia Metze and the MRLCFC was essential, but probably underappreciated. Finally, I would like to thank the other UIUC physics grads with whom I struggled through the first year: Tushar Mandrekar, Dr. Raj Shah, Dr. Dohn Arms, Britt Plourde, Balijeet Bains, and Craig Milling.

This research was supported for two years by the National Science Foundation under grant DMR 93-15691, and for one year by the University of Illinois Materials Research Laboratory under DOE DEFG02-96ER45439. I received a Graduate Assistantship in Areas of National Need for the 1996-1997 school year, in support of this research. The NSLS, where the experiments described in this thesis were performed, is supported by the U. S. Department of Energy under Grant No. DE-AC02-98CH10886.

Table of Contents

Chapter

1 Scattering of x rays by surfaces . . . 1

1.1 Surface x-ray diffraction . . . 1

1.1.1 Scattering from electrons and atoms . . . 1

1.1.2 Scattering from a bulk crystal . . . 3

1.1.3 Scattering from a crystal surface . . . 5

1.1.4 Scattering from a rough surface . . . 8

1.1.5 Thermal vibrations . . . 13

1.2 Experimental set-up . . . 14

1.2.1 Diffraction chamber . . . 14

1.2.2 Design and use of load lock . . . 17

2 Surface structure of α-Ga(010) . . . 21

2.1 Introduction . . . 21

2.1.1 Bulk α-Ga structure . . . 22

2.1.2 Previous work on α-Ga(010) . . . 25

2.2 Experiment and results . . . 26

2.2.1 Experimental set-up . . . 26

2.2.2 Results . . . 26

2.2.3 Discussion . . . 32

3 Structure of Cu(115): Clean surface and O-induced facets 34
3.1 Introduction 34
3.2 Clean Cu(115) surface structure 38
3.2.1 Previous work on Cu(115) 41
3.2.2 Present experiment and results 44
3.3 Structure of O/Cu(104) facets 48
3.3.1 Previous work on O/Cu(104) 48
3.3.2 Present experiment and results 50
3.4 Structure of O/Cu(113)(3×1) facets 56
3.4.1 Previous work on O/Cu(113) 56
3.4.2 Present experiment and results 57
3.5 Conclusion 62
4 O-induced spinodal decomposition of Cu(115) 64
4.1 Introduction 64
4.2 Background: Wulff plot and equilibrium crystal shape 66
4.3 Experimental method 69
4.4 Faceting observed by x-ray diffraction 70
4.4.1 Early stages of facet formation 70
4.4.2 Medium-temperature facet formation 74
4.4.3 High-temperature facet formation 76
4.4.4 Low-temperature facet formation 76
4.4.5 Reversal of faceting 77
4.5 Stability and evolution of facets 78
4.5.1 Equilibrium surface free energies of facets 78
4.5.2 Dynamic scaling of facet growth 82

References 90

Vita 97

List of Tables

1.1 n_{layers} for several surfaces, including those considered in this thesis. 7

1.2 Forms for various roughness models. 10

2.1 In-plane and interlayer displacements from bulk for one domain of our model of α-Ga(010), a relaxation of surface B, with $\chi^2 = 2.43$. 32

3.1 Interlayer relaxations of Cu(115). 42

3.2 Refined parameters for the physically realistic model of Cu(115), as described in the text, yielding $\chi^2 = 1.40$. 47

3.3 Refined parameters for O/Cu(104) surface structure, resulting in $\chi^2 = 5.5$. . 53

3.4 O–Cu bond lengths for the two O adsorption sites on Cu(104), with uncertainties of about 0.04 Å, based on refined atomic coordinates (Table 3.3). . 56

List of Figures

1.1 Probability distribution functions for the geometric, Poisson, and binomial distributions (symbols: $\diamond$, $+$, $\times$ respectively). 11

1.2 Top view of Bell Labs/Illinois surface diffraction chamber installed on beamline X16A of the NSLS. 16

1.3 Sectional view of load lock installed on X16A surface chamber. 20

2.1 Bulk structure of α-Ga, showing the seven nearest-neighbor bonds for one of the atoms. 23

2.2 Structure factors of the ten crystal truncation rods measured. 27

2.3 Layer-by-layer dissection of our model for the α-Ga(010) surface structure. . . 30

2.4 Nearest-neighbor atom separations classified by bond type (as defined in Fig. 2.1) versus depth from surface. 31

3.1 Schematic real-space model of one faceted pyramid. 37

3.2 A cross-section through reciprocal space above the $(603)_{115}$ bulk point, at $\ell = 4$. 38

3.3 Bulk-truncated structure of a clean, ideal fcc(115) surface. 39

3.4 Reciprocal space map for an fcc(115) surface, in the $k = 0$ plane. 41

3.5 Structure factors of the five crystal truncation rods of clean Cu(115). 45

3.6 Structure factors of the five CTRs of O/Cu(104) facets. 52

3.7 a) Plan and b) side views of refined O/Cu(104) surface structure. 54

3.8 a-d) Structure factors of the four CTRs of O/Cu(113) facets. 59

3.9 Structure factors measured along third-order rods from O/Cu(113)(3×1) facets. 60

3.10 Side view of refined O/Cu(113)((3×1) surface structure. 62

4.1 Sample Wulff construction, showing the surface free energy vs. orientation (outer, thinner line) and the resulting equilibrium crystal shape (inner, thicker line). 67

4.2 Selected scans through (11n) facet CTRs during faceting, for three representative temperatures. 71

4.3 Plots of a) elapsed time and b) O_2 dose at which faceting began, which turns out to be a dose of 9.6 L. 73

4.4 Positions of (11n) facets shown in Fig. 4.2 during dosing. 75

4.5 Proposed Wulff plots for the O on Cu system around the (115) orientation. . 81

4.6 Projected area of (104) facets vs. O_2 exposure, for several dosing experiments in the middle- and high-temperature regimes. 86

4.7 Variation of intensity from a point on a O/Cu(104) CTR during O_2 dosing, during experiments in the low- and middle-temperature regimes. 88

X rays are a hoax.

— *Lord Kelvin*

Chapter 1

Scattering of x rays by surfaces

1.1 Surface x-ray diffraction

1.1.1 Scattering from electrons and atoms

Surface x-ray diffraction depends on the elastic scattering of x rays by electrons. For incident radiation of amplitude A_0, the amplitude of scattered light by an electron (of charge $-e$ and mass m at position $\mathbf{r}$) is given by the classical Thompson formula [1]:

$$A = A_0 \frac{e^2}{mc^2 R} \exp(+i\mathbf{k_i} \cdot \mathbf{r} - i\mathbf{k_f} \cdot \mathbf{r}) = A_0 \frac{e^2}{mc^2 R} \exp(-i\mathbf{q} \cdot \mathbf{r}), \tag{1.1}$$

where R is the (large) distance from the electron to the detector, $\mathbf{k_i}$ and $\mathbf{k_f}$ are the incident and exit wavevectors, respectively, and $\mathbf{q}$ is their difference. That is, $|\mathbf{k_i}| = |\mathbf{k_f}| = \frac{2\pi}{\lambda}$, and $|\mathbf{q}| = \frac{4\pi \sin(2\theta/2)}{\lambda}$, where 2θ is the scattering angle. The amplitude has, in general, a complex value; it can be multiplied by $e^{i\psi}$, with ψ any arbitrary phase factor (equivalent to changing the origin of $\mathbf{r}$). An experiment will only measure the intensity (the square modulus of the amplitude).

Given the small value of $\frac{e^2}{mc^2 R}$, x-ray scattering from a single electron is relatively weak compared to electron-electron scattering, with the simplifying result that surface x-ray diffraction fits completely within the kinematic (single-scattering) approximation; dynamical scattering is only relevant very near three-dimensional Bragg diffraction spots of "perfect" crystals. Conversely, x-ray scattering from an electron is roughly three orders of magnitude greater than scattering from a nucleus (through the ratio of the proton to electron masses); nuclear x-ray scattering is thus completely negligible in all but certain specific resonant conditions.

Within the kinematic approximation, the amplitude of light scattering from two electrons is simply the sum of the amplitudes of the scattering from the individual electrons:

$$\begin{aligned} A_{1+2} = A_1 + A_2 &= A_0 \frac{e^2}{mc^2 R} \Big(\exp(-i\mathbf{q}\cdot\mathbf{r_1}) + \exp(-i\mathbf{q}\cdot\mathbf{r_2}) \Big) \\ &= A_0 \frac{e^2}{mc^2 R} \Big(1 + \exp(-i\mathbf{q}\cdot(\mathbf{r_1} - \mathbf{r_2})) \Big) \exp(-i\mathbf{q}\cdot\mathbf{r_2}). \end{aligned} \tag{1.2}$$

By factoring out $\exp(-i\mathbf{q}\cdot\mathbf{r_2})$, Eq. 1.2 emphasizes the importance of $\mathbf{r_1} - \mathbf{r_2}$, the path length difference between the two electrons, on the scattering amplitude.

Scattering from multiple electrons is calculated similarly, by summing the amplitudes of scattering from each individual electron. If the electrons cannot be treated as point particles, then the summation becomes an integral over the number density $\rho\,(\mathbf{r})$:

$$A = A_0 \frac{e^2}{mc^2 R} \int \rho\,(\mathbf{r}) e^{(-i\mathbf{q}\cdot\mathbf{r})}\, d^3\mathbf{r}. \tag{1.3}$$

$\int \rho\,(\mathbf{r}) d^3\mathbf{r}$ is the total number of electrons in the system, while $-e\rho\,(\mathbf{r})$ is the charge density of the electron distribution. Eq. 1.3 shows that A and $\rho\,(\mathbf{r})$ are related by a Fourier transform.

From Eq. 1.3, the amplitude of scattering from an atom of electron density $\rho_Z\,(\mathbf{r})$ directly follows. The atomic form factor f_0 is Eq. 1.3 without the prefactors:

$$f_0(\mathbf{q}) = \int \rho_Z\,(\mathbf{r}) e^{(-i\mathbf{q}\cdot\mathbf{r})}\, d^3\mathbf{r}. \tag{1.4}$$

Form factors have been calculated (usually assuming spherical symmetry) and tabulated for the elements [2] , as have been the coefficients of an analytical approximation: [2]

$$f_0(\mathbf{q}) = \sum_{i=1}^{4} a_i \, \exp(-b_i \, \mathbf{q}^2/16\pi^2) \; + \; c. \tag{1.5}$$

If the incident x ray's energy is near that of an absorption edge for an atom, resonant effects may become important and additional terms must be added to Eq. 1.4 [1, 3]:

$$f(\mathbf{q}, E) = f_0(\mathbf{q}) + f'(E) + i\, f''(E). \tag{1.6}$$

The resonant terms $f'(E)$ and $f''(E)$ are weakly $\mathbf{q}$-dependent, and vary slowly except near edges. Values for the resonant terms have been tabulated for free atoms in the dipole approximation, but in condensed matter the values may change significantly near edges, due to the presence of nearby atoms (and may also vary with polarization and orientation). This effect is exploited in techniques such as EXAFS, XANES, and DAFS, but most surface diffraction work attempts to avoid the complications of resonant effects by choosing energies far from absorption edges (ideally, the x-ray energy is below the edge to minimize fluorescence). However, resonant scattering at interfaces has been used by by Specht and Walker to determine the registry [4] and charge state [5] of interfacial atoms, and Chu *et al.* [6] used surface resonant scattering to determine the charge state of Pt(111) atoms undergoing surface anodic oxidation.

X-ray magnetic scattering is possible for atoms with a net spin (or angular momentum). Again, this effect is much weaker than the typical case of charge scattering, but can be extremely enhanced near absorption edges and with elliptically polarized radiation. Recent experiments have observed magnetic scattering at the $UO_2(001)$ [7] and $Co_3Pt(111)$ [8] surfaces.

1.1.2 Scattering from a bulk crystal

A crystal, simply defined, is a lattice with a basis. The electron density of a crystal is just that of the unit cell (the basis) convoluted with an array of delta functions (the lattice) in real space:

$$\rho_{crystal}(\mathbf{r}) \;=\; \rho_{cell}(\mathbf{r}) \otimes \sum_{n_1,n_2,n_3=-N}^{+N} \delta(\mathbf{x} - n_1\mathbf{a})\,\delta(\mathbf{y} - n_2\mathbf{b})\,\delta(\mathbf{z} - n_3\mathbf{c}). \tag{1.7}$$

($\mathbf{a}$, $\mathbf{b}$, and $\mathbf{c}$ are the lattice parameters of the crystal.) The scattered amplitude from the crystal is the Fourier transform of Eq. 1.7, i. e., the transform of the electron density of the cell multiplied by that of the lattice.

The Fourier transform of the unit cell is called the structure factor. If the j atoms of the cell are located at $\mathbf{r_1}, \mathbf{r_2}, \ldots \mathbf{r_j}$ (relative to the origin of the unit cell), then the structure factor $F(\mathbf{q})$ can be reexpressed in terms of the atomic positions and form factors:

$$\begin{aligned} F(\mathbf{q}) &= \int_{cell} \rho_{cell}(\mathbf{r})\, e^{-i\mathbf{q}\cdot\mathbf{r}}\, d^3\mathbf{r} \\ &= \sum_{n=1}^{j} f_n(\mathbf{q})\, e^{-i\mathbf{q}\cdot\mathbf{r}}\, d^3\mathbf{r}_n. \end{aligned} \tag{1.8}$$

Each sum of delta functions in Eq. 1.7 Fourier transforms into sums of phases:

$$\begin{aligned} \mathcal{FT}\left(\sum_{n_1=-N_x}^{+N_x} \delta(\mathbf{x} - n_1\mathbf{a})\right) &= \sum_{n_1=-N_x}^{+N_x} \exp\left(-in_1\, \mathbf{q}\cdot\mathbf{a}\right) \\ &= \frac{\exp\left(i\, N_x\, \mathbf{q}\cdot\mathbf{a}\right) - \exp\left(-i\, N_x\, \mathbf{q}\cdot\mathbf{a}\right)}{1 - \exp\left(-i\mathbf{q}\cdot\mathbf{a}\right)}. \end{aligned} \tag{1.9}$$

The diffracted intensity, an observable quantity, is proportional to the square modulus of Eq. 1.9. This is the N-slit interference function,

$$\frac{\sin^2\left(N_x\, \mathbf{q}\cdot\mathbf{a}\right)}{\sin^2\left(\mathbf{q}\cdot\mathbf{a}/2\right)}, \tag{1.10}$$

which becomes sharply peaked for large N_x. Eq. 1.10 has maxima at integer values of $\frac{q_x\, a}{2\pi}$, with height proportional to N_x^2 and width inversely proportional to N_x.

For sufficiently large N_x, Eq. 1.10 is comparable to an array of delta functions, this time in reciprocal space. For a three-dimensional bulk crystal, the derivations for the y and z directions are equivalent to the derivation for x above, and the diffracted intensity will be very small except at discrete points in reciprocal space. At these "bulk" or "Bragg" diffraction spots, the scattered intensity is very strong. Their positions are given by integer values of h, k, and ℓ, which can be used in place of the $\mathbf{q}$ vector to index reciprocal space:

$$\frac{q_x\, a}{2\pi} = h,$$

$$\begin{aligned} \frac{q_y\, b}{2\pi} &= k, \\ \frac{q_z\, c}{2\pi} &= \ell. \end{aligned} \tag{1.11}$$

The Laue condition states that h, k, and ℓ must simultaneously be integers for diffraction from a three-dimensional bulk crystal to occur.

In practice, N_x, N_y, and N_z are not usually well-defined, but are contingent on, for example, the x-ray coherence length and the grain size of the bulk crystal. If particle size is the limiting factor, then the width of the bulk peaks is inversely proportional to the average particle size; the actual shape of the peak depends on the particular distribution of particle sizes in the crystal. Measuring the integrated intensity, rather than the peak intensity, performs an ensemble average over effects such as particle size distribution, beam divergence, and the mosaic spread, and is therefore a useful crystallographic tool. To quantitatively extract structure factors from integrated intensity data, geometry-dependent (i. e., **q**-dependent) corrections for the Lorentz factor, polarization factor, and illuminated volume [1] must be performed.

1.1.3 Scattering from a crystal surface

In contrast to scattering from a bulk crystal, scattering from a surface does introduce an asymmetry in the sums of Eq. 1.7. One sum, usually the third, is abruptly truncated at the surface. The z direction is, then, taken to be perpendicular to the surface, with x and y in the surface plane. This may require a transformation from the traditional choice of lattice parameters. For example, in changing from reciprocal space coordinates (H, K, L) in standard face centered cubic orientation ($a = b = c; \quad \alpha = \beta = \gamma = 90°$) to (111) surface

[1] For surface diffraction, the correction is for variation of the illuminated surface area with **q**.

coordinates, the following transformation is used:

$$\begin{pmatrix} h \\ k \\ \ell \end{pmatrix}_{(111)} = \begin{pmatrix} -\frac{1}{2} & \frac{1}{2} & 0 \\ 0 & -\frac{1}{2} & \frac{1}{2} \\ 1 & 1 & 1 \end{pmatrix} \begin{pmatrix} H \\ K \\ L \end{pmatrix}_{\text{fcc}} . \tag{1.12}$$

The (real-space) z direction is, after this transformation, perpendicular to the surface; x and y are parallel to the surface and separated by 120°, reflecting the three-fold symmetry of the fcc(111) surface. Transformations from the standard fcc coordinates to (115), (104), and (113) surface orientations will be discussed in chapter 3. An important exception to this convention is α-Ga, whose (010) surface structure is described in chapter 2. Due to its orthorhombic symmetry, α-Ga's lattice parameters are not interchangeable. To maintain the crystallographic convention of Cmca symmetry (instead of nonstandard Bmab), the y axis must remain perpendicular to the surface.

Transformations such as Eq. 1.12 often yield indexing schemes which do not have Bragg peaks at every integer (h, k, ℓ) triplet. Instead, if the number of ways to "slice through" the surface unit cell in the x-y plane and form an equivalent surface is n_{layers}, then Bragg peaks will be separated in ℓ by an amount n_{layers}. (Some examples are listed in table 1.1.) For example, if a given crystal has a bulk peak at (h, k, ℓ_B), there will be bulk peaks at $(h, k, \ell_B \pm n_{layers})$, $(h, k, \ell_B \pm 2n_{layers})$, etc. In calculating surface roughness, described below in section 1.1.4, the absolute perpendicular momentum transfer does not matter, but the distance in q_z from the nearest Bragg point does; in this case $q_z\, c$ can be replaced by $\frac{2\pi}{n_{layers}}\,(\ell - \ell_B)$, where each (h, k) has a particular value of ℓ_B.

To calculate the amplitude of scattering from the surface of a semi-infinite crystal, the sum of Eq. 1.9 is given a definite ending point:

$$\begin{aligned} A &\propto \sum_{n=-\infty}^{N} F_{\text{bulk}} \exp\left(-in\,\mathbf{q}\cdot\mathbf{c}\right) \\ &= F_{\text{bulk}} \frac{\exp(-iN\,\mathbf{q}\cdot\mathbf{c})}{1-\exp\left(-i\mathbf{q}\cdot\mathbf{c}\right)}. \end{aligned} \tag{1.13}$$

Surface	n_{layers}
simple cubic (001)	1
fcc(001)	2
fcc(111)	3
fcc(115)	27
fcc(104)	17
fcc(113)	11
α-Ga(010)	2

Table 1.1: n_{layers} for several surfaces, including those considered in this thesis.

The intensity is, again, the square modulus of the amplitude. For integer values of h and k,

$$I \propto |A|^2 \propto |F_{\text{bulk}}|^2 \frac{1}{4 \sin^2\left(\frac{\mathbf{q}\cdot\mathbf{c}}{2}\right)}. \tag{1.14}$$

As with Eq. 1.9, Eq. 1.14 predicts high intensity at the bulk peaks. Away from the bulk peaks, however, diffracted intensity is concentrated in "rods" which originate at the bulk peaks and are oriented perpendicular to the surface, and therefore have been labeled "crystal truncation rods" (CTRs) [9] for h and/or $k \neq 0$. (The case of $h = k = 0$ is that of specular reflectivity, a surface-sensitive technique not limited to crystalline materials [10].) The constraint of finding intensity only at $\ell = \ell_B$ is relaxed. The inverse-sine-squared behavior produces a minimum in intensity at the anti-Bragg position (i. e., $\ell = \ell_B \pm n_{layers}/2$) where measurements are most sensitive to the conditions of the surface.

Real surfaces will not scatter according to Eq. 1.13 since two assumptions implicit in the derivation are not generally true, as discussed here and in section 1.1.4. First, the atoms at a crystal surface do not generally lie exactly at their bulk positions. This could be due to interlayer relaxations, absorption of foreign atoms, and/or reconstructions. A separate, surface structure factor must be calculated with Eq. 1.8 and added, with the appropriate phase, to Eq. 1.13:

$$
\begin{aligned}
A &\propto \sum_{n=-\infty}^{N} F_{\text{bulk}} \exp\left(-in\,\mathbf{q}\cdot\mathbf{c}\right) \;+\; F_{\text{surface}} \exp(-iN\,\mathbf{q}\cdot\mathbf{c}) \\
&= \left(\frac{F_{\text{bulk}}}{1-\exp\left(-i\mathbf{q}\cdot\mathbf{c}\right)} \;+\; F_{\text{surface}}\right) \exp(-iN\,\mathbf{q}\cdot\mathbf{c}). \qquad (1.15)
\end{aligned}
$$

The bulk and surface structure factors interfere, which aids in the determination of surface structure (since the bulk structure factor is usually known.)

When the surface is reconstructed, its unit cell has dimensions which are a multiple of the bulk unit cell's in-plane dimensions. Besides the CTRs, rods of scattering can appear at fractional values of h and/or k, as determined by the symmetry of the reconstruction. For these rods, there is no contribution from the bulk, i. e., $A \propto F_{\text{surface}}$. (An alternate calculation of the scattering from a reconstructed surface is performed by increasing the lateral dimensions of the bulk unit cell to match that of the surface. This way, h and k will be integers even for the rods due to the reconstruction and Eq. 1.15 applies, but F_{bulk} is identically zero.)

1.1.4 Scattering from a rough surface

Real surfaces are not perfectly smooth. Whether due to local rough spots or to long-ranged terraces, different regions of a crystal will truncate at varying heights; these surfaces at different heights will interfere with each other. The abrupt cut-off in the sums of eqs. 1.13 or 1.15 is no longer appropriate. In the derivation that follows, "roughness" always refers to crystalline roughness, i. e., all atoms on a given terrace remain at lattice sites. An amorphous or liquid overlayer will not affect CTR intensity in the same manner.

To calculate the scattering from the rough surface of a semi-infinite crystal, Robinson [9] assumed that the crystal was perfect up to $z = 0$, and above that, continually decreased in (laterally averaged) density (via a parameter β, which is less than unity). Eq. 1.13 then breaks into two sums:

$$A \propto F_{\text{bulk}} \left(\sum_{n=-\infty}^{0} \exp\left(-in\, \mathbf{q} \cdot \mathbf{c}\right) + \sum_{n=1}^{\infty} \beta^n \exp\left(-in\, \mathbf{q} \cdot \mathbf{c}\right) \right). \tag{1.16}$$

This method effectively sums from $z = -\infty$ to where the surface "might" be.

A more general method is to sum from $z = -\infty$ to the surface, and then sum over the probability of finding the surface at a given z. That is, let $P(N)$ be the probability of finding the surface at $z = N$. To find the scattered amplitude, two sums are performed:

$$A \propto F_{\text{bulk}} \sum_N P(N) \sum_{n=-\infty}^{N} \exp\left(-in\, \mathbf{q} \cdot \mathbf{c}\right). \tag{1.17}$$

The sum over n of Eq. 1.17 is exactly that of an ideal CTR, i. e., Eq. 1.13. The sum over N represents the surface roughness; the measured intensity is therefore the same as that for an ideally flat surface multiplied by a roughness factor

$$\left| \sum_N P(N) \exp\left(-iN\, \mathbf{q} \cdot \mathbf{c}\right) \right|^2. \tag{1.18}$$

The surface roughness, therefore, completely decouples from the crystalline structure of the surface; the expression for the intensity factors into separate components for structure and roughness.

Roughness has little effect near the Bragg peaks, where scattering is more sensitive to the bulk, but can significantly lower the intensity around the out-of-phase (anti-Bragg) position, where scattering is most surface sensitive. The extent of the effect, of course, is greater for greater values of σ, the root mean square surface width. Eq. 1.18 is solved for three probability distribution functions in Table 1.2. The probability distribution functions are shown in Fig. 1.1a, and the resulting roughness factors are shown in Fig. 1.1b.

Fig. 1.1c demonstrates the effect of these roughness models on CTR intensity. A geometric probability distribution gives the same results as Eq. 1.16, and in fact seems to work best for most surfaces. The roughness factor of the Poisson distribution [11] is qualitatively different than the geometric model, with a greater reduction in intensity at the anti-Bragg

Probability distribution	$P(N)$	Parameter(s)	σ	Roughness factor for CTRs
geometric	$(1-\beta)\,\beta^N$	β $0 \leq \beta < 1$	$\frac{\sqrt{\beta}}{1-\beta}$	$\frac{(1-\beta)^2}{1+\beta^2-2\beta\cos(q_z c)}$
Poisson	$\frac{e^{-\lambda}\,\lambda^N}{N!}$	λ $\lambda \geq 0$	$\sqrt{\lambda}$	$\exp\left(-4\lambda\sin^2\left(\frac{q_z c}{2}\right)\right)$
binomial	$\frac{n!(n-N)!}{N!}\,p^N\,(1-p)^{n-N}$	n, p $n = \text{integer} > 0$ $0 \leq p \leq 1$	$\sqrt{np\,(1-p)}$	$\left[1-2p\,(1-p)\,(1-\cos\,(q_z c))\right]^n$

Table 1.2: Forms for various roughness models. The product of the roughness factor and the intensity of a smooth surface's CTR is the intensity of the rough surface's CTR. For amplitudes, take the square root of the roughness factor.

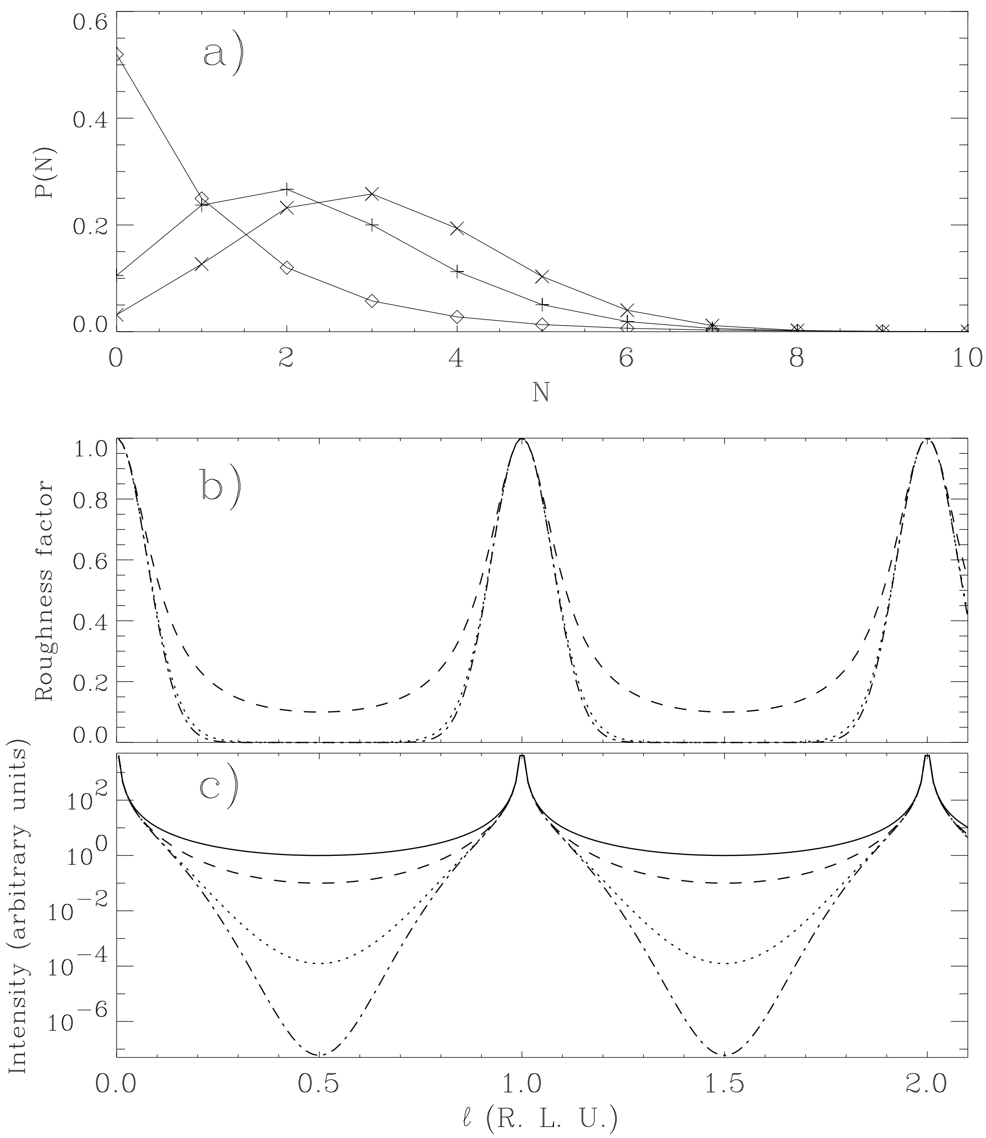

Figure 1.1: a) Probability distribution functions for the geometric, Poisson, and binomial distributions (symbols: $\diamond$, $+$, $\times$ respectively). For each distribution, $\sigma = 1.5$ unit cells, corresponding to $\beta = 0.52$, $\lambda = 2.25$, and $p = 0.25$ with $n = 12$. In all three cases for this value of σ, $P(N > 8) < 10^{-3}$; the binomial distribution is identically zero for $N > 12$.
b) Roughness factors calculated for the distributions of a), using Eq. 1.18. The dashed, dotted, and dash-dot lines represent the roughness factors modeled by geometric, Poisson, and binomial distributions respectively.
c) Effect of roughness on CTR intensity. The roughness factors of part b) are multiplied by the intensity from a bulk-truncated CTR, Eq. 1.14. For comparison, the solid line represents the intensity from a smooth surface.

position and less reduction nearer to the bulk peak. The binomial distribution requires two parameters, a real p and an integer n (which must be varied discretely when fitting a roughness model to data). Unlike the geometric and Poisson distributions which (mathematically if not physically) extend to $z = +\infty$, the binomial distribution ends at $z = n$. For a given σ, its roughness factor is like the Poisson, but with less intensity at the anti-Bragg position; for large n and small p, the binomial distribution approaches the Poisson, with $\lambda = np\,(1-p)$.

The enormous difference in the roughness models for large σ is clearly seen in Fig. 1.1c. The geometric model has the least intensity loss of the three models, even though σ, the root mean square width of the distributions, is the same. However, the maximum of $P_{geometric}\,(N)$ $[= 1-\beta]$ is always at $N = 0$, meaning most terraces of the crystal are at height $z = 0$. The probability distribution functions in the Poisson and binomial cases are less sharply peaked, resulting in most terraces being spread among three or four values of z. The greater spread in these distributions' *peaks* results in less intensity, for a given width of the overall distribution. In the opposite limit of small σ, the models become equivalent; the roughness factor becomes $1 - 4\sigma^2 \sin^2\left(\frac{q_z c}{2}\right)$.

Besides the three examples discussed above, any discrete probability distribution can model roughness with Eq. 1.17. This includes discrete versions of continuous distribution functions, such as the Gaussian distribution [11]. However, the roughness factor has no simple analytical form since the discretized Gaussian distribution must be numerically normalized; this quickly becomes computationally expensive if σ is a fitting parameter.

In the case of a reconstructed surface, the fractional order rods cannot have the same roughness factor as integer order rods since the fractional order rods do not pass through bulk peaks. This roughness factor can be calculated in the limit of coherent scattering from terraces at the same height, and incoherent scattering between reconstructed terraces at different heights. This model probably applies best to surfaces with long, flat terraces with evenly distributed steps, rather than a heavily stepped surface. The scattered amplitude from a terrace at given height is proportional to the number of scatterers on the terrace, i. e., its size. This, the area of a terrace at height N, is proportional to $P(N)$, the probability that the crystal truncates at $z = N$. The intensity scattered from this terrace is simply $P^2(N)$, and the incoherently scattered intensity from such a surface is proportional to the sum of the probabilities squared, without any phase factor:

$$\sum_{n=0}^{\infty} P^2(N) \tag{1.19}$$

All intensities from fractional order rods are thus decreased by a q-independent, constant factor. For the geometrical model of roughness, the factor for fractional order rods is

$$\sum_{n=0}^{\infty} P^2(N) = \sum_{n=0}^{\infty} (1-\beta)^2 \beta^{2n} = \frac{1-\beta}{1+\beta}\,. \tag{1.20}$$

The factor for the Poisson model is

$$\sum_{n=0}^{\infty} P^2(N) = \sum_{n=0}^{\infty} \frac{e^{-2\lambda}\lambda^{2n}}{(n!)^2} = e^{-2\lambda} I_0(2\lambda)\,, \tag{1.21}$$

where I_0 is the zeroth-order modified Bessel function.

1.1.5 Thermal vibrations

Atomic vibrations may significantly affect intensities measured by surface diffraction. To zeroth order, the only effect is a (q-dependent) decrease in the scattered intensity, without changing any peak widths or positions [1]. For small enough vibrations, atomic positions can be represented with a Gaussian distribution, corresponding to atoms in a harmonic potential. In this model (which is exact if the atomic potentials are purely harmonic), the atomic form factor (Eq. 1.4) is simply multiplied by the Debye-Waller factor

$$e^{-M} = e^{-B\,q^2/\left(16\,\pi^2\right)} = e^{-<u^2>q^2/2}\,, \tag{1.22}$$

where $< u^2 >$ is the mean square displacement of the atom from its average location. Different elements (or atoms of the same element at different sites) will in general have different values of B.

In general, thermal vibrations need not be isotropic, but only vibrations in the direction of $\mathbf{q}$ have an effect on the intensity. That is, with Cartesian coordinates Eq. 1.22 can be replaced by

$$e^{-\left(B_x\, q_x^2\, + B_y\, q_y^2\, + B_z\, q_z^2\right)/(16\,\pi^2)} \tag{1.23}$$

with $B_m\,/8\pi^2\; = < u_m^2 >$, the mean square displacement in direction m. This anisotropy is particularly relevant to surface diffraction, since atomic vibrations at surfaces tend to be higher than the bulk, but are particularly enhanced perpendicular to the surface due to the loss of coordination.

The higher order effects of thermal vibrations [1] do not matter much in surface diffraction except as a nuisance, since they result in a relatively isotropic, slowly varying background which can be subtracted from integrated intensity measurements. (Subtracting this thermal diffuse background could be more difficult very close to the bulk Bragg peaks, where it is strongest.) On the other hand, anharmonic vibrations may be particularly important at some surfaces. For K/Ag(001)–(2×1), Meyerheim *et al.* [12] demonstrated that neglecting anharmonicity results in a severe overestimation of the first Ag layer's contraction relative to the second. A harmonic potential would require a surface atom to vibrate inward and outward with equal probability; in reality, at least for the top-layer Ag atoms in this system, the anharmonic potential causes excursions away from the surface to be much larger than excursions into the bulk.

1.2 Experimental set-up

1.2.1 Diffraction chamber

Most surface science experiments must be performed in a vacuum chamber for two reasons. One is a limitation of the technique: the mean free paths of electrons, ions, and atoms (the most common surface probes) are too small in air to be useful. (A notable exception is experiments in a tunneling configuration; STM is usable in atmosphere due to the tiny separation of the tip from the surface.) Light does not suffer this limitation, allowing x rays, with their large absorption lengths, to be a useful probe of surfaces in electrochemistry environments (e. g., [13, 6]) as well as buried interfaces (e. g., [14]).

The other, more fundamental, reason is the nature of surfaces. Many surfaces can be altered or completely changed as a result of exposure to various gases; the oxygen-induced faceting of Cu(115) described in chapters 3 and 4 is a prime example. In order to study the fundamental nature of a surface, as desired in chapter 2, exposure to foreign gases must be kept to a minimum.

All of the experiments described in this thesis were performed on the surface diffraction chamber [15] installed on beamline X16A of the National Synchrotron Light Source, Brookhaven National Laboratory. The UHV chamber, pictured in Fig. 1.2, is connected to a diffractometer which, through a series of differentially pumped bellows, holds the sample in place. The bellows allow the “five-circle” diffractometer to make high-resolution changes to the sample’s angular position without needing to move the bulky chamber. The sample holder is connected to the sample manipulator with three springs. When the sample is positioned for diffraction, the sample holder rests on a kinematic mount directly attached to the diffractometer. The manipulator is pulled back from the sample holder, so the three springs are in tension; motions of the sample are thus decoupled from motions of the chamber. A laser beam is reflected at nearly normal incidence (through a viewport at the end of the chamber) to find the optical surface of the sample.

The diffractometer motions are 2θ, θ, ϕ, and χ, typical of a four-circle diffractometer, [16] as well as α, a rotation of the sample and detector (and the entire chamber) about a vertical axis. This fifth angle is useful because the bellows severely restrict the range of χ. The α angle (along with the very wide Be window) allows out-of-plane measurements, i. e., measurements at nonzero ℓ. The diffractometer and detector are computer controlled

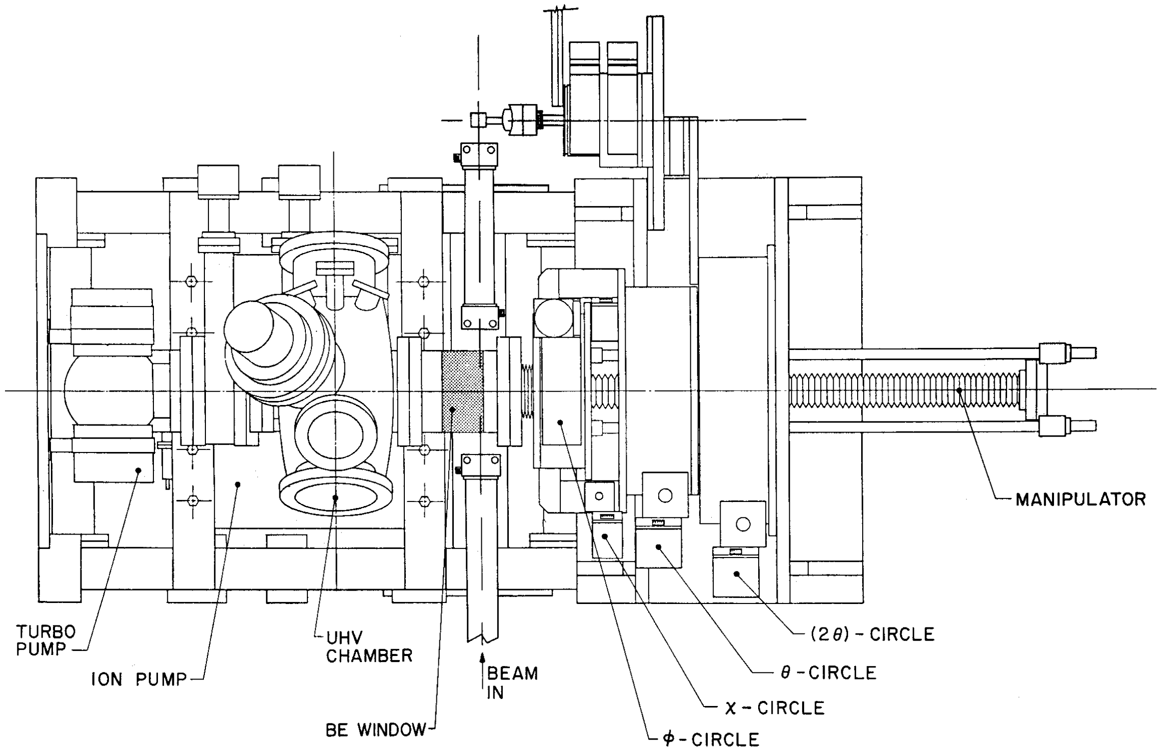

Figure 1.2: Top view of Bell Labs/Illinois surface diffraction chamber installed on beamline X16A of the NSLS. (The beam actually comes in from the top of the figure, and the detector is toward the bottom center.)

[17], with the computer performing the conversions from reciprocal space to angular space [16, 18, 19].

The detector for most of the experiments in this thesis was a one-dimensional position-sensitive detector. Slits defined the angular resolution of the detector. The detector was aligned to be (nearly) parallel to $q_\perp$, thus integrating along the crystal truncation rod. This allowed higher resolution for the in-plane directions, acceptable since intensities along the rods vary slowly. Note that the magnitude of the momentum transfer, $|q|$, is determined by the detector position, which moves on both the 2θ and α circles.

Two constraints are needed to map three-dimensional reciprocal space onto the five angles of the diffractometer, and are chosen to be convenient to surface diffraction. The first constraint requires the sample normal to be (approximately) horizontal; given the horizontal polarization of the synchrotron radiation, this minimizes intensity loss due to the polarization factor. Also, the divergence of synchrotron radiation from bending magnets is generally greater in the horizontal direction; a horizontal sample normal allows for maximum resolution in the surface plane. The second constraint permits a choice of the incident angle or exit angle (or the choice that they be equal). In this work, the exit angle is usually chosen to be well above the critical angle, to avoid complications of refraction [20], yet as small as practical to limit detection of scattering from the bulk, which in turn minimizes background noise from fluorescence, Compton scattering, and thermal diffuse scattering. The exit, rather than incident, angle is kept small to better keep the 1D position-sensitive detector parallel to $q_\perp$ [21].

Besides x-ray diffraction, the chamber has standard surface science tools, including low energy electron diffraction (LEED), Auger electron spectroscopy, an ion sputtering gun, sources to evaporate thin films of various materials, leak valves to admit gases such as oxygen or argon, and pressure gauges (an ion gauge and a residual gas analyzer). To reach the surface analysis tools, the sample must be moved from the x-ray diffraction position. The sample sits on the end of the sample manipulator, a long rod which can move the sample to the opposite end of the chamber. The manipulator can be turned by 90° at a knuckle joint to face the sample toward the LEED, Auger, or sputtering devices. Inside this rod are two copper wires to carry electrical current, two pairs of Chromel/Alumel wires for thermocouples, and a coaxial tube through which liquid nitrogen can flow for cooling.

1.2.2 Design and use of load lock

One fundamental challenge to surface science is the cleanliness of the sample environment. UHV conditions are not easy to achieve, needing good pumping systems and some standard techniques. The chamber at X16A is pumped by a large turbomolecular pump, an ion pump, and a titanium sublimation pump (TSP). A smaller turbo pump is dedicated to the differentially pumped seals at the bellows. The turbo pumps are backed by roughing pumps which must begin the pumping from atmospheric pressure; the ion pump and TSP are more useful in maintaining, rather than achieving, UHV conditions. The process of "baking out" a chamber after opening it to air is typically required to produce a clean environment. For the apparatus at beamline X16A, a bakeout entails building an oven around the chamber, heating it overnight, then slowly letting it cool; often the diffractometer must be realigned afterwards. This ~24-hour process is needed to achieve base pressures of $\lesssim 3 \times 10^{-10}$ Torr. However, it can become time consuming when similar experiments are repeated in succession (e. g., deposition of metals on Si [22]; Si wafers are not generally reusable), and is not possible for samples with low melting points (e. g., Ga, as described in chapter 2).

To overcome this limitation, we have designed and installed a load lock on the chamber to permit access to the sample without breaking vacuum in the main chamber. A 6" gate valve (VAT) was installed on the chamber, directly in line with the sample manipulator. This valve typically remains closed, but is opened when the sample is moved into the load lock (and to align the sample's optical surface using a reflected laser beam). Attached to this valve is a specially designed reducing flange (MDC Corp.) which receives the sample holder. The sample holder seals against a Viton o-ring which is held in a groove of the reducing flange. A cross-shaped transfer chamber (MDC Corp.) is attached to the reducing flange; the sample enters this transfer chamber as the seal is made against the o-ring. Opposite the sample is a window, so the sample can be carefully observed as it is moved into place; on one of the side flanges is a small turbo pump which pumps on the transfer chamber. Once the sample is in place, the pump can be turned off and the transfer chamber removed, allowing access to the sample.

The sample holder was carefully designed to allow maximal utility in the limited space available. In the center is a thermal feedthrough, a copper rod brazed to copper braid, which attaches to a liquid nitrogen cold finger. The copper rod is brazed to a thinwall stainless steel tube for thermal insulation. Surrounding the thermal feedthrough are six electrical feedthroughs (Ceramaseal, Inc.); these are brazed at an angle to reduce the bending of the conductors. Two of these feedthroughs have copper conductors for sample heating via a filament (e. g., Cu samples), electron bombardment (e. g., Pt), or a current through the sample (e. g., Si). The others are two pairs of Chromel and Alumel, for thermocouples. The tapped holes are for rods from the sample mount, which firmly hold the sample at the appropriate height. The flat face at the largest diameter seals against the o-ring. Fig. 1.3 is a cross-section of the assembly, with the sample holder approaching the sealed position. One person (but preferably two people) can use this load lock to change samples in about three hours. If the flat face of the sample holder seals correctly against the o-ring, pressure should not rise in the main chamber when the transfer chamber is vented to air. However, once the sample transfer is complete, the sample and the parts of the load lock exposed to air usually need degassing.

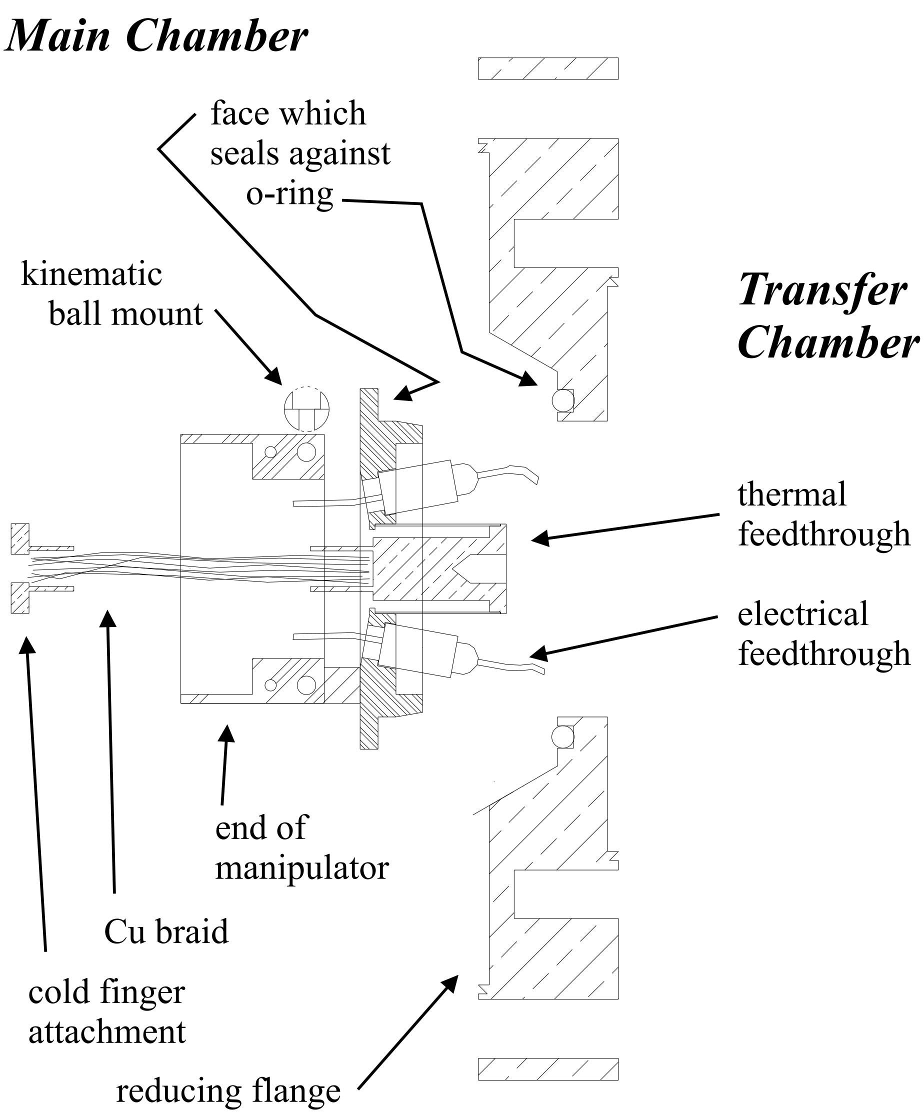

Figure 1.3: Sectional view of load lock installed on X16A surface chamber. The main UHV chamber is to the left, and the transfer chamber (not shown) on the right. Parts are described in the text.

Chapter 2

Surface structure of α-Ga(010)

2.1 Introduction

Atoms at surfaces face lower coordination than their bulk counterparts, often accommodating this change in environment by displacing from locations given by a simple truncation of the bulk. For clean metal surfaces, the loss of coordination results in a tendency for the outermost plane of atoms to relax inwards, allowing those atoms to become more fully bathed in the electronic sea. For semiconductor surfaces, it may result in dangling covalent bonds, a high-energy situation often resolved by reconstructions which minimize the number of dangling bonds across the surface's unit cell, usually with a periodicity which is some multiple of bulk unit cells. The stable phase of gallium at low pressure, labeled α-Ga, is commonly thought to contain both metallic and covalent bonds. Investigations of α-Ga surfaces lend insight to the unusual metallic-covalent duality of this material, and hence to metal-insulator transitions in general. Here we report an experimental determination of the three-dimensional structure of α-Ga(010) surface.

Several recent x-ray reflectivity studies have probed the surface structure of (fully metallic) liquid Ga, finding layering of the liquid at the free surface and in contact with a hard wall. For the liquid Ga/vacuum interface, Regan *et al.* [23, 24] measured a layering with spacing $d \sim 2.6$ Å (consistent with atomic layering), with an exponential decay length of about 6 Å. These lengths remained remarkably constant over the temperature range $T = 295$ K (supercooled liquid) to 443 K; only the amplitude of the layering decreased with temperature. Quantum Monte Carlo simulations by Zhao *et al.* [25] support these results. (Inelastic scattering of supersonic Ar and Xe atoms from the liquid Ga surface has also been found to be independent of temperature; the gas-liquid energy transfer remains constant from 40 to 400° C [26].) At the liquid Ga/diamond(111) interface, Huisman *et al.* [27] found a layer spacing of $d \sim 3.8$ Å (approximately the bilayer spacing of $\frac{b}{2}$ for α-Ga, possibly indicative of covalent bonding in the liquid) and a decay length of 4 Å. Neither experiment found any evidence of in-plane ordering of the liquid Ga.

2.1.1 Bulk α-Ga structure

α-Ga is a semi-metal with a low melting point ($T_m = 303$ K). Its orthorhombic crystal structure has Cmca symmetry with $a = 4.5192$ Å, $b = 7.6586$ Å, and $c = 4.5258$ Å [28]. In labeling the orthorhombic axes, we follow the crystallographic convention (Cmca symmetry). Refs. [29, 30, 31, 32, 33, 34] follow the historic (pseudotetragonal) convention, reversing the b and $\bar{c}$ axes and yielding a structure with nonstandard Bmab symmetry. With eight atoms per unit cell, α-Ga is not very dense and its density increases upon melting. One atom is located at $(0, y, z)$, where $y = 0.1539$ and $z = 0.0798$ in fractional coordinates of the unit cell [28]. The seven other atomic positions are determined by the $(8f)$ site symmetry:

$$\pm(0, y, z);\ \ \pm(\frac{1}{2}, y, \frac{1}{2} - z);\ \ \pm(0, \frac{1}{2} - y, \frac{1}{2} + z);\ \ \pm(\frac{1}{2}, \frac{1}{2} + y, z).$$

That is, two atoms are placed at each y, with $x = 0$ or $\frac{1}{2}$. As seen in Fig. 2.1, each atom has a total of seven neighbors in the first coordination shell. One of these neighbors is at the surprisingly short distance of 2.465 Å. The pairs of atoms connected by this 'dimer' bond

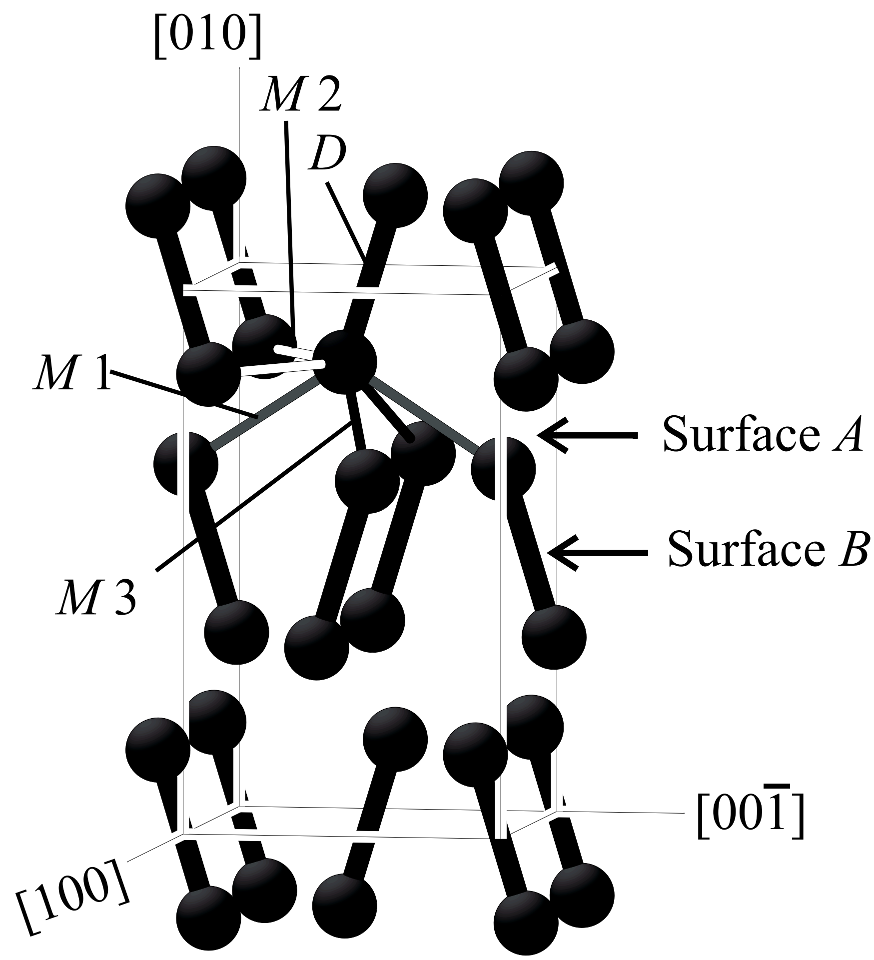

Figure 2.1: Bulk structure of α-Ga, showing the seven nearest-neighbor bonds for one of the atoms. The covalent bond labeled D has a length of 2.46 Å; the three pairs of metallic bonds are $M1$, $M2$, and $M3$, and are 2.70 Å, 2.73 Å, and 2.79 Å long respectively [28]. Bulk truncations to form the two possible (010) surfaces, A and B, are indicated.

(labeled D in Fig. 2.1) are angled $\pm 17.0°$ from [010], and are generally thought to be bonded covalently, as discussed below. The six next nearest atoms are paired at distances of 2.70 Å, 2.73 Å, and 2.79 Å; the bonds to these atoms are labeled $M1$, $M2$, and $M3$ respectively.

The one short dimer bond is the most prominent feature of the α-Ga structure, implying that the Ga_2 dimer is the fundamental building block of the crystal. Speculation on the covalent nature of the dimer bond has existed since the first accurate α-Ga structure determination [35], but direct evidence has been limited. The electrical conductivity is lowest along the b axis (i. e., the average direction of the dimer bonds) and much greater in the (010) plane [36]; thus, the bonds in the (010) plane (labeled $M1$, $M2$, and $M3$ in Fig. 2.1) are more metallic than the dimer bonds. Breaking of covalent bonds upon melting may explain the high entropy of melting of α-Ga (almost twice that of metallic β-Ga) [37]. Early calculations by Heine [38] concluded that the short bond length and low-symmetry structure is merely the result of a minimum in the pseudopotential which favors a short bond length despite the large unit cell. However, *ab initio*, total energy calculations of α-Ga bulk structure [29, 33] found significant charge accumulation in the dimer bonds. Furthermore, electronic band structure calculations [29, 33] predicted a pseudogap in the electronic density of states at the Fermi level, consistent with the semimetallic nature of α-Ga; highly anisotropic band structure at the Fermi surface, consistent with the anisotropic conductivity [36]; and a bonding-antibonding transition at ~ 2.3 eV associated with the covalent bonds, consistent with optical conductivity measurements [39, 40].

For a fresh perspective on the α-Ga bulk geometry, Häussermann *et al.* [41] did not assume the Ga_2 dimer is the building block of α-Ga. Instead, they modeled a two-dimensional net of Ga atoms with the symmetry of a terminally-coordinated deltahedral cluster. Within a net, the atoms are connected with multicenter (i. e., metallic) bonds, but each atom has one dangling bond left over. To construct a 3-d structure, 2-d nets are connected at the dangling bonds, forming two-electron, two-center (i. e., covalent) bonds between the nets. Buckling these nets to an appropriate angle while maintaining Cmca symmetry produces the (slightly idealized) α-Ga structure. Maintaining Immm symmetry during the buckling and adding a glide plane produces the β-Ga structure. Thus, this model succinctly explains the short length of the covalent bond, the metallic bilayers, and the overall low symmetry of the bulk structure.

2.1.2 Previous work on α-Ga(010)

To further understand the properties of this unusual material, we turn to the (010) surface. Due to the low symmetry of bulk α-Ga, two possible (010) surfaces can be created from ideal bulk terminations. As shown in Fig. 2.1, splitting the metallic bilayer creates surface A, while a cut through the dimer bonds creates surface B. Surface A is created by the breaking of four metallic bonds per surface atom, and B by the breaking of one covalent bond. These two surfaces are separated by one-quarter of a unit cell, and would presumably have very dissimilar properties. According to *ab initio*, total-energy calculations by Bernasconi *et al.*, [31] neither A nor B's ideal surface is stable, but the lowest-energy surface is a major rearrangement of surface A: the top layer of dimers is tilted and stretched, significantly decreasing the degree of covalency. The top two atomic layers become metallic, and are comparable to two layers of Ga III (a fully metallic, high-pressure phase of Ga [42]) which self-wet the α-Ga. Although Ga III is face-centered tetragonal, Bernasconi *et al.* argue that two layers of Ga III can deform to match the proposed structure, if the in-plane lattice parameters are appropriately constrained.

Züger and Dürig [30] performed scanning tunneling microscopy (STM) experiments of α-Ga(010), finding the atoms of the top layer relax significantly in both the x and z directions. (We have relabeled the axes from their paper [30] to be consistent with the crystallographic convention [28].) The degeneracy of the two surface atoms per unit cell is broken, with one shifted 0.05 Å higher than the other, and thus separated by 2.723 Å (slightly less than the bulk $M2$ bond length). STM is inherently limited as a crystallographic tool; its inability to probe below the top layer of atoms does not allow it to differentiate between surfaces A and B. STM is, however, ideal for examining surface "defects." For example, Züger and Dürig determined that the (010) surface is extremely stable even up to the melting point, without the appearance of any vacancies, adatom diffusion, or step fluctuations. More significantly, a step-height analysis of a slightly miscut (010) surface shows all steps are 3.8 Å high. This distance is one half the unit cell; no steps of 1.9 Å, or $\frac{b}{4}$, were found, clearly demonstrating that α-Ga(010) terminates as surface A *or* B, but not a mixture of both.

2.2 Experiment and results

2.2.1 Experimental set-up

In order to conclusively differentiate between surfaces A and B, we used surface x-ray diffraction to determine the surface structure. The α-Ga single crystal used in this experiment was grown in UHV conditions, with the (010) surface an as-grown natural facet. Surface x-ray diffraction measurements were performed at beamline X16A of the National Synchrotron Light Source, Brookhaven National Laboratory. A load-lock installed on the surface diffraction chamber [15] allowed introduction of the sample without breaking vacuum (base pressure of chamber $\sim 7 \times 10^{-10}$ Torr for this experiment). The surface was cleaned with repeated cycles of 1 keV Ar ion bombardment, but no annealing, due to the low melting temperature. 882 structure factors were measured at $T \sim 290 \pm 10$ K, using 9.7 keV x rays. The structure factors, derived from integrated intensities of diffractometer ϕ-scans, were corrected for Lorentz and polarization factors and the variation of the illuminated area on the surface. These structure factors were symmetry averaged (with an average agreement factor of 9.5%) to 278 points on ten crystal truncation rods [9]. The structure factor data are shown in Fig. 2.2, along with the A and B bulk terminations and the best fit (described below). With no superstructure reconstruction on this surface, all these rods pass through bulk diffraction peaks.

2.2.2 Results

In our model of the surface, the atoms are allowed to relax from their bulk-defined positions, including the x direction (breaking the bulk's mirror-plane symmetry in which all

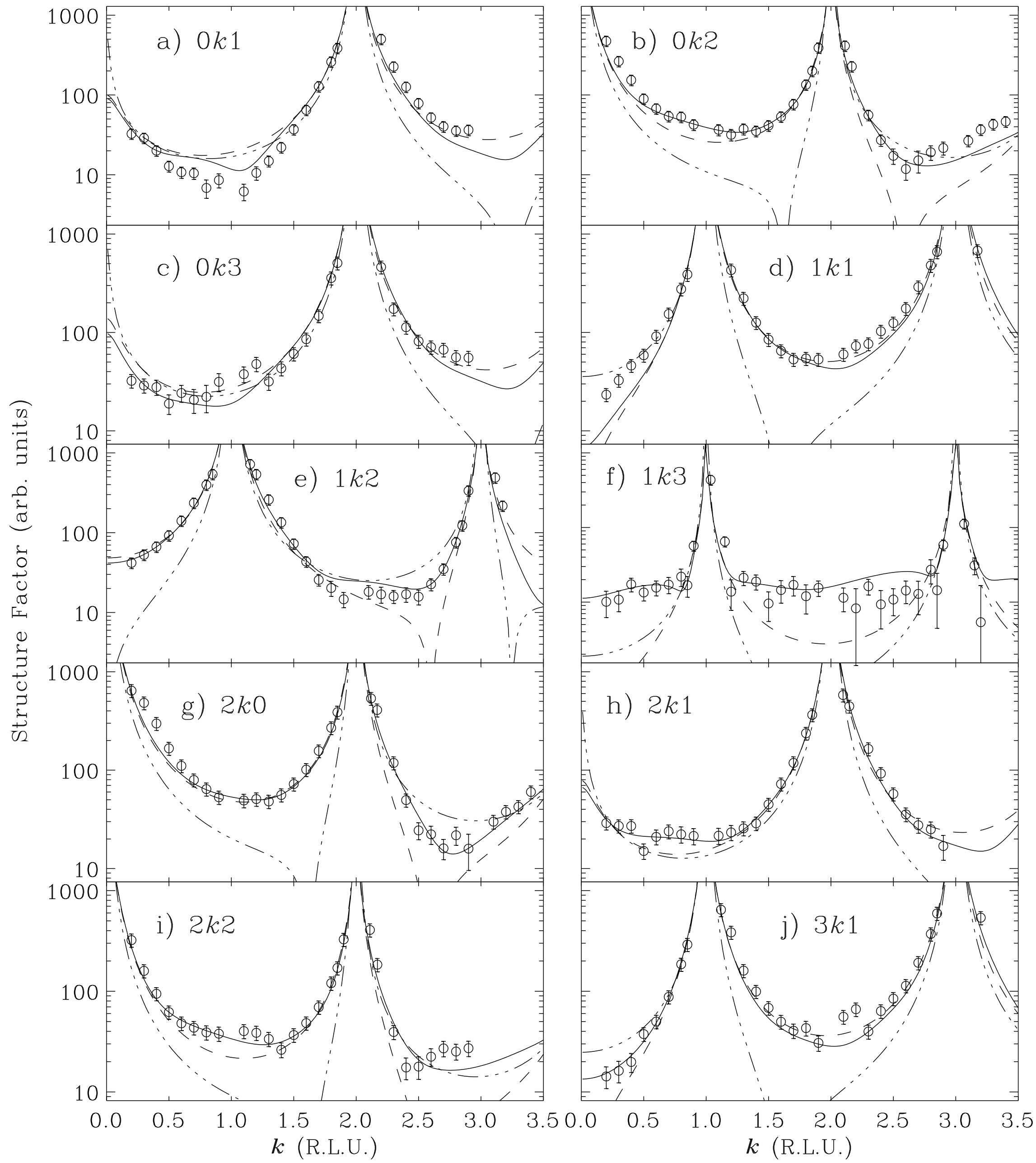

Figure 2.2: Structure factors of the ten crystal truncation rods measured. Circles represent data points, solid lines represent the best fit based on a relaxation of surface B. Dashed and dash-dot lines indicate values for bulk truncations of surfaces B and A, respectively ($\chi^2_B = 5.5$; $\chi^2_A = 13.2$). To maintain the crystallographic convention of labeling the α-Ga axes, we break with surface science convention and use k as the continuous variable to index the rods.

atoms are at $x = 0$ or $\frac{1}{2}$). However, the two atoms per unit cell at a given y value remain crystallographically equivalent. Thus, when one atom is displaced by $(+\Delta x, +\Delta y, +\Delta z)$, its partner will move in $(-\Delta x, +\Delta y, -\Delta z)$. Given this degeneracy, our fitting procedure averages intensities over equally probable surface domains with opposite displacements in x and/or z.

Models based on surface A could only give a good fit when the top layer atoms are substantially expanded away from their neighbors and attain unphysically large Debye-Waller factors, suggesting the *absence* of this layer. In fact, the best fit of the surface is a relaxed version of surface B, with shortened nearest-neighbor metallic bonds and lengthened dimer bonds. In this model, the atoms of the top five layers of the surface were allowed to relax in y and z, and the top three layers could also relax in x. Neither further relaxations nor the breaking of any layer's degeneracy improved our fit.

In addition to thirteen displacive parameters, our model includes an overall scale factor, a roughness factor, and three Debye-Waller parameters. Using a standard formulation for roughness based on a geometric distribution of terrace heights [9], we find a width of $\sqrt{\sigma^2} = 12.7 \pm 1.$ Å ($\beta = 0.74$, as defined in ref. [9]) and section 1.1.4. The other height distribution functions modeling roughness, described in section 1.1.4, did not yield satisfactory fits. This large value does not necessarily indicate that α-Ga(010) is an intrinsically rough surface; rather, it is the result of the surface's apparent inability to anneal below its (low) melting point. The constant value of the crystal truncation rods' widths along k indicate that this roughness is not laterally correlated.

Three Debye-Waller parameters were used to model thermal vibrations. All atoms except the two of the top layer could be assigned to one isotropic Debye-Waller parameter, which was fixed at $B_{bulk} = 0.4$ Å^2. The two atoms on the top layer needed an anisotropic Debye-Waller factor, separating perpendicular and in-plane vibrations. As expected, the vibrations perpendicular to the surface were significantly enhanced: $B_\perp = 9.6 \pm 1.2$ Å^2 vs. $B_\parallel =$

1.43 ± 0.2 Å^2. These high values are probably a result of being only 10–20 K below the melting point, although $B_\perp$ and the surface roughness are correlated, since both act as $q_\perp$-dependent scale factors. Assigning independent Debye-Waller factors to additional atoms neither improved the fit nor altered the refined atomic positions.

Table 2.1 lists the in-plane displacements from bulk and vertical layer changes of our refined model, yielding a $\chi^2 = 2.43$. Fig. 2.3 graphically displays the relaxed positions of the atoms compared with the bulk coordinates. The magnitudes of the in-plane displacements Δx and Δz are generally smaller than the changes in interlayer separation (δd), and decrease with depth. The breaking of mirror-plane symmetry is needed to achieve a fit of this quality, and is qualitatively consistent with the STM and LEED results of Züger and Dürig [30], but not the LEED work of Hofmann *et al.* [43] To visualize the effect of the model's atomic displacements on nearest-neighbor interatomic distances, Fig. 2.4 plots bond length vs. depth from the surface for the dimer bond (D) and the three metallic bonds ($M1$, $M2$, and $M3$). The trend is a decrease in metallic bond lengths and a slight increase in dimer bond lengths. The differences in bond lengths from bulk values are generally greatest at the surface, decreasing towards the bulk. The $M2$ bond, of which there are two per bilayer, tends to zigzag.

If one assumes that bond *length* is a measure of bond *strength*, then the α-Ga(010) surface is clearly more metallic than the bulk. This enhanced metallicity comes at the expense of the covalent dimer bonds, which are somewhat weakened (lengthened) relative to bulk dimers. This finding is in complete accord with photoemission experiments by Hofmann *et al.* [43], which found a metallic surface state in the $\overline{C}$–$\overline{X}$ direction of the surface Brillouin zone, for temperatures above 210 K. Bernasconi *et al.* [31, 32, 34] predicted α-Ga(010) would be stable as a fully metallic surface, but their proposed surface had a completely different structure.

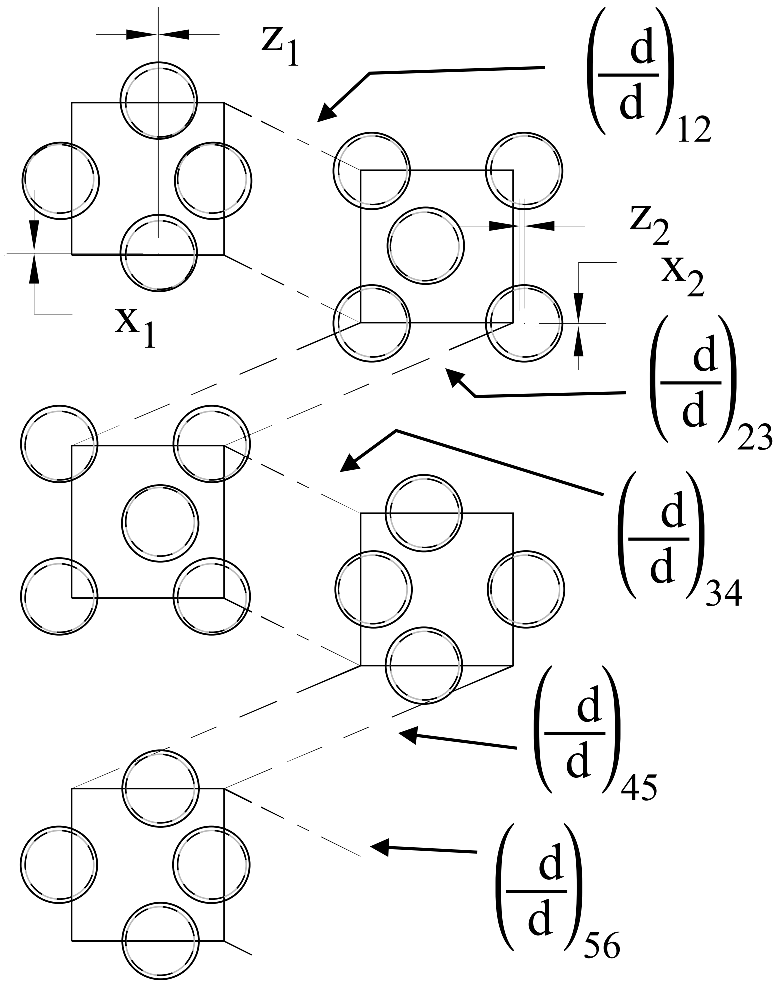

Figure 2.3: Layer-by-layer dissection of our model for the α-Ga(010) surface structure. Smaller, broken circles represent bulk atomic positions, while the larger circles represent relaxed positions. Atomic and interlayer displacements are labeled.

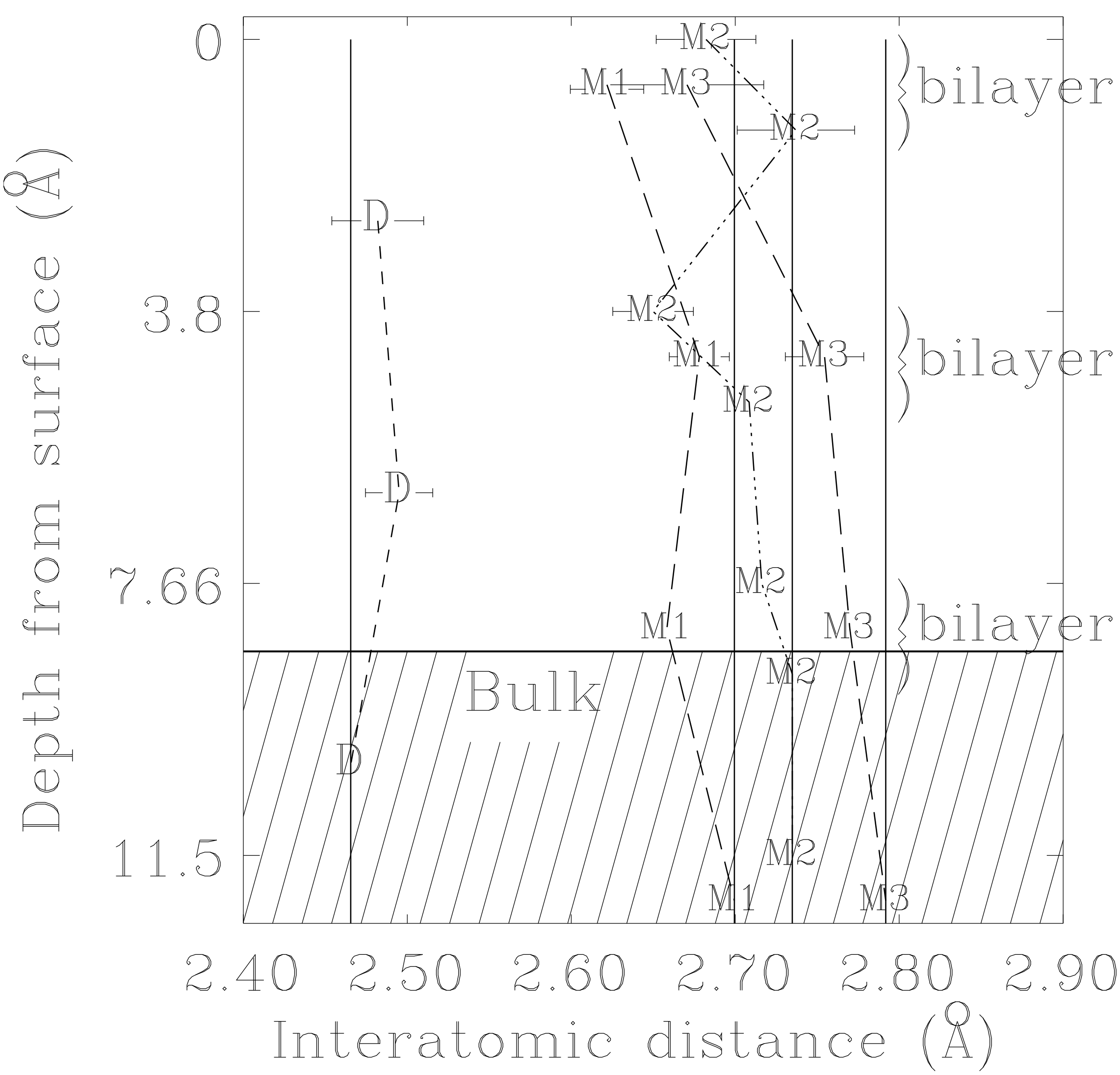

Figure 2.4: Nearest-neighbor atom separations classified by bond type (as defined in Fig. 2.1) versus depth from surface. Error bars are displayed when larger than symbols. Solid vertical lines represent bulk bond lengths; note that all bond lengths in the shaded region were fixed at bulk values.

i	Δx_i (Å)	Δz_i (Å)	$(\frac{\delta d}{d})_{i,i+1}$ (%)
1	0.0125(36)	0.0084(8)	−9.6
2	−0.0054(44)	0.0071(7)	10.2
3	0.0107(27)	0.0014(8)	−0.9
4	0	0.0052(7)	0.8
5	0	−0.0037(7)	−3.4

Table 2.1: In-plane and interlayer displacements from bulk for one domain of our model of α-Ga(010), a relaxation of surface B, with $\chi^2 = 2.43$. Errors, based on a least-squares fit, are in parentheses.
$d = 1.472$ Å for odd i (within one metallic bilayer), and $d = 2.357$ Å for even i (between metallic bilayers). Δx_4 and Δx_5 are fixed.

2.2.3 Discussion

We find using surface x-ray diffraction that the structure of α-Ga(010) is a relaxation of surface B, the surface created by cutting through dimer bonds. To our knowledge, this is the lowest-symmetry surface structure determined with x-ray diffraction to date. At the surface, metallic bonds are contracted and covalent dimers are expanded. This result is difficult to reconcile with the traditional view of Ga_2 dimers being the building blocks of the bulk α-Ga structure, which should lead to an A-terminated surface. It is only reasonable if the fundamental building blocks are the corrugated metallic bilayers as suggested by Häussermann *et al.* [41] However, this surface still leaves one unsaturated dangling bond per surface atom. These dangling bonds might be satisfied in another α-Ga surface structure, the $c(2 \times 2)$ reconstruction observed with LEED below 210 K by Hofmann *et al.* [43]; this speculation invites a full structural study for this low-temperature phase. We hope further calculations will be performed to confirm the stability and determine the band structure of the high-temperature B surface of α-Ga(010). Even the bulk structure of α-Ga is difficult to calculate, since several metastable and high-pressure phases of Ga lie close in energy to the stable α phase. Accurately calculating Ga surface structures would therefore be a stringent test of theoretical methods.

Chapter 3

Structure of Cu(115): Clean surface and O-induced facets

3.1 Introduction

The structure of many crystalline surfaces are affected by the adsorption of foreign species [44], sometimes undergoing minor rearrangements to accommodate the adsorbed atoms or molecules, in other situations undergoing major transformations. Some adsorbed species induce highly organized reconstructions, while others form incommensurate overlayers. Others yet can destroy the reconstructions formed on clean surfaces, such as the well-known case of H on Si(001)(2×1) [45]. In other cases, surface adsorbates lead not to additional order, but to disorder such as surface alloying (exhibited in certain metal-on-metal systems) [46], surface roughening, or even amorphization. Under the appropriate circumstances, faceting, the breaking up of a flat surface into large-scale terraces with particular crystallographic orientations, can occur. Whether the driving force is primarily short-range chemical forces, a longer ranged charge density wave [47], or surface stress reduction [48], the system attempts to reach an equilibrium state which minimizes the surface free energy.

In this chapter we report on structures formed by the influence of oxygen on high-Miller-index copper surfaces. The reconstructions formed by O on low-index Cu are already well-known, and are reviewed in Ref. [49]. On Cu(110), O forms a (2×1) reconstruction [50] at low coverage and a $c\,(6\times2)$ reconstruction at higher coverage [51]. On Cu(001), O induces only a $(2\sqrt{2}\times\sqrt{2})$ reconstruction [52] (although other superstructures had preliminarily been reported as discussed in Ref. [52]). A common structural feature of these reconstructions [53] is the formation of Cu–O chains on these surfaces. The O atoms are fourfold coordinated, with all O–Cu bond lengths about 1.85 Å. These features are conspicuously similar to the characteristics of bulk cuprite, Cu_2O, except the O atoms of these reconstructions are not centered in Cu tetrahedra [53]. O on Cu(111) induces a more complex series of reconstructions which are rotated relative to the substrate, yet are comparable to the structure of bulk $Cu_2O(111)$ planes [54, 55]. Recent studies of O/Cu(102)(2×1) have also found evidence for Cu–O–Cu chains on this surface, although the structure has not been fully determined [56, 57]. Similar structures have also been found in the oxidation of Cu alloy surfaces [58, 59] and Cu thin films [60]. One notable exception is that of O/Cu(112), which forms several reconstructions depending on experimental conditions, none of which have the Cu–O–Cu chain feature [61].

Unlike these low-index surfaces, most high-index Cu surfaces do not form stable reconstructions, but rather facet when exposed to oxygen. Most Cu(001) vicinal surfaces form O/Cu(104) facets [62, 63, 64, 65, 66, 67, 68, 69, 70]. Of course, to maintain the surface's macroscopic orientation, other facets must form across the surface as well, such as {001} for the faceting of Cu(106) [70] and Cu(108) [68]. In this thesis we discuss the O-induced faceting of Cu(115), in the temperature range 200° C to 400° C, which forms facets with the (104), (014), and (113) orientations. Since they are crystallographically equivalent, we implicitly include the O/Cu(014) facets in the following discussions of O/Cu(104) unless stated otherwise. This chapter describes the surface structure of these facets as well as that of the clean Cu(115) surface. This faceting was previously observed by Sotto [71] and by Reiter and Taglauer [69, 72]. Chapter 4 describes the kinetics of the faceting process as observed by x-ray diffraction.

Before moving on to the crystallographic structure of the clean and faceted surfaces, we comment on the ability to observe facet structures using surface x-ray diffraction. As discussed in section 1.1.3, crystal truncation rods (CTRs) occur because a surface breaks the periodicity of a bulk crystal. A facet is a small area of the surface with a particular crystallographic orientation which does not correspond to that of the macroscopic surface. Yet it is still a surface; equation 1.15 can apply to the faceted region. In doing so, the unit cell is chosen such that the lattice parameter c is perpendicular to the facet plane (instead of the bulk surface plane, the case for an unfaceted surface). The scattered amplitude from one single facet will be small, proportional to the area of the facet. But if many facets of a given orientation are present on a surface, the scattering from their CTRs will add incoherently and the intensities become large enough to be observed.

The beautiful STM images of Reiter and Taglauer [69] show that the facets formed by exposing Cu(115) to O produce three-sided pyramids across the surface; each side is (at least) moderately well-ordered with well-defined orientations of (104), (014), or (113). One such pyramid is diagrammed in Fig. 3.1a. The three facets are clearly distinguishable in the original micrograph[69], as are the high degree of atomic ordering on the {104} facets and the relative disorder on the (113) facets.

We have observed CTRs from these three facets with surface x-ray diffraction, as demonstrated in Fig. 3.2. Fig. 3.2a is a cross-section through reciprocal space at constant ℓ, parallel to the (115) surface and slightly above a bulk Bragg peak. This surface was prepared by exposing Cu(115) at 300° C to ~ 20 L O_2 (1 L = 1 Langmuir = 10^{-6} Torr sec). No longer is this surface (115)-oriented; if it were, a CTR would pass through the center of this plot at $h = 6$, $k = 0$ (see below). Instead, the plot cuts through three rods, all of which are

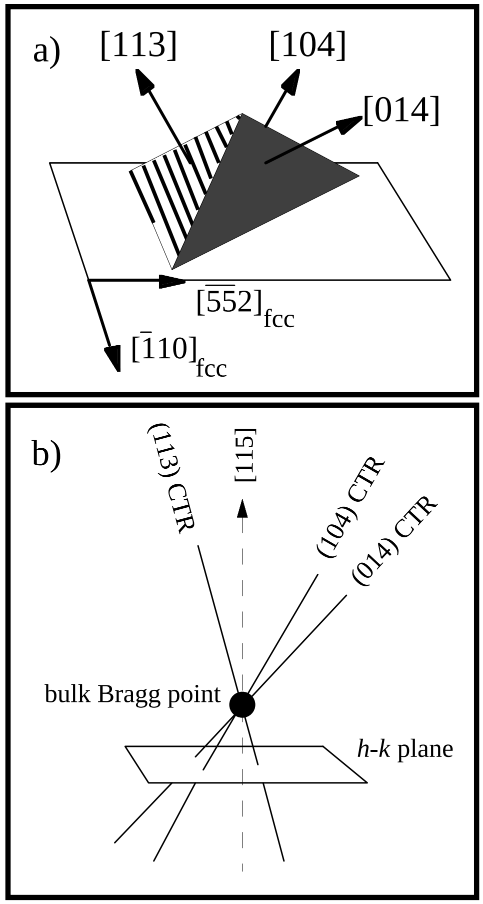

Figure 3.1: a) Schematic real-space model of one faceted pyramid. These structures were observed with STM in Ref. [69]. The surface normals of the (104), (014), and (113) facets are shown. The vertical scale is significantly exaggerated. b) Schematic reciprocal-space diagram of CTRs due to the three facets in a). The ℓ = constant plane below the bulk Bragg peak is the plane of Fig. 3.2b.

angled towards the bulk peak and perpendicular to the plane of their particular facet. On the lower side of the Bragg peak, the peaks are on the opposite sides, as shown in Fig. 3.2b. Fig. 3.1b depicts the constant-ℓ plane cutting through the three CTRs below a bulk peak. The well-defined orientations of the facets permit structure factors to be measured along the rods of each facet; the crystallographic analyses of these facets are in sections 3.3 and 3.4 below.

In labeling the axes for the bulk surface and the two facets discussed in this chapter, we

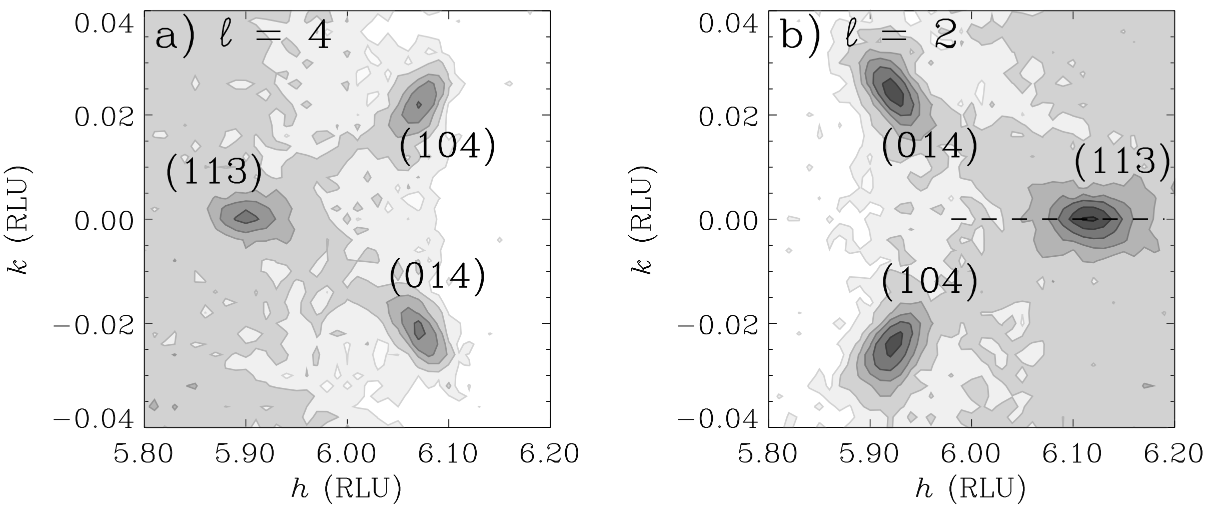

Figure 3.2: a) A cross-section through reciprocal space above the $(603)_{115}$ bulk point, at $\ell = 4$. The three spots are located at the intersection of the $\ell = 4$ plane and the CTRs of the three facets formed by exposing O to Cu(115), as labeled. No (115) rod is visible at $h = 6$, $k = 0$, indicating the surface is entirely faceted. b) The same mesh scan, but now below the Bragg peak, at $\ell = 2$. Each spot is now on the reverse side of the figure. The dotted line roughly indicates the scans used in Fig. 4.2.

follow standard surface science practice of labeling the surface normal as the z axis. In the surface plane, we choose y parallel to the steps on these vicinal surfaces and $+x$ pointing toward an upward step. Thus, our choice of coordinate system changes for each surface. The coordinates x, y, and z are given in units of the appropriate surface unit cell.

3.2 Clean Cu(115) surface structure

Ideal Cu(115) is a regularly stepped vicinal surface of Cu(001). Compact step notation [73] describes its structure as 3(001)×(111), meaning the surface is composed of {001} terraces (three atoms long) separated by <111>-type (closed-packed) steps along the y direction. The angle between the [115] and [001] surface normals is 15.8°. Fig. 3.3 illustrates the bulk-terminated Cu(115) surface, highlighting the three inequivalent atomic sites on the surface

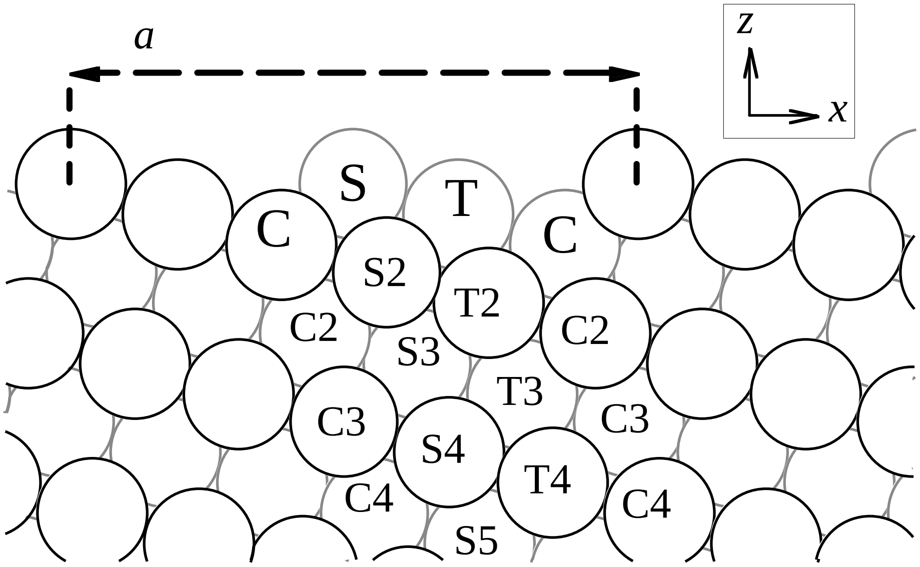

Figure 3.3: Bulk-truncated structure of a clean, ideal fcc(115) surface. z is the surface normal; x runs perpendicular to the steps in the surface plane; y is parallel to the surface steps (and perpendicular to the page). The surface atoms thus have small vertical separations, accounting for the small interlayer spacing ($d_{bulk} = 0.696$ Å). Atoms at the surface are labeled according to their location at the step ("S"), on the terrace ("T"), or at the corner below the next step ("C") [74, 75]. Subsurface atoms are labeled according to the surface atom above them and their depth (in atoms) below the surface (along the column of similar atoms).

[74], which all have different coordination numbers. Atoms on the step sites ("S" in Fig. 3.3) have seven nearest neighbors, while atoms at the terrace sites ("T") have eight, and atoms at the corner sites ("C") have ten. All other atoms are in fully coordinated "bulk-like" sites. In the centered orthorhombic surface unit cell, each atom at (x, y, z) has a crystallographically equivalent atom at $(x + \frac{1}{2}, y + \frac{1}{2}, z)$, in units of the surface unit cell.

Because of the high Miller indices of this surface, the reciprocal space notation is rather complicated. The transformations between standard fcc coordinates and (115) surface coordinates are given by the following matrices:

$$\begin{pmatrix} h \\ k \\ \ell \end{pmatrix}_{(115)} = \begin{pmatrix} \frac{5}{2} & \frac{5}{2} & 1 \\ -\frac{1}{2} & \frac{1}{2} & 0 \\ -1 & -1 & 5 \end{pmatrix} \begin{pmatrix} H \\ K \\ L \end{pmatrix}_{\text{fcc}} \tag{3.1}$$

and

$$\begin{pmatrix} H \\ K \\ L \end{pmatrix}_{\text{fcc}} = \frac{1}{27} \begin{pmatrix} 5 & -27 & -1 \\ 5 & 27 & -1 \\ 2 & 0 & 5 \end{pmatrix} \begin{pmatrix} h \\ k \\ \ell \end{pmatrix}_{(115)} , \tag{3.2}$$

with lattice parameters $a = 13.281$ Å, $b = 2.556$ Å, and $c = 18.783$ Å. Thus, the $(111)_{fcc}$ bulk Bragg peak is now indexed as $(603)_{115}$, as shown in the reciprocal-space map of Fig. 3.4. Bragg peaks are separated in ℓ by 27 reciprocal lattice units. That is, there are other Bragg peaks at $(6,0,30)_{115}$ and $(6,0,\overline{24})_{115}$, although these peaks are far beyond the q-range accessible in this experiment. On the other hand, the interlayer spacing is deceptively small: $d_{bulk} = 0.696$ Å, since there are 27 layers of atoms per unit cell. Atoms in adjoining planes have, of course, significant lateral separation, as seen in Fig. 3.3.

For vicinal surfaces, it is more natural to describe vertical displacements in terms of interatomic separation (projected onto the z axis) than to speak of interlayer spacings. For atoms in adjacent "layers" which have horizontal separations much larger than their vertical separations, the concept of interlayer spacing is less meaningful. The *change* in relative vertical position of an atom in layer i compared to an atom in layer $i + 1$ can be defined as

$$\frac{\Delta z_i}{z_0} = \frac{\delta d_{i,i+1}}{d_{bulk}} = \frac{(z_i - z_{i+1}) - z_0}{z_0}. \tag{3.3}$$

z_i is the vertical position of the atom in the coordinates of the surface unit cell, and, for the Cu(115) surface unit cell, the bulk interlayer spacing $z_0 = \frac{1}{27}$. Use of Δz_i instead of $\delta d_{i,i+1}$ emphasizes that atoms on vicinal surfaces may not be directly above the atom in the next layer down.

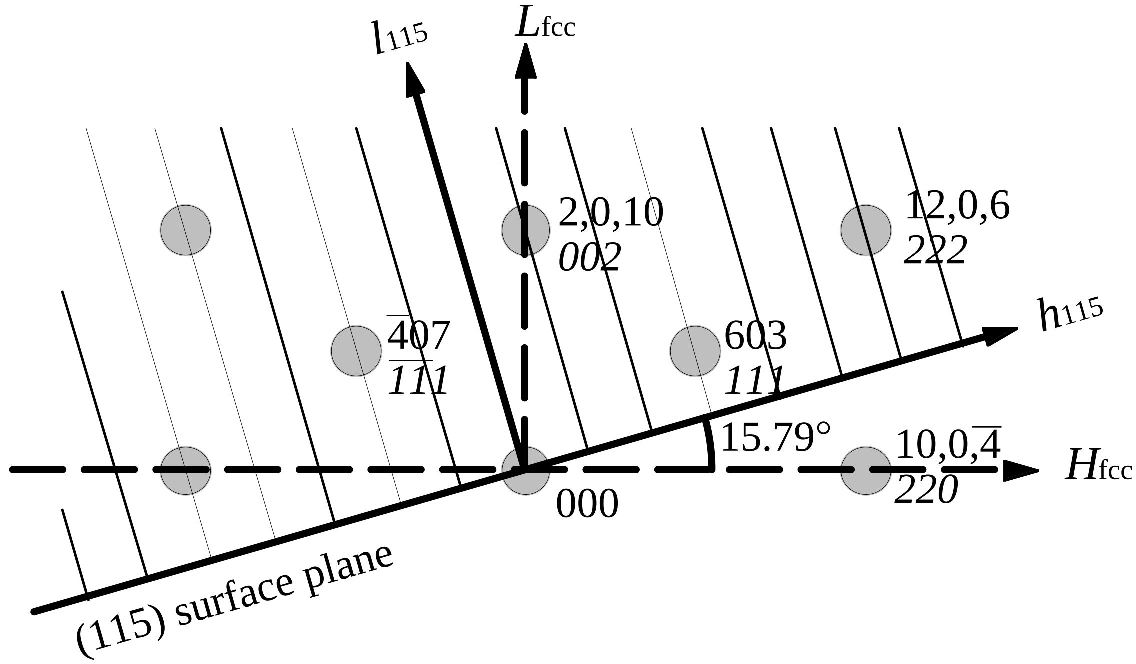

Figure 3.4: Reciprocal space map for an fcc(115) surface, in the $k = 0$ plane. Shaded circles represent Bragg points, labeled in standard fcc units (lower, italics) and 115 surface units (upper, straight).
Axes for standard fcc orientation (dashed) and for 115 surface orientation (solid) are in bold. The narrow, tilted lines represent 115 crystal truncation rods. Note this figure is rotated from Fig. 3.3.

3.2.1 Previous work on Cu(115)

Work on the clean Cu(115) surface originally focused on the stability of this stepped surface, rather than the crystallographic structure. Time-of-flight helium atom scattering by Ernst *et al.* [76] determined that this surface does *not* undergo a roughening transition, as previously thought. Energy analysis was essential to this experiment, given the large amount of inelastic scattering from this surface at high temperatures.

Low-Energy Electron Diffraction (LEED) has been performed on Cu(115), and is interpreted as a complex multilayer relaxation [77]. The measured relaxation between the first and second lattice plane is $\frac{\Delta z_1}{z_0} = -16.5\%$, and relaxations continued to the sixth layer. Table 3.1 lists the results of this experiment. Although the fractional change $\frac{\Delta z_1}{z_0}$ is very

	Percent relaxation $\left(\frac{\Delta z_i}{z_0}\right)$, determined by:				
Layer	LEED [77]	tight-binding calculations [78]	energy minimization calculations [79]	embedded atom calculations [75]	surface x-ray diffraction
1	−13.2	−8.0	−12.7	−9.46	−15.4
2	−6.1	−5.1	−10.3	−7.87	+8.1
3	+5.2	+7.0	+10.8	+8.76	−1.1
4	−0.1	−3.3	−6.3	−4.19	−10.3
5	+2.7	−3.1	–	−4.04	+5.4
6	–	–	–	+3.44	−0.7
7	–	–	–	−1.67	−6.9
8	–	–	–	−1.14	+3.6

Table 3.1: Interlayer relaxations of Cu(115). These were determined by LEED experiments [77], tight-binding calculations [78], energy minimization calculations [79], embedded atom calculations [75], and surface x-ray diffraction (present work). Ref. [75] and the present work also explicitly include lateral displacements.

large, the actual atomic displacement is not so dramatic since, as mentioned above, d_{bulk} is relatively small.

This LEED analysis found, within error bars, no lateral displacements of the Cu atoms, although such relaxations are not *a priori* forbidden. Since no reconstruction was observed in either in-plane direction, we expect on symmetry grounds that atoms remain at $y = 0$ or $\frac{1}{2}$ (grey or black circles in Fig. 3.3). The lack of mirror symmetry in the x direction allows, in general, for atoms to relax in this direction. LEED is typically more sensitive to interlayer displacements and surface x-ray diffraction to lateral displacements, so perhaps the LEED data could be sufficiently fit without including lateral displacements in the surface model.

The structure of Cu(115) has been studied theoretically by Loisel *et al.* [78] using tight-binding calculations, Hammonds and Lynden-Bell [79] using energy-minimization calculations, and by Tian and Rahman [74] and Durukanoglu, Kara, and Rahman [75] using the embedded atom method. All methods found a qualitatively similar relaxation pattern in the interlayer spacing, with $\frac{\Delta z_1}{z_0}$ not as extreme as determined by LEED [77]; results are shown in Table 3.1. More recent embedded atom calculations [80] are in very good agreement with Refs. [74, 75]. Furthermore, Rahman and coworkers [74, 75] found a common characteristic in several Cu(001) vicinal surfaces: the vertical displacements of subsurface (bulklike) atoms follow the trend set by atoms of the topmost layer. The displacement of the surface atoms are repeated inwards with an exponentially decaying scale factor. Multilayer relaxations of this sort are common in surface structure, but vicinal surfaces present a complication: for Cu(115), each atom is almost vertically on top of the atom of the *third* layer below it (besides an offset of $\frac{1}{2}$ in y). Tian and Rahman [74] used the vertical displacements of the top atoms, Δz_m (where m = S, T, or C, the three surface sites defined in Fig. 3.3) to describe the displacements of the lower atoms:

$$\Delta z_{m,n} = \Delta z_m \exp[-\kappa_m (n-1)]. \tag{3.4}$$

n is the depth of the atom beneath the surface (Fig. 3.3), and κ_m is an exponential decay factor. The form of Eq. 3.4 is the general solution of the Poisson equation, which will be the exact solution in the limit of continuum elasticity theory. Although Ref. [74] did not consider lateral displacements, Ref. [75] did, finding the trend of Eq. 3.4 approximately holds. The small displacements in x did not follow any such trend.

Durukanoglu, Kara, and Rahman [75] also calculated the surface phonon spectrum of Cu(115) and similar Cu(001) vicinal surfaces, finding highly anisotropic thermal vibrations at the surface. The in-plane phonon modes perpendicular to the steps were particularly softened, resulting in a large Debye-Waller factor in x for the step atoms (symbol: B_x^S; the subscript represents direction and the superscript identifies the atom). Calculated vibrational amplitudes in x for terrace and corner atoms were progressively smaller, reflecting their greater coordination. Vibrational amplitudes in y were nearly identical for the S, T, and C atoms, and in z the trend was reversed from x, with the corner atoms having the largest mean square amplitude. These results appear consistent with He-atom scattering experiments [81] which mapped out the surface phonon dispersion curves of Cu(115) and found a low-energy longitudinal mode at the zone boundary.

3.2.2 Present experiment and results

In order to determine the surface structure of Cu(115), we have performed a surface x-ray diffraction experiment at beamline X16A of the National Synchrotron Light Source, Brookhaven National Lab. The surface was prepared by chemical polishing, then by cycles of sputtering with 1 keV Ar^+ ions and annealing to 550° C, until terraces on the surface were $\gtrsim$ 700 Å, as determined by the width of the crystal truncation rods. The structure factors, derived from integrated intensities of diffractometer ϕ-scans, were corrected for Lorentz and polarization factors and the variation of the illuminated area on the surface. 123 structure factors along five crystal truncation rods [9] were measured at room temperature using 8.5 keV x rays. Structure factors for negative ℓ are achieved through inversion symmetry using the Freidel relation $F_{hk\ell} = F_{\overline{hk\ell}}$, and crystallographically equivalent structure factors were symmetry averaged together using plane group pm: $F_{hk\ell} = F_{h\bar{k}\ell}$ because of mirror symmetry in y.

Fig. 3.5 displays the structure factors measured from the Cu(115) surface. The dashed line represents the calculated scattering from a bulk-truncated Cu(115) surface; the only fitting parameters are an overall scale factor, a roughness parameter, and one isotropic Debye-Waller factor. The ideal bulk truncation made a reasonable preliminary fit, but the data had clear oscillations which called for a model with atomic displacements and additional Debye-Waller factors for the surface atoms. On this vicinal surface, the most general model has many

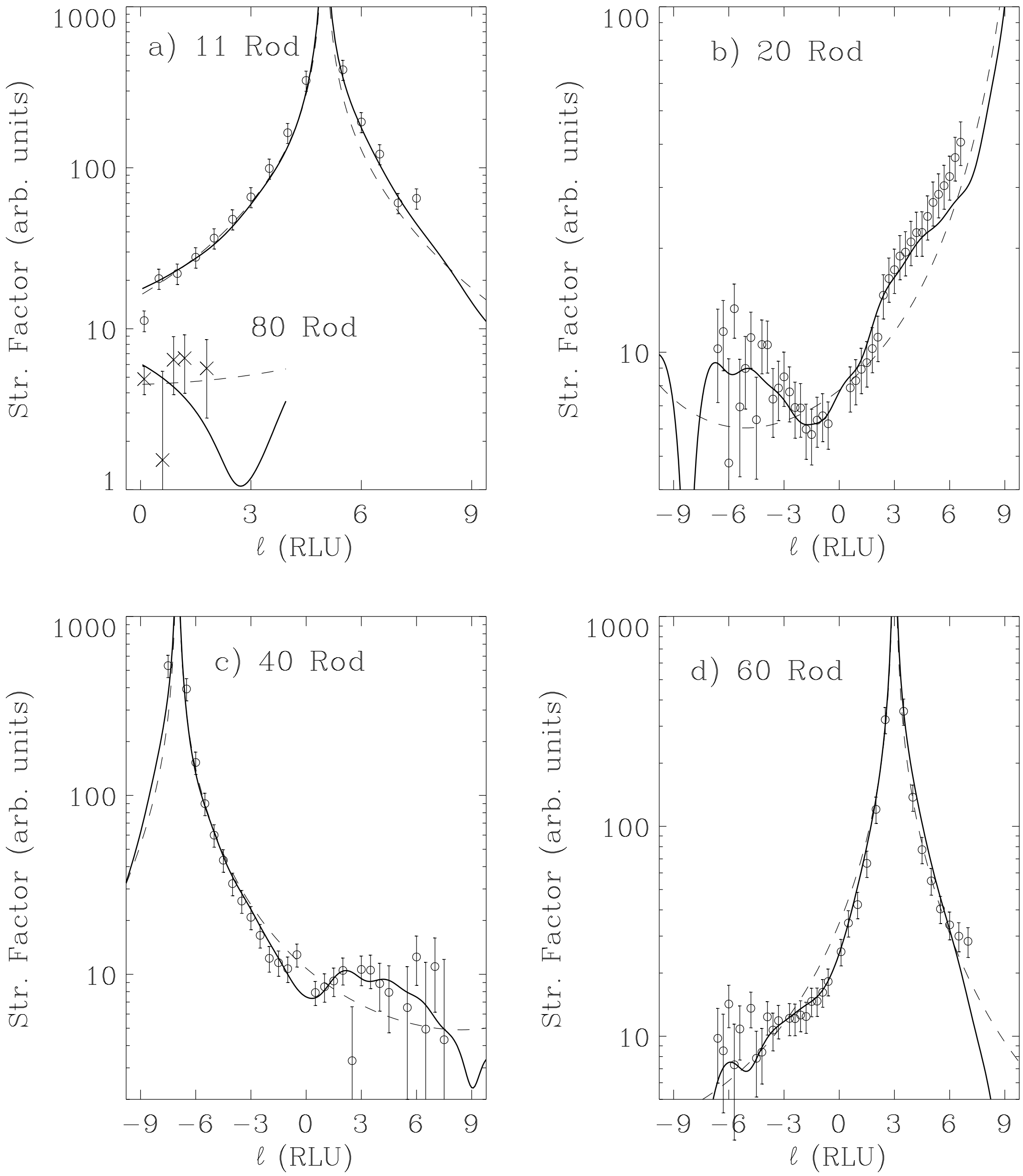

Figure 3.5: Structure factors of the five crystal truncation rods of clean Cu(115). Circles represent data points, the dashed line is a fit for an abrupt bulk termination, without atomic displacements or multiple Debye-Waller factors ($\chi^2 = 2.47$); and the solid line is the best fit as described in the text ($\chi^2 = 1.40$).
a) (11ℓ) rod, whose bulk peak is at $\ell = 5$; also (80ℓ) rod (data marked by $\times$ instead of circles), with bulk peak at $\ell = 13$.
b) (20ℓ) rod, whose bulk peak is at $\ell = 10$.
c) (40ℓ) rod, whose bulk peak is at $\ell = -7$.
d) (60ℓ) rod, whose bulk peak is at $\ell = 3$.

atoms with independent displacement parameters, e. g., 14 free displacement parameters for the top seven layers of atoms (all of these atoms being close to the surface). Refining such a model produced a physically unreasonable fit: the distance from atom S (the step atom) to any of its nearest neighbors was greater than 2.6 Å, compared with the bulk bond length of 2.556 Å; the Debye-Waller factor for this atom also had a large, negative value (which has no physical meaning). Other interatomic distances on this surface became less than 2.2 Å. We conclude that this model provided too many degrees of freedom for the available data.

To attempt a more realistic description of the Cu(115) surface, one can choose to fit only one or two displacements (the approach taken in Ref. [77]), or to provide a constraint to the fitting parameters. In this work, we developed a model which included several free parameters combined with some physical insight. Specifically, this model limited all vertical displacements to the form of Eq. 3.4. Thus, an arbitrary number of atoms were allowed to relax in the z direction and be described by only four parameters: the z displacements of the step, terrace, and corner atoms (Δz_S, Δz_T, and Δz_C respectively) and one decay factor κ, using the definitions of Eq. 3.4 [74, 75]. In practice, we allowed vertical displacements to the fifteenth layer of atoms, and used one common κ instead of separate decay factors for the S, T, and C atomic columns.

In addition to these vertical displacements, displacements in x for the top four atoms and four Debye-Waller factors were needed to satisfactorily model the surface. The values of the refined parameters are listed in Table 3.2, resulting in a fit to the data of $\chi^2 = 1.40$ and graphed as the solid line in Fig. 3.5. The simple constraint of Eq. 3.4 was apparently sufficient to constrain the model and still explain the observations. As expected, the step atom is significantly contracted inward, towards its neighbors, in agreement with the LEED experiment [77]. The fit was not very sensitive to the decay parameter, so κ was fixed at 0.4, as suggested by the numerical calculations and simple force-constant model of Ref. [74].

As predicted by calculations of the phonon spectrum of the Cu(115) surface [75], an

vertical displacements	lateral displacements	Debye-Waller factors
$\frac{\Delta z_S}{z_0} = -0.154$	$\Delta x_S = -0.0009$	$B_x^{ST} = 7.6$ Å^2
$\frac{\Delta z_T}{z_0} = +0.081$	$\Delta x_T = -0.0011$	$B_{yz}^{ST} = 3.3$ Å^2
$\frac{\Delta z_C}{z_0} = -0.011$	$\Delta x_C = -0.0075$	$B^{C,S2} = 1.9$ Å^2
$(\kappa = 0.4)$	$\Delta x_{S2} = 0.0035$	$B^{bulk} = 0.55$ Å^2

Table 3.2: Refined parameters for the physically realistic model of Cu(115), as described in the text, yielding $\chi^2 = 1.40$. Structure factors calculated from this fit are the solid lines in Fig. 3.5. Δx_i is the displacement of atom i from its bulk lattice-defined position in units of the surface unit cell. Δz_j is the vertical displacement of atom j from the atom at the next deepest site compared to the bulk displacement, as defined in Eq. 3.3. Uncertainties were about 0.03 for $\frac{\Delta z}{z_0}$, and 0.001 for the Δx parameters.

anisotropic Debye-Waller factor for the surface atoms significantly improved the fitting. Instead of attempting a detailed comparison with the results of Ref. [75], we limited the number of Debye-Waller factors to the minimum needed to obtain a satisfactory fit. We found that four such parameters were sufficient: two anisotropic Debye-Waller factors (one for the x direction, and one for y and z) shared by atoms S and T; one isotropic factor shared by atoms C and S2; and a value of $B_{bulk} = 0.55$ Å for all other atoms. Additional Debye-Waller parameters did not result in an improved fit. The resulting values are shown in Table 3.2, and do follow the general trend of Ref. [75].

In addition to the above parameters, our model included a roughness factor based on the geometrical model of roughness [9]. The best fit yielded $\beta = 0.51$, a large value even for a metal. However, this, like the large values of $\frac{\Delta z_i}{z_0}$, was due to the very small interlayer spacing of this surface; the root mean square roughness was only 1.44 Å.

The low symmetry of this vicinal surface produced many atoms near the surface which had crystallographically independent x and z coordinates. Simply allowing these coordinates to vary independently did not produce a physically realistic fit, but a model based on elastic interactions did. One effect of including Eq. 3.4 is to limit unrealistic interatomic distances; most of the refined distances in the model ranged from 2.49 Å to 2.57 Å. Prevention of unrealistic interatomic distances can also be addressed by adding an "energy cost" to the goodness of fit parameter. That is, bond lengths (or also bond angles) far from bulk values add to the χ^2 of a model, ensuring a preference for realistic interatomic distances. This procedure has been employed [82] in the solving of complex reconstructions on semiconductor surfaces using the Keating model of interatomic potentials [83]. On the other hand, Eq. 3.4 is, to some extent, an oversimplification of the true multilayer displacements. Surface atoms will likely relax with some deviation from an exponential decay, which this model does not take into account. A more complete structure determination would require data from a greater range of reciprocal space, implying a higher x-ray energy. Unfortunately, more energetic x rays than those used in this experiment would cross the Cu K adsorption edge, resulting in a high fluorescence background and making accurate integrated intensities more difficult to measure without an energy-sensitive detector.

3.3 Structure of O/Cu(104) facets

3.3.1 Previous work on O/Cu(104)

Unlike Cu(11n) surfaces, Cu(104) is a (001) vicinal surface with <010>-type steps, i. e., 4(100)×(010) in compact step notation [73]. The first four rows of atoms are all exposed to the surface (i. e., have reduced coordination); the steps are not close-packed, resulting in surface which is not expected to be thermodynamically stable [84]. Upon exposure to oxygen, however, this surface becomes extremely stable [85]. The O/Cu(104) orientation is so strongly preferred that many nearby Cu(001) vicinal surfaces grow O/Cu(104) facets when exposed to O. Formation of O/Cu(104) facets has been observed by O dosing of many Cu surfaces, including Cu(115) [71, 69], Cu(117) [67], Cu(1,1,11) [67], Cu(1,1,16) [66], Cu(102)

[65], Cu(106) [70], Cu(108) [68, 67], and Cu(418) [66]. As mentioned above, other facets must also form in order to maintain, on average, the macroscopic orientation of the surface.

Due to the <010> orientation of the steps of the (104) surface, the lateral separation of Cu step atoms (along a step) is 3.61 Å. This exposes gaps along the step edges which provide an ideal adsorption site for O, since 1.85 Å ($\approx$ 3.61 Å /2) is the Cu–O bond length in Cu_2O and in several O-induced Cu reconstructions [53]. In fact, the O–Cu–O linear chains which form along these steps are often considered the stabilizing building block of the O/Cu(001)$(2\sqrt{2}\times\sqrt{2})$, O/Cu(110)$(2\times1)$, and O/Cu(110)$c\,(6\times2)$ reconstructions [53]. (Our model of the O/Cu(104) surface, in Fig. 3.7 below, shows the surface unit cell and labels the atomic rows.)

Despite the importance of the (104) surface in the O on Cu system, a full structural determination has not been performed, and studies to date remain ambiguous. Algra *et al.* [86] found, using low energy ion scattering, only one type of O adsorption site in Cu(104) for low O exposures, concluding that O_2 adsorbs dissociatively into the hollow sites of the steps. A photoelectron diffraction study by Thompson and Fadley [85] confirmed that O resides at the two-fold step sites at low exposure, but at higher coverage also occupies a (001) terrace site, as proposed by Perdereau and Rhead [64]. More recently, Robinson, Vlieg, and Ferrer [52] hypothesized that O would sit in the hollow sites of the first and third Cu rows, and that the fourth Cu row would be missing; the (001) terraces on the vicinal surface would then have a structure similar to the $(2\sqrt{2}\times\sqrt{2})$ reconstruction of O/Cu(001) (schematically diagrammed in Fig. 3.7c). In the $(2\sqrt{2}\times\sqrt{2})$ reconstruction, the O atoms are fourfold coordinated; if O atoms sit at the center of the first and third-row hollow sites of *unrelaxed* Cu(104), then the O atoms in the third row have five Cu neighbors *unless* the fourth Cu row is removed. Rutherford backscattering and channeling experiments [71, 87] were not able to directly observe O on the Cu(104) surface, but did find a large outward expansion of the top atomic layers of ~ 0.3 Å. A missing row was not needed to interpret this data, yet the data were consistent with the third or fourth row missing.

Several STM studies have examined the structure of O/Cu(104) facets formed by exposing various Cu(001) vicinal surfaces to O. Lloyd and Woodruff [68] initially labeled the O/Cu(104) facets of Cu(108) as missing the *second* Cu row, based on one low-resolution STM image. Knight, Driver, and Woodruff [70] reinterpreted that image as more likely missing the fourth row of Cu, consistent with their higher quality images of O/Cu(104) formed by faceting of Cu(106). Reiter and Taglauer [69] interpreted their images of O/Cu(104) from the faceting of Cu(115) as missing the fourth Cu row.

3.3.2 Present experiment and results

In order to conclusively determine the surface structure of O/Cu(104), we have performed surface x-ray diffraction on the (104) [and equivalent (014)] facets. The faceted surface was prepared by exposing the clean Cu(115) surface (prepared as described in section 3.2.2) to ~50 L O_2 at 308° C. Faceting was observed with the x rays, as described in Chapter 4, until (104), (014), and (113) facets had formed.

For this preparation, the coherence length in x (perpendicular to the steps) on the (104) facets was approximately 400 Å, as judged by CTR halfwidths; in y, the coherence length was approximately 700 Å. These lengths on the (113) facets were approximately 300 Å in x by 1000 Å in y. These dimensions varied with preparation conditions (i. e., temperature, O_2 partial pressure, total O_2 dose). All structure factor measurements were performed after O dosing ended and the sample cooled to room temperature.

The crystal truncation rods arising from these facets were no longer perpendicular to the Cu(115) surface, but instead each set of rods were perpendicular to the facet plane from which they arose, as shown in Fig. 3.1. The (104) and (014) CTRs are not parallel to the plane of Fig. 3.4; the (113) CTRs are in this plane, but are tilted 25.2° from [001]. To index these rods, we switched from (115) surface notation to the notation of the particular facet.

The reciprocal space transformation from standard fcc units to the (104) surface units is given by

$$\begin{pmatrix} h \\ k \\ \ell \end{pmatrix}_{(104)} = \begin{pmatrix} 4 & 0 & 1 \\ 0 & 1 & 0 \\ -1 & 0 & 4 \end{pmatrix} \begin{pmatrix} H \\ K \\ L \end{pmatrix}_{\mathrm{fcc}} , \tag{3.5}$$

or inversely,

$$\begin{pmatrix} H \\ K \\ L \end{pmatrix}_{\mathrm{fcc}} = \frac{1}{17} \begin{pmatrix} 4 & 0 & -1 \\ 0 & 17 & 0 \\ 1 & 0 & 4 \end{pmatrix} \begin{pmatrix} h \\ k \\ \ell \end{pmatrix}_{(104)} . \tag{3.6}$$

With this transformation, $(111)_{fcc} = (603)_{115} = (401)_{104}$. Bulk peaks for the (104) surface are separated in ℓ by 17 reciprocal lattice units, and are connected by CTRs perpendicular to the (104) surface. In this tetragonal unit cell, $a = c = 14.90$ Å; $b = 3.615$ Å.

Since the average surface orientation, across many facets, is still (115), $\ell = 0$ no longer represents the plane of grazing incidence or exit for the x rays relative to the (104) planes. For some rods, measurements can be made with the grazing incidence geometry for $\ell < 0$. In other cases, $\ell \sim 0$ is inaccessible. But for most of the $\ell < 0$ measurements in Fig. 3.6, we use the inversion symmetry $|F_{hk\ell}| = |F_{\overline{hk\ell}}|$.

Along with structure factors from O/Cu(104), we measured the structure factors from the crystallographically equivalent O/Cu(014) facets, finding, as expected, the data from both facets agree well. Therefore, to achieve a better data set we averaged the measurements from the two facets together, along with the symmetry equivalents from each facet. In all, we measured 319 structure factors using 7.9 keV x rays, which symmetry average to 127 data points (average agreement = 5.2%) along the five inequivalent rods shown in Fig. 3.6.

The structure factors along each truncation rod are strongly modulated, indicating a drastic modification of the surface structure away from a simple bulk truncation (represented as the dashed line in Fig. 3.6). Although the oscillations may be suggestive of a missing row,

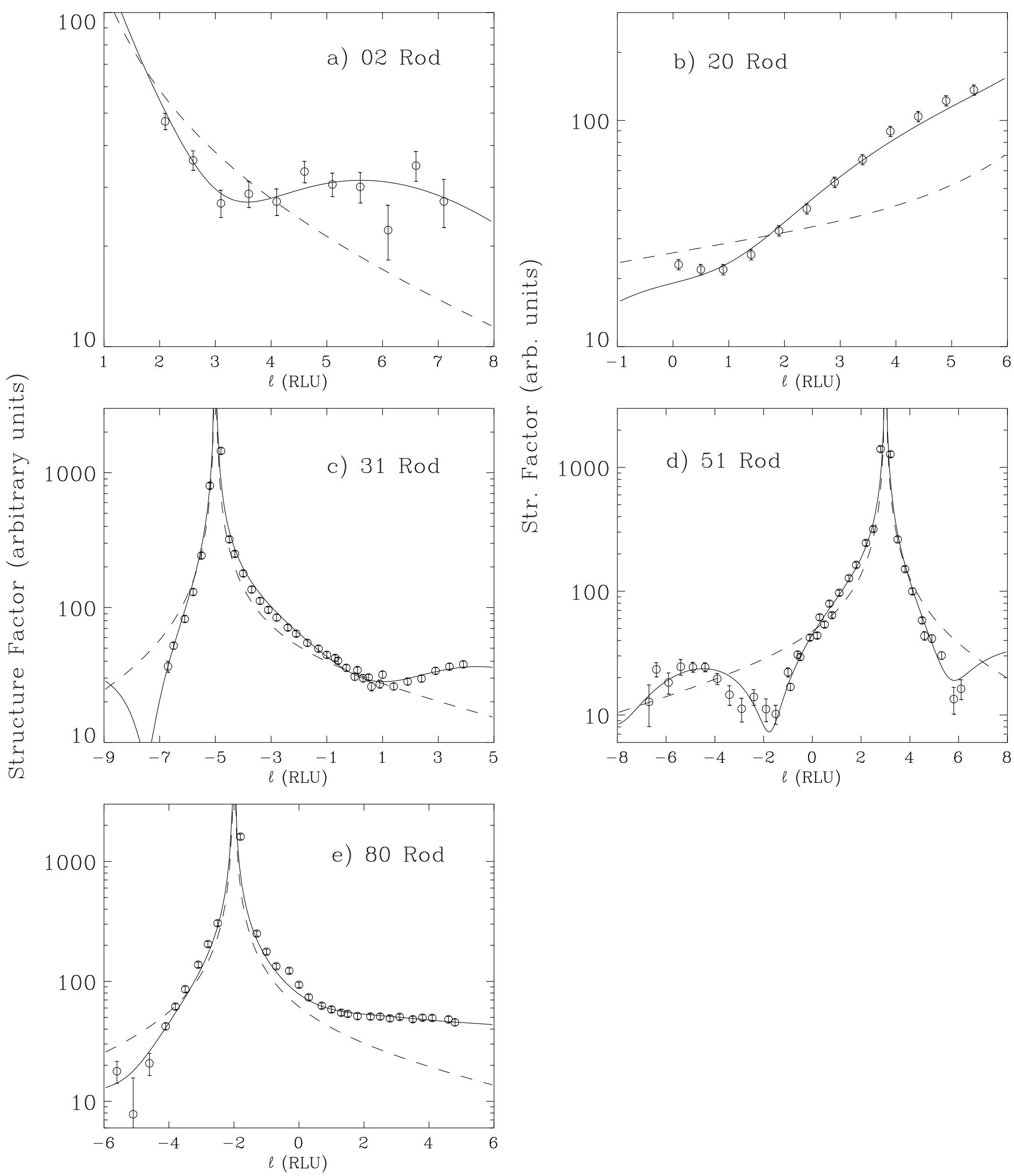

Figure 3.6: Structure factors of the five CTRs of O/Cu(104) facets. Circles represent data points, the dashed line is a fit for an abrupt bulk termination, without atomic displacements or multiple Debye-Waller factors ($\chi^2 = 37.3$); and the solid line is the best fit as described in the text ($\chi^2 = 5.5$).
a) (02ℓ) rod, whose bulk peak is at $\ell = 0$.
b) (20ℓ) rod, whose bulk peak is at $\ell = 8$.
c) (31ℓ) rod, whose bulk peak is at $\ell = -5$.
d) (51ℓ) rod, whose bulk peak is at $\ell = 3$.
e) (80ℓ) rod, whose bulk peak is at $\ell = -2$.

atom	layer i	Δz_i	Δx_i	Debye-Waller factors
O	1	+0.028	−0.003	∼0
O	3	+0.015	+0.016	∼0
Cu	1	+0.025	−0.0157	1.8 Å^2
Cu	2	+0.019	+0.0125	1.8 Å^2
Cu	3	+0.023	+0.0022	1.8 Å^2
Cu	4	–	+0.0046	0.55 Å^2
Cu	5	–	+0.0036	0.55 Å^2

Table 3.3: Refined parameters for O/Cu(104) surface structure, resulting in $\chi^2 = 5.5$. Displacements are in fractions of the surface unit cell ($a = c = 14.90$ Å).
For Cu atoms, displacements are relative to bulk-inferred positions. Displacements for O atoms are relative to the Cu atoms of the same layer (besides the displacement of $\frac{1}{2}$ in y). Uncertainties for Cu atom displacements are $\sim 2 \times 10^{-3}$ for Δz_i, and $\sim 1 \times 10^{-3}$ for Δx_i, and about twice that for O atoms.

no such structure fits the oscillations on all five rods. Instead, our best fit to the data is a model with *all rows present*, and O atoms in the hollow sites of the first row (step edge) and third row (terrace). The displacements of the atoms in the first five rows are listed in Table 3.3, with calculated structure factors displayed as solid lines in Fig. 3.6. Excluding the O atoms from the model, while refining the same number of Cu displacements, results in a χ^2 value more than double that of our best model.

In our model of the surface, the first three rows of atoms relax upwards, away from the bulk. The average spacing between atoms in the top three rows and atoms in lower layers increases by ∼9%, fully consistent with ion channeling studies [87]. With the first three rows expanding away from the bulk, the comparison with the O/Cu(001)$(2\sqrt{2} \times \sqrt{2})$ superstructure (Fig. 3.7c) remains partially valid, even without the fourth row absent. Apparently, the expansion of the first three rows carries a lower energy cost than removing the fourth row.

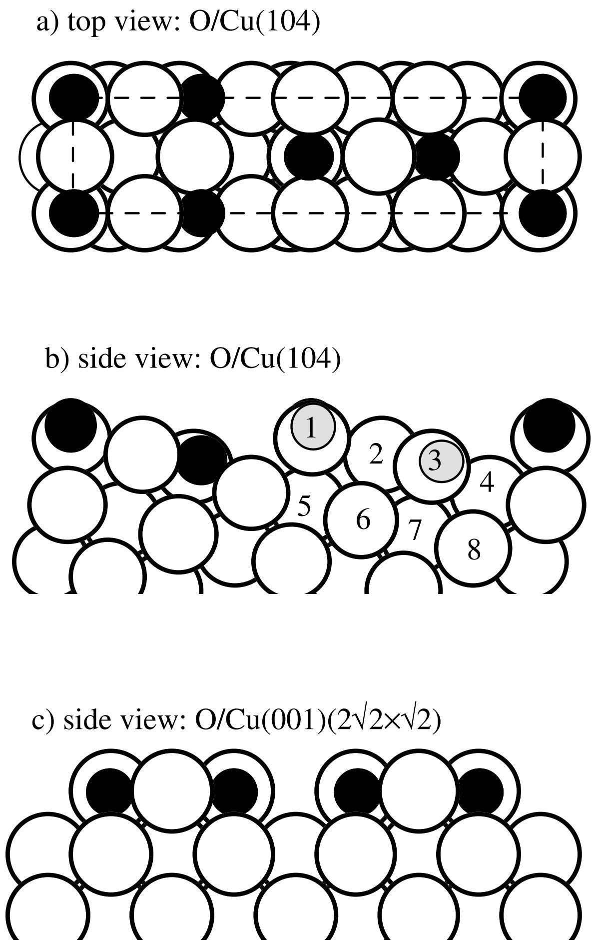

Figure 3.7: a) Plan and b) side views of refined O/Cu(104) surface structure. Cu atoms are hollow; O atoms are filled. Gray atoms in b) are O atoms hidden by Cu. The surface unit cell is outlined in a), and the rows are numbered in b).
c) Side view of (unrelaxed) O/Cu(001)($2\sqrt{2} \times \sqrt{2}$) structure, for comparison.

Views of the relaxed structure are shown in Fig. 3.7.

One notable result of this analysis is that the facets are, within error, completely smooth: $\sqrt{\sigma^2} = 0 \pm 0.1$ Å, indicative of the stability of the O/Cu(104) facets. That is, on the length scale of the facets, the steps on the surface are straight (unkinked) and unbunched, in agreement with the micrographs of Reiter and Taglauer [69]. While defects such as dislocations and impurities on the clean surface might be sites where facets nucleate, they will not occur on the facets themselves, resulting in very smooth facet surfaces.

Besides a Debye-Waller factor for the bulk Cu atoms of $B_{bulk} = 0.55$ Å^2, the Cu atoms of the first three rows had a separate factor, $B_{surface} = 1.8 \pm 0.2$ Å^2. The refined Debye-Waller factor of the O atoms was zero within error bars. In all, four displacement parameters were used for O atoms and eight for Cu atoms. Due to the fewer electrons in O than in Cu and the correspondingly smaller form factor, the positions of the O atoms are determined with slightly lower certainty than the Cu positions. Despite this model's excellent ability to reproduce the modulations of the structure factor along all five rods, the goodness-of-fit parameter is relatively large: $\chi^2 = 5.5$. We feel this is due not to any deficiency in the model, but to an underestimation of the error bars associated with the highly reproducible data. The χ^2 test weights each data point with the inverse square of the error, yielding a high goodness-of-fit measure even for good fits to data with small uncertainties.

We do find one striking dissimilarity with the O/Cu(001)$(2\sqrt{2}\times\sqrt{2})$ structure, in that the two O sites (in the first and third rows) are inequivalent. The O in the third row (terrace site) is four-fold coordinated with bonds ~1.84 Å to the Cu atoms in the second, third, and fourth rows; this is almost a planar structure quite unlike the O coordination on the $(2\sqrt{2} \times \sqrt{2})$ structure or in bulk Cu_2O. The Cu–O–Cu bond angles for this O (row 3) are 160° parallel to the step edge (both Cu atoms in row 3) and 152° perpendicular to the step (Cu atoms in rows 2 and 4). The O in the first row (step-edge site) is only two-fold coordinated; it is located 1.85 Å from the adjoining Cu step atoms, but then >2.4 Å from the next nearest Cu atoms. Cu–O chains, without the fourfold coordination of O, are thus the main feature at this O site. The Cu–O–Cu bond angle along this chain (parallel to the step) is 154°. Table 3.4 details the nearest-neighbor Cu–O bond lengths resulting from our fit. This marked asymmetry in binding sites is not too surprising; on this stepped, vicinal surface, the O adsorption sites should not be degenerate as are the sites on the symmetrical $(2\sqrt{2} \times \sqrt{2})$ surface. The steps on this vicinal surface produce the asymmetry in O adsorption sites observed in this work and previous studies [86, 85]. We expect this asymmetry, not present on ideal (non-miscut)

O atom site	Cu location	d_{O-Cu} (Å)	coordination
step (row 1)	row 1	1.855	2
	row 2	2.410	1
	row 5	2.540	1
terrace (row 3)	row 2	1.847	1
	row 3	1.837	2
	row 4	1.842	1
	row 6	2.420	1

Table 3.4: O–Cu bond lengths for the two O adsorption sites on Cu(104), with uncertainties of about 0.04 Å, based on refined atomic coordinates (Table 3.3). In contrast, if the surface Cu atoms were unrelaxed and the O atoms were centered in the hollow spot of the step or terrace, then $d_{O-Cu} = 1.807$ Å for each bond length in the table.

O/Cu(001)($2\sqrt{2} \times \sqrt{2}$), significantly affects any rehybridization of Cu–O bonds [88]. This should be apparent in valence-band spectroscopy and in any future theoretical calculations which compare the total energies of the various O/Cu(104) surface structure models.

3.4 Structure of O/Cu(113)(3×1) facets

3.4.1 Previous work on O/Cu(113)

In contrast to the heavily studied O/Cu(104) system, very little work has been published regarding O/Cu(113), and most of that has concentrated on the (113) facets produced by exposing Cu(115) to oxygen. STM images by Reiter and Taglauer [69] show a moderately disordered structure on the (113) facets, with stripes about two atoms wide running parallel to the y direction. These stripes appear to be separated by about four monatomic Cu(113) steps; however, variations in stripe width and separation are clearly visible across the larger area scans. Along a stripe, atoms appear to be grouped in "blocks" about three atoms long, with gaps between the blocks about 1.6 Å wide. Occasional bright spots on the blocks were interpreted as "superatoms" elevated $\sim$ 0.8 Å above the other atoms in the block. Based on the separation of stripes, length of blocks, and relative positions of neighboring "superatoms," Reiter and Taglauer described this surface as a $c\,(12 \times 7)$ reconstruction.

Milne [89] also observed the formation of (113) facets due to O adsorption on two vicinal Cu surfaces. Electron microscopy indicated that O adsorption caused Cu(315) to form (305) and (113) facets, and RHEED determined that O caused Cu(112) to facet to (223) and (113) orientations [89]. No structure was proposed for these facets, and as they appeared only occasionally, they were likely metastable. During O_2 dosing on a single crystal Cu(113) surface, Fu and Somorjai [90] observed a $p\,(2 \times 1)$ reconstruction for O coverages of 0.4 to 0.5 monolayers, which reduced to (1×1) at higher coverages. Two nondegenerate O adsorption sites were identified based on desorption asymmetries, but no structural study was performed.

3.4.2 Present experiment and results

The disordered nature of the O/Cu(113) facets precluded the possibility of a full crystallographic analysis, yet as Fig. 3.2 clearly shows, (113) CTRs were present in our data; the surface was, to some degree, flat and ordered. As described in section 3.3.2 for the case of O/Cu(104), we measured structure factors along six CTRs, which symmetry averaged to the four shown in Fig. 3.8a-d. Furthermore, we found a (3×1) reconstruction, indicating an ordered superstructure in x *but not in* y. Some in-plane ($|\ell| \lesssim 1$), third-order structure factors are shown in Fig. 3.8e, while Fig. 3.9 plots structure factors of six fractional order rods. Care was taken during measurement to exclude contamination from third order harmonics in the x-ray beam; such features were much narrower and more intense than the superstructure rods, and therefore straightforward to isolate. In all, 300 structure factors were measured, symmetry averaging to 218 inequivalent points with an average agreement of 5.9%. The conversions between standard fcc coordinates and (113) surface coordinates are given by the matrices

$$\begin{pmatrix} h \\ k \\ \ell \end{pmatrix}_{(113)} = \begin{pmatrix} \frac{3}{2} & \frac{3}{2} & 1 \\ -\frac{1}{2} & \frac{1}{2} & 0 \\ -1 & -1 & 3 \end{pmatrix} \begin{pmatrix} H \\ K \\ L \end{pmatrix}_{\mathrm{fcc}} \tag{3.7}$$

and

$$\begin{pmatrix} H \\ K \\ L \end{pmatrix}_{\mathrm{fcc}} = \frac{1}{11} \begin{pmatrix} 3 & -11 & -1 \\ 3 & 11 & -1 \\ 2 & 0 & 3 \end{pmatrix} \begin{pmatrix} h \\ k \\ \ell \end{pmatrix}_{(113)} \tag{3.8}$$

with resulting lattice parameters $a = 8.477$ Å, $b = 2.556$ Å, and $c = 11.989$ Å.

Since all third-order rods are present (not just $3h + k =$ integer), the (3×1) reconstruction was noncentered. Thus, each (bulklike) layer of the surface contained six symmetry-inequivalent atoms. The modulation of the fractional order rods in Fig. 3.9 indicated multilayer relaxations were important in the structure of this reconstruction. The refinement of this many atomic positions presents a daunting task even for a well-ordered surface; the disorder made a complete crystallographic description unfeasible.

While our model does not determine all atomic positions on this surface, it does succeed in describing some features of these facets. We indeed found that a model containing stripes of Cu atoms fit the data best, in agreement with the STM work [69]. However, the STM also showed the atoms in the stripes did not have well-defined y values. The complete absence of superstructure reflections in k agreed with our interpretation of the STM images, that the stripes had no long-range order in the y direction. Our model attempted to account for the disorder in y by performing an incoherent average (summing of intensities) over two model surfaces. In each surface, the atomic positions were identical except for three Cu atoms, which exchanged y values. That is, if for one model surface, one "disordered" atom was located at $(x, 0, z)$ then for the other, the atom was at $(x, \frac{1}{2}, z)$. This model is an obviously limited attempt at treating the surface's disorder, and ignores the variations in stripe width

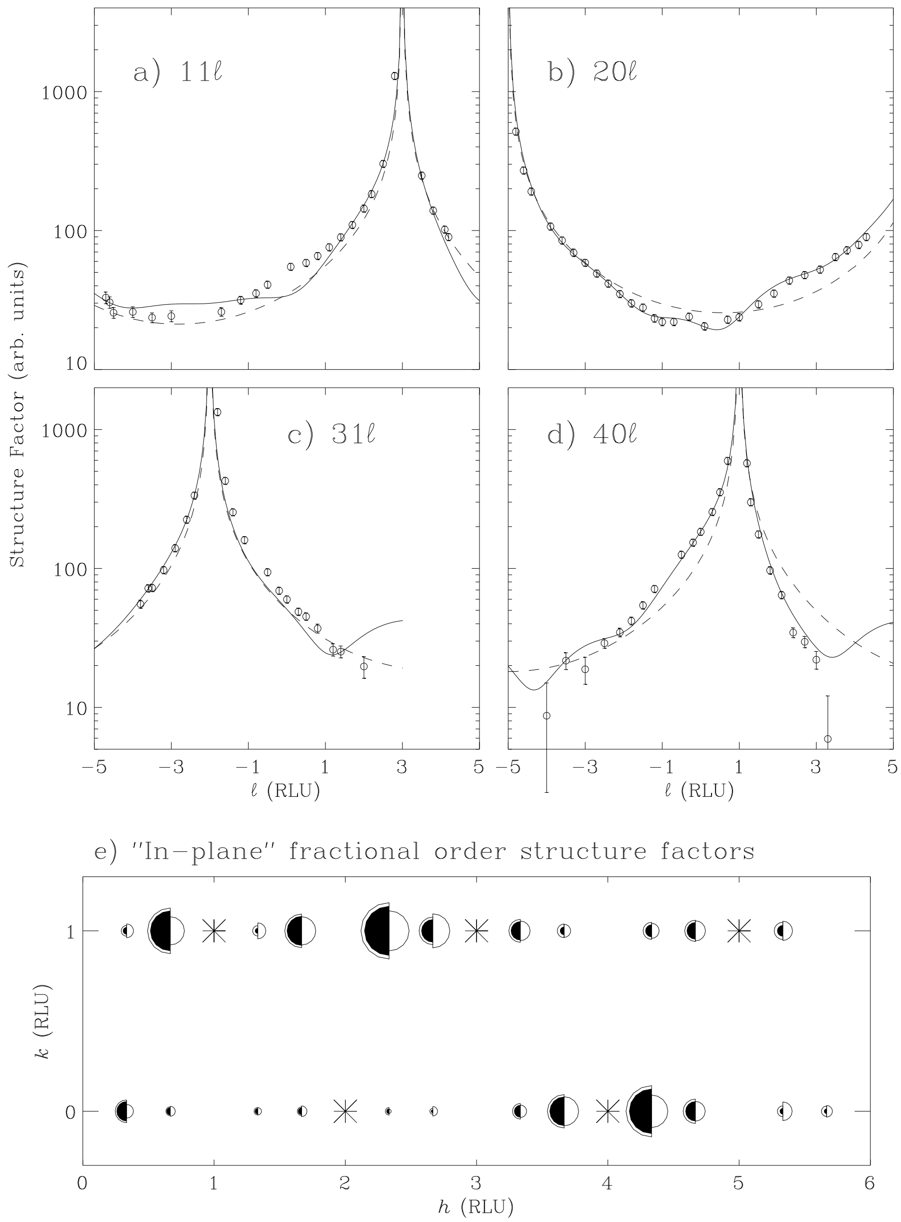

Figure 3.8: a-d) Structure factors of the four CTRs of O/Cu(113) facets. Circles represent data points; dashed lines, the fit for an abrupt (1×1) bulk termination; and solid lines, the best fit as described in the text. Bulk peaks are located at (113), $(20\overline{5})$, $(31\overline{2})$, and (401).
e) Structure factors for in-plane third-order reflections ($|\ell| \lesssim 1$). On the left are shaded semicircles whose radii are proportional to the measured structure factors, with the hollow, outer semicircles representing the error bars. On the right are values calculated from the best fit. Asterisks represent points where CTRs pass through the surface plane.

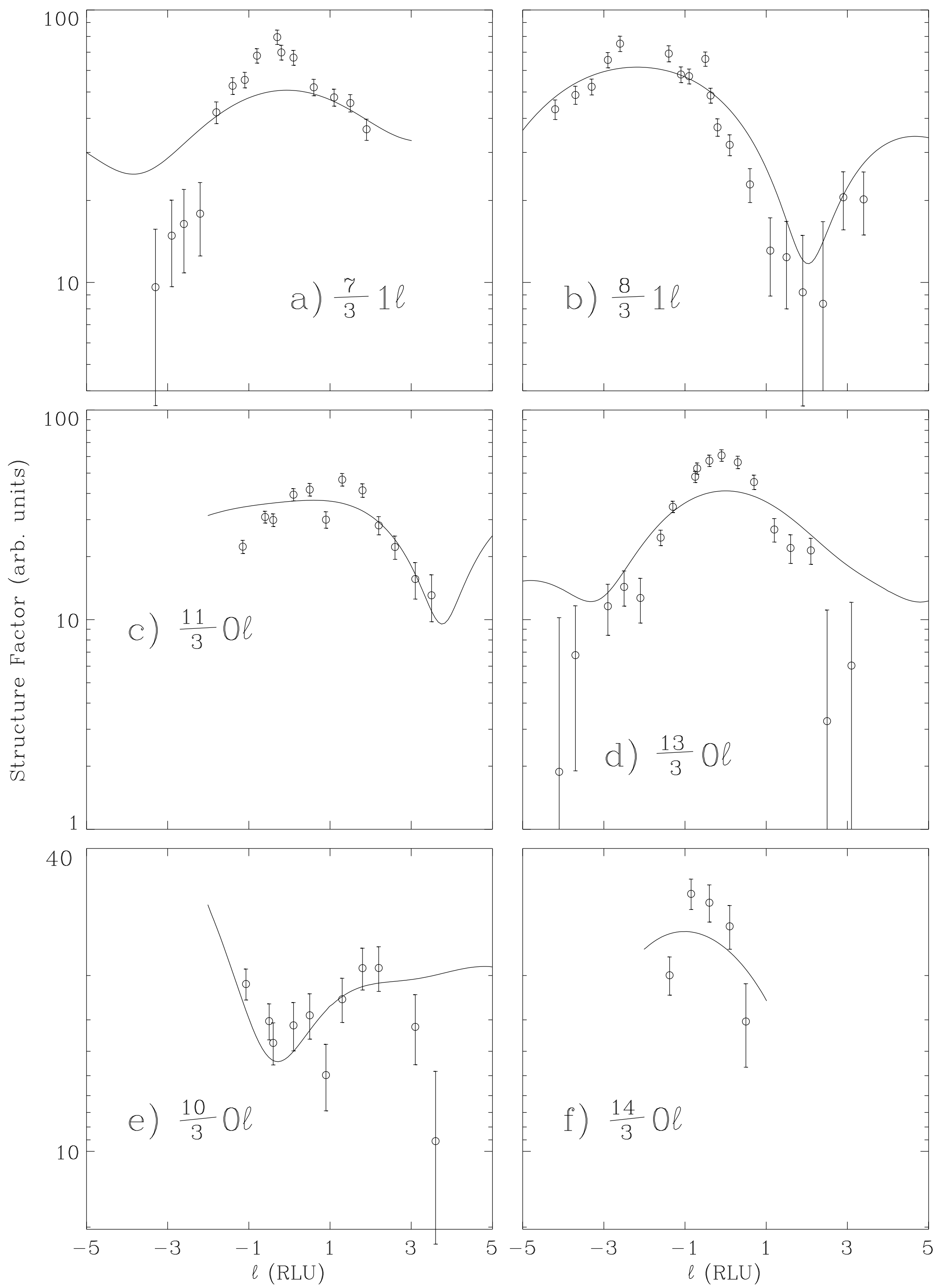

Figure 3.9: Structure factors measured along third-order rods from O/Cu(113)(3×1) facets. The circles are the measured data, and the lines are the best fit from the disordered stripe model discussed in the text.

observed by STM [69]. The significant disorder on this surface makes it unlikely that any "superatoms" would be at well-defined crystallographic sites; attempts to refine positions of additional atoms on top of the stripes were unsuccessful.

Like the O/Cu(104) facets, described in section 3.3.2, which were smooth as measured by x rays, the O/Cu(113)(3×1) facets had $\beta = 0 \pm 0.01$, using the geometrical model of roughness described in Ref. [9] and section 1.1.4. One Debye-Waller factor of $B = 0.5$ Å^2 sufficed for all atoms; this model is not detailed enough for the relatively fine effects of additional Debye-Waller factors. Based on interatomic distances, three atoms per unit cell were tentatively identified as O, with the appropriate form factor used in calculation of the best fit. In the refinement of the atomic positions, 19 Cu atoms were allowed to relax from their bulk-defined positions, besides the three O atoms and the three Cu atoms "disordered" in y. Fig. 3.10 is a side view of the refined positions of the atoms in our disordered stripe model. The structure factors calculated from this model are shown with the data in Figs. 3.8 and 3.9.

The goodness of fit parameter for the disordered stripe model is $\chi^2 = 7.9$; while certainly leaving room for improvement, this was the best achievable given the disorder on the surface. Most of the disagreement is associated with the third-order rod measurements rising and falling more abruptly than the model predicts. This is a symptom of an over-simplified model: deeper layer displacements are needed to increase the modulation, but would introduce many additional fitting parameters. It is not clear that such a procedure would produce reliable results. We expect our refined positions are the result of the ensemble average naturally performed by diffraction across many unit cells. Since the structure of the stripes is expected to vary in y (due to the blocks and possible "superatoms" observed with STM [69]), the positions of the atoms beneath the stripes are also likely to vary with y. The results of the simple disordered stripe model picks out the laterally averaged position of each atom.

Applying surface x-ray diffraction to O/Cu(113) facets has helped elucidate the struc-

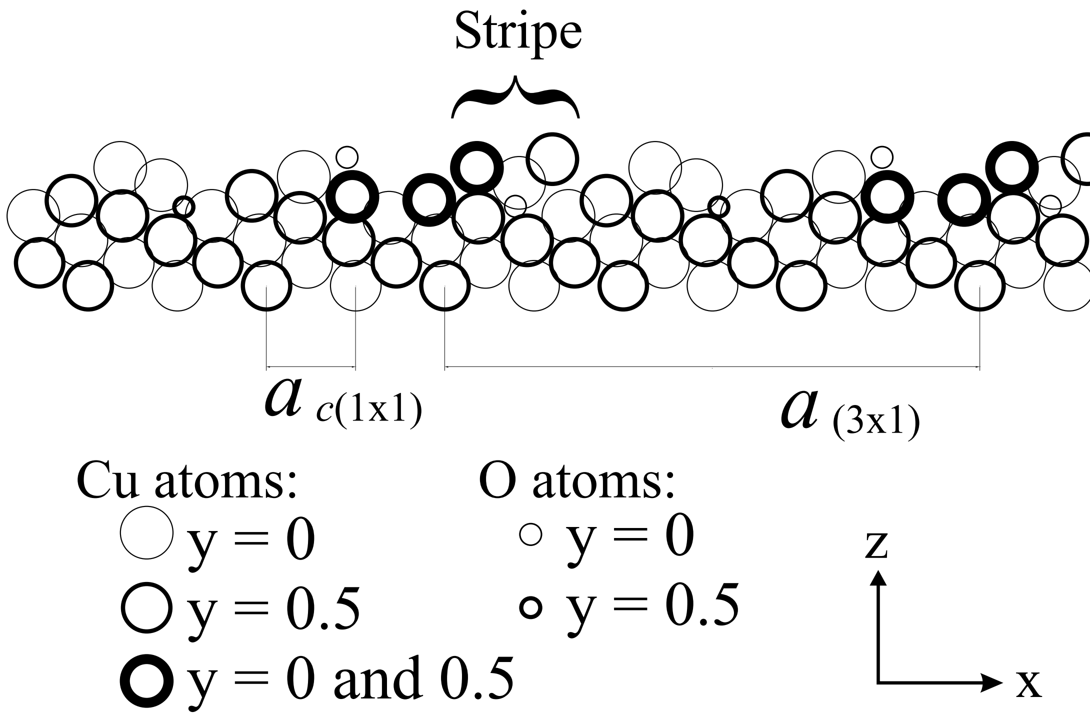

Figure 3.10: Side view of refined O/Cu(113)((3×1) surface structure. O atoms have a smaller diameter than the Cu atoms. The thickness of the atoms shows whether they are located in the $y = 0$ or $\frac{1}{2}$ plane, or both (to model the disorder on the surface).
The bottom two rows of atoms are unrelaxed from their bulk positions.

ture of these facets. Specifically, a noncentered (3×1) reconstruction was observed, and the measured data were most consistent with a disordered stripe model. However, the disordered nature of this surface precluded a full crystallographic analysis, therefore limiting the conclusions which could be drawn. For a more complete understanding of O/Cu(113), other surface science techniques, each with its own advantages and limitations, must be applied to this system.

3.5 Conclusion

This chapter describes three surface structure determinations, of a clean vicinal surface and of two oxygen-covered facets. While the determination of the O/Cu(104) facet structure demonstrates the power of surface x-ray diffraction to detect subsurface atoms, the determination of the Cu(115) surface structure and the O/Cu(113)(3×1) facet structure demonstrate the more common situation, of the need for multiple, complimentary surface science techniques (theoretical as well as experimental) to fully describe a surface. In the case of O/Cu(113)(3×1), additional work remains on both preparation and analysis of this disordered structure before a complete description can be reached.

We expect that our results for the O/Cu(104) facets should also describe the structure of bulk O/Cu(104) single crystal surfaces. As discussed in Chapter 4, O/Cu(104) is one of the most stable O-covered Cu surfaces, and the formation of O/Cu(104) facets appears to drive the faceting of this system. It is conceivable that these facets may, in fact, be closer to the lowest-energy structure of O on Cu(104) than even O/Cu(104) from bulk single crystals (although surface x-ray diffraction experiments by Vleig *et al.* for such a sample resulted in comparable data [91]). Bulk crystals may be hampered by misorientation, impurities, or incomplete O adsorption, while the facets are less susceptible to such limitations. In our preparation we are, in effect, growing the {104} substrate along with its surface. We note that such a growth method is compatible with any surface science technique with sufficient spatial or orientational resolution, in order to resolve the signal from the O/Cu(104) and O/Cu(014) facets with that from the O/Cu(113) facets.

In contrast, the (113) facets are formed primarily because the surface must maintain its macroscopic (115) orientation. These facets are significantly disordered and likely strained. Indeed, the reconstruction formed by O on a Cu(113) single crystal is supposedly quite different from the disordered stripes observed on the facets [69, 90]. Nevertheless, now that several structures of O on Cu surfaces have been experimentally determined (and several other surfaces have been found to be unstable against faceting), the time is ripe for theoretical work to more completely describe the interactions of oxygen with both flat and stepped Cu surfaces.

Chapter 4

O-induced spinodal decomposition of Cu(115)

4.1 Introduction

Atomic adsorption at surfaces is an important yet incompletely understood process, particularly in cases where adsorption induces a major rearrangement of the surface structure. Changes in morphology can drastically affect many properties of a surface, especially in areas such as catalysis [92, 93, 94, 95, 96] and corrosion [97]. One of the most dramatic changes a surface can undergo is adsorbate-induced faceting, the breaking up of a surface into facets of differing orientations under the influence of foreign adsorbates; this chapter investigates the faceting of a high-Miller-index metal surface due to oxygen adsorption. Low symmetry, high index surfaces provide a controlled starting surface (routinely characterized by traditional surface science techniques) with many potential adsorption sites (steps and/or kinks) from which the effects of adsorption can be generalized to more technologically relevant materials (e. g., polycrystalline surfaces [98] or nanoparticles [99, 100]).

While thermal faceting is generally a complex, multistep process [101], adsorbate-induced faceting [102, 103, 104] is further complicated by adsorption kinetics [105, 93] and, if applicable, molecular dissociation [106] or other chemical reactions [107]. Once facet nucleation has begun, surface diffusion [108] can become the dominant process in facet growth and coarsening; significant mass transfer may be involved in the growth of facets which can be hundreds of Å across. While the surface is, ultimately, driven towards a new equilibrium configuration, the kinetics of adsorption or diffusion can severely affect the surface's final morphology, as can variations in the stability of various orientations.

Chapter 3 described the crystallographic structure of facets formed by exposing Cu(115) to O; we now turn to the formation of those facets, which we have observed in real time with surface x-ray diffraction. Three stable facets are formed by O adsorption on Cu(115): O/Cu(104), O/Cu(014), and O/Cu(113)(3×1), with the (104) and (014) facets being crystallographically equivalent. We find that a sufficient O_2 exposure induces spinodal decomposition of the surface, which proceeds with a strong temperature dependence. The temperature dependence of the faceting process reflects changes in the relative stability of various facet orientations, and allows us to propose a Wulff plot for O-covered Cu facets in the vicinity of (115). The time evolution of the faceting process shows a consistent, slow growth mode.

Several metal surfaces have been observed, under the appropriate conditions, to facet upon oxygen adsorption, including many copper surfaces [62, 63, 64, 65, 85, 66, 67, 71, 68, 69, 70]. The case of O/Cu(115) is relatively complex, since two well-defined but inequivalent types of facets result. In contrast are the cases of O-induced faceting of W(100), W(112), and W(111), since, for sufficiently high O coverage, only O/W{110} facets are formed [109]. As another example, only one smooth surface is formed when O was observed to cause faceting of miscut Ag(110): the surface transformed to regions of smooth O/Ag(110) and heavily stepped regions without a well-defined orientation [110].

The structure of many faceting systems have been investigated with a variety of surface probes, including LEED [109, 111, 93], scanning probe microscopies (STM [112, 113, 110] and AFM [114, 115, 116]), low energy electron microscopy (LEEM) [117, 118], helium-beam scattering [119], transmission electron microscopy [112], and, in a few appropriate systems, field ion microscopy [120, 121, 122]. Recently, x-ray scattering methods have been applied to study the thermal faceting of various miscut surfaces, including Cu(110) [123], Ni(111) [124], Pt(001) [125], Pt(111) [126], Au(111) [127], Au(001) [128], and Si(113) [129, 130, 131]. In heteroepitaxial systems, x rays have been used to study the formation of facets on "hut clusters," including the {105} facets of Ge/Si(001) [132] and the {103} facets of In/Ge(001) [133]. In the metal-on-metal systems of Cu/Ni(001) [134] and Co/Pt(110) [135], x-ray diffraction found that fcc crystallites grow with {111} facets.

4.2 Background: Wulff plot and equilibrium crystal shape

Before moving to a description of the experiment, we very briefly discuss the theory of equilibrium crystal shapes, or equivalently, the stability of various surface orientations. The equilibrium shape of a crystal is given by the Wulff construction, i. e., the dependence of surface free energy on orientation [136]. To construct a Wulff plot (also known as the gamma plot), radii from the origin are drawn to every point on a polar plot of surface free energy vs. orientation (actually, radii only need be drawn to all local minima). Planes perpendicular to the radii are drawn at the intersection of the surface free energy plot, with the minimum interior volume representing the equilibrium crystal shape. Mathematically, this is equivalent to a two-dimensional Legendre transformation [101]. Fig. 4.1 provides a two-dimensional example.

A cusp (i. e., a local minimum with a diverging derivative) in the Wulff plot denotes a locally stable facet. By "locally stable," we mean that this orientation has a lower free energy than immediately adjacent orientations; this is the case for orientations A, B, C, and

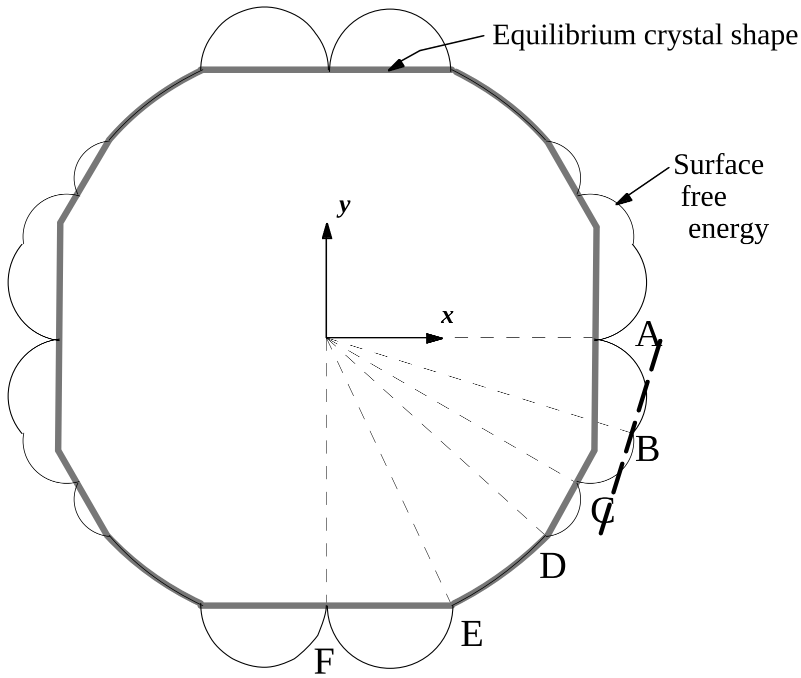

Figure 4.1: Sample Wulff construction, showing the surface free energy vs. orientation (outer, thinner line) and the resulting equilibrium crystal shape (inner, thicker line). Dashed lines are radii from the origin to local minima of the surface free energy. The effects at orientations A through F are discussed in the text.

F in Fig. 4.1. However, another nearby orientation may have such a deeper cusp that a facet of the latter orientation is preferred to the former. In the example of Fig. 4.1, the cusps at orientations A and C overwhelm the cusp at B, so orientation B is only a metastable orientation which will not be found on the equilibrium crystal. Surface roughening may occur for a range of orientations which have approximately equal (and locally minimal) free energies [101]; this is the case for orientations D to E in Fig. 4.1. No orientations in this range are energetically preferred, and the surface is, statistically, rough [101]. Adsorbates and reconstructions may alter the anisotropy of the surface free energy enough to affect the equilibrium crystal shape [137, 138], perhaps changing relative facet areas or driving some orientations unstable. If adsorption leads to a deep cusp at a given orientation, then a nearby, less stable surface may facet to the more stable orientation if the decrease in surface energy offsets the increase in surface area.

It has long been known [139] that the equilibrium shape of a crystal can be discussed in the language of phase transitions of binary alloys. That is, orientations which appear on the Wulff plot are stable phases; the edges which separate facets are phase boundaries, which can be classified as first order transitions (in the case of sharp edges) or second order transitions (for rounded edges) [101]. Orientations which do not appear on the Wulff plot (e. g., orientation B in Fig. 4.1) are unstable phases; the faceting of such a surface into stable orientations is thermodynamically favorable [140] and is a case of spinodal decomposition [141, 139, 101, 142]. Several theoretical studies have focused on the stability of various orientations at zero and finite temperatures [143, 104, 144, 84, 145]. Other theoretical work has focused on the late-time evolution of the typical facet length scale $L(t)$, often finding power-law behavior

$$L(t) \sim t^{\phi} \tag{4.1}$$

or logarithmic behavior

$$L(t) \sim \ln(t). \tag{4.2}$$

The choice between these forms (and also the value of the exponent ϕ) may depend sensitively on the dimension of the system and the mode of mass transfer. Early on, Mullins [146, 147] derived power-law behavior with $\phi = \frac{1}{2}$, $\frac{1}{3}$, or $\frac{1}{4}$ for mass transport in two dimensions by evaporation/condensation, volume diffusion, and surface diffusion respectively. However, these values are much higher than have typically been observed in experiments [129, 116] and some simulations [148, 149, 150]. Attempting to explain the slower than expected coarsening rates, Papoular [108] proposed $\phi = \frac{1}{6}$ when kink-antikink reorganization time is the limiting factor in mass transport, while Song *et al.* [130] argued that $\phi = \frac{1}{6}$ when growth proceeds by thermal collisions of step bunches. By working in the continuum limit, Stewart and Goldenfeld [142] found that non-negligible surface stress could destroy any dynamic scaling, while Liu and Metiu [149] derived logarithmic scaling in the case of quasi-one-dimensional surface diffusion. On the other hand, Shore and Buchman [151] argued that coarse-grained models neglect dynamics on the scale of individual steps, which are too important to ignore on vicinal surfaces. Barriers then depend on (grow with) the length scale, which again results in logarithmic scaling [151]. Jeong and Weeks [152] also studied step-step interactions on vicinal surfaces, finding that flat reconstructed terraces grow very fast, in fact linearly with time, along the step direction, but with $\phi = \frac{1}{2}$ or $\frac{1}{4}$ perpendicular to the steps (for global or local mass transport, respectively). Furthermore, they found the kinetic effects of local mass transport were sufficient for a growing facet to nucleate new facets nearby [152]. Vlachos *et al.* [150] used Monte Carlo simulations to study faceting under equilibrium conditions, finding that the exponent ϕ could vary with temperature, orientation, and material [150].

4.3 Experimental method

This series of experiments was performed *in situ* at beamline X16A of the National Synchrotron Light Source, Brookhaven National Lab, on the five-circle UHV diffractometer [15]. The starting surface, clean Cu(115), was prepared fresh for each O-dosing experiment by sputtering with 1 keV Ar^+ ions followed by annealing to 550° C. The sample temperature was then slowly lowered to a desired point (200° C to 400° C), and Cu(115) CTRs were measured to verify that the surface was clean, ordered, and free of other facets. O_2 was then admitted into the chamber through a leak valve at a constant partial pressure (P_{O_2}= 2×10^{-9} Torr to 1.5×10^{-7} Torr).

To observe the faceting process with diffraction, we continuously performed scans while dosing progressed. We scanned near the $(603)_{115}$ bulk Bragg peak, but close to the surface plane ($\ell = 0.6$) to enhance surface sensitivity. (The relation between standard fcc units and 115 surface units is given by Eq. 3.1.) As discussed in Section 3.1, any well-defined facet on the surface will have a CTR associated with it. By locating the intersection of a CTR and the $\ell = 0.6$ plane, its facet orientation could be precisely determined, since these CTRs intersect the $(603)_{115}$ Bragg point. The primary scans we performed were along $[h, 0, 0.6]$, to scan continuously from the (115) to (113) orientations. This scan effectively searches for all ($11n$)-oriented facets from $n \sim 6$ to $n \sim 2.5$. In several experiments, we also scanned radially and transversely through the (104) facet CTR. Our results, based on many various dosing experiments at various temperatures and O_2 partial pressures, are described in the next section.

4.4 Faceting observed by x-ray diffraction

4.4.1 Early stages of facet formation

Evolution of the Cu(115) surface morphology during the early stage of O adsorption was qualitatively similar for the entire range of temperatures and O_2 partial pressures under consideration, and is described first. (Later effects, which vary strongly with substrate temperature, are described in subsections 4.4.2 through 4.4.4.) No immediate changes were observed in the (115) CTR as O dosing began, but slowly, the intensity of the CTR decreased without observable broadening or shifting of the peak; no facets other than (115) were observed in this time. This behavior is consistent with a random disordering of the steps on this vicinal surface [153, 150], similar to that observed for O on Cu($hk0$) vicinal surfaces [154]. Indeed, calculations by Jeong and Weeks [155] predicted that step fluctuations should increase (and step stiffness decrease, relative to an isolated step) for such a vicinal surface undergoing spinodal decomposition.

Quite suddenly, however, the O-decorated Cu(115) surface destabilized and nanoscopic facets began to form. Two changes, occurring simultaneously, marked this transformation: the abrupt appearance of the O/Cu(104) and O/Cu(014) CTRs, and the slow shift of the (115) CTR towards the (113) orientation. We index the intermediate facet as ($11n$), with

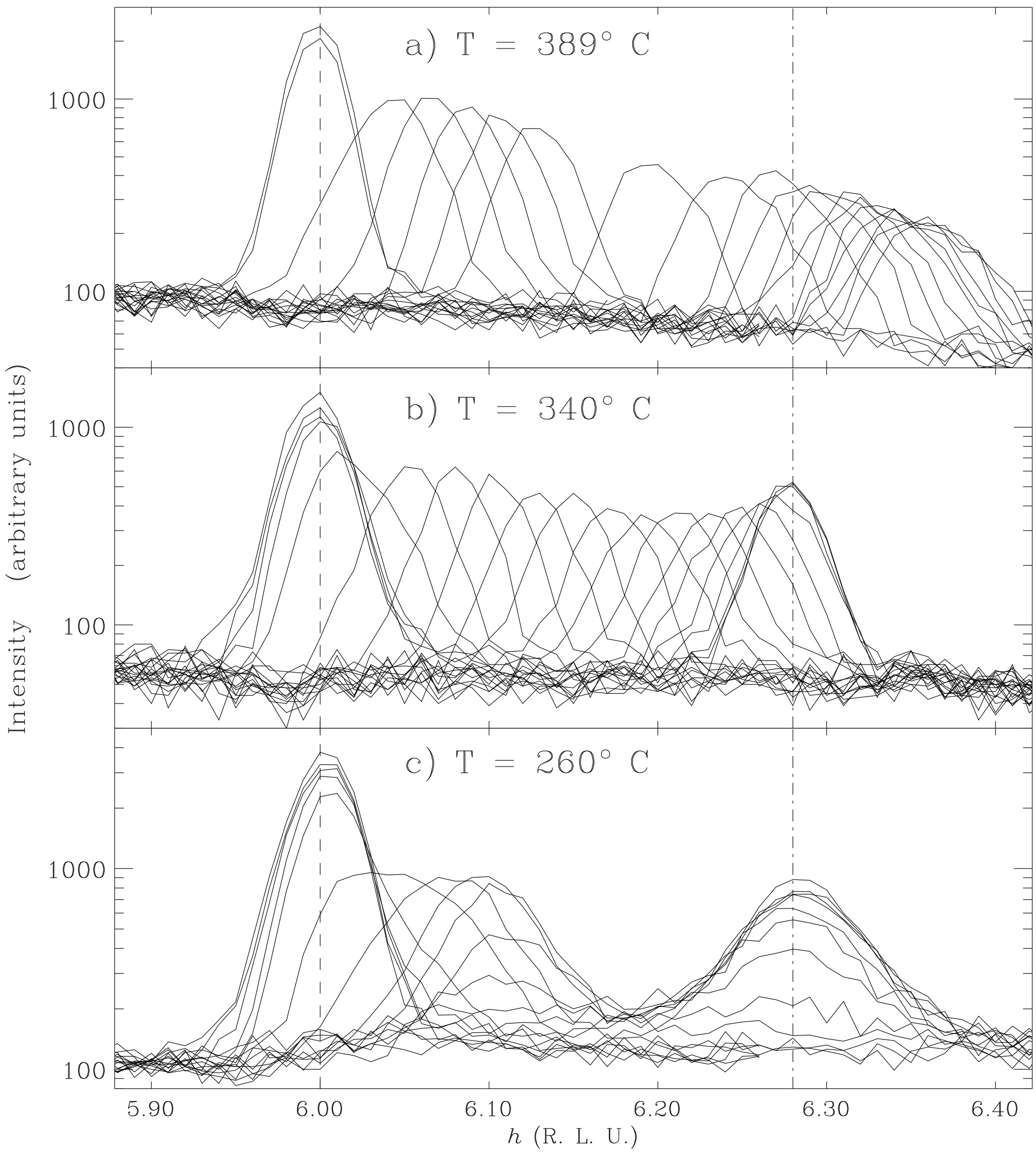

Figure 4.2: Selected scans through $(11n)$ facet CTRs during faceting, for three representative temperatures. These scans are performed below the $(603)_{115}$ bulk peak, at $k = 0$, $\ell = 0.6$ in units of the 115 surface unit cell (similar to the dotted line in Fig. 3.2). The vertical dashed line indicates the (115) peak position ($h = 6.0$), while the dot-dashed line marks the (113) peak position ($h = 6.28$). Scanning proceeded from left to right, the same direction as peak motion, resulting in a slight broadening of the peaks.
a) $T = 389°$ C; faceting does not cease at the (113) orientation.
b) $T = 340°$ C; faceting proceeds smoothly from (115) to (113).
c) $T = 260°$ C; faceting occurs discontinuously from (115) to (113).

n representing the continuum of well-defined but nonsingular orientations between (115) and (113), since it has a well-defined orientation but no special direction. The tilting of the (11n) CTR resulted from a shift in facet orientation away from (115) toward a more densely-stepped surface. This gradual tilting is shown for three dosing experiments in Fig. 4.2. The [h, 0, 0.6] scans shown in Fig. 4.2 are a direct measure of facet orientation, since all of the rods pass through the $(603)_{115}$ bulk peak. The strong temperature dependence of the facet evolution is discussed below.

By repeating the O dosing experiments at many temperatures and pressures, we found a wide range in the time delay between initiation of O_2 dosing and the commencing of faceting, as shown in Fig. 4.3a. Instead, we found that the *amount* of exposed O_2 (i. e., dose), rather than exposure time, was the critical factor to initiate faceting. For the entire range of pressures and temperatures studied in these experiments, faceting began after an exposure of 9.6 ± 1.4 L of oxygen, as shown in Fig. 4.3b. For the purposes of Fig. 4.3, the "starting dose" is defined as the dose at which the (115) CTR moved by its halfwidth from $h = 6.0$ towards higher h (medium and high temperatures), or else developed a clear shoulder on the high-h side (lower temperatures). An alternate definition, namely the exact dose at which the (104) facet CTR first appeared, is more difficult to employ; the change in position (or lineshape) of an existing peak was easier to observe than the appearance of a new peak out of the diffuse background. However, we find the two definitions to be equivalent to within ± 1 L when we project the early-time (104) CTR intensities, shown in Fig. 4.7, back to zero elapsed dose (i. e., dose with the "starting dose" subtracted off).

In our measurements, the starting dose could be most accurately determined when changes in surface morphology were the slowest, i. e., at lower O_2 partial pressures. This accounts for the larger error bars for the higher pressures in Fig. 4.3b; in fact, experiments at even higher partial pressures are excluded from Fig. 4.3 because in these cases faceting occurred too quickly to accurately determine the starting dose. Since the temporal evolution

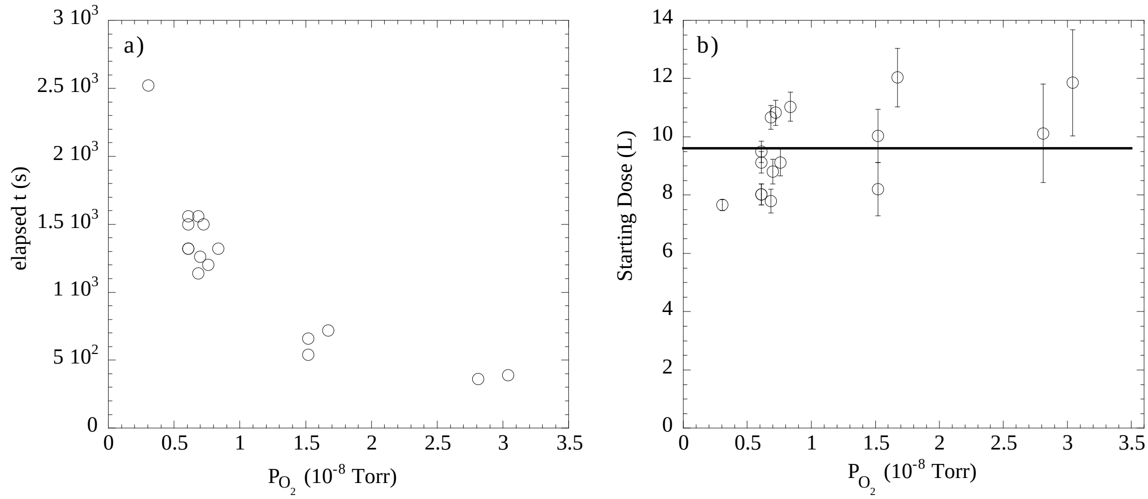

Figure 4.3: Plots of a) elapsed time and b) O_2 dose at which faceting began, which turns out to be a dose of 9.6 L. "Starting dose" is defined as the dose of O_2 at which the (115) facet peak began to move towards (113).

of the faceting surface depended on cumulative O_2 exposure (rather than exposure time) in the following sections we will plot any changes to the facets against O_2 dose as a way to normalize experiments performed at different O_2 partial pressures. Faceting was typically completed after a total dose of 30 to 40 L independent of temperature or pressure (except for the highest temperatures, as described below), but the time scales could range from minutes to hours depending on P_{O_2}.

The observation that faceting begins after a 9.6-L dose is consistent with STM micrographs taken by Taglauer *et al.* [156] at 210° C as a function of dose: After an O_2 exposure of 10 L, the Cu(115) surface was somewhat disordered and a moderate fraction of the surface area was faceted. The surface was completely transformed to (104), (014), and (113) facets after a 30-L exposure, although facet sizes continued evolving after higher doses [156].

The observed behavior of the (104) and (014) facets differed significantly from that of the (11n) facets. The CTRs associated with the (104) facets were always found at the exact (104) orientation, never shifting position. These (104) peaks did gain intensity, reflecting the growth of these facets across the surface until the (11n) facet ceased evolving; this behavior of the (104) facets was found for all temperatures studied. The (113) facets, as mentioned above, did not form abruptly; furthermore, their evolution is strongly temperature dependent. Each temperature regime is discussed separately in the following sections.

4.4.2 Medium-temperature facet formation

We first discuss (113) facet growth in the medium temperature regime (310° C $\lesssim T \lesssim$ 370° C), since the phenomenon was most straightforward here. Just as the {104} facet peak appeared, the (115) peak shifted in the $+h$ direction away from its original position of $h = 6$, as seen in Fig. 4.2b. No shift was ever observed in k. This change in peak position corresponded to a change in the orientation of the $(11n)$ facet, with n changing smoothly from 5 to 3 in this temperature regime. To better visualize the evolution of the $(11n)$ facets, the facet positions from Fig. 4.2 are plotted against O_2 exposure in Fig. 4.4. Since peak position in h for a given ℓ (the left axes of Fig. 4.4) is a direct measure of facet orientation, angular deviation of the facet from (115) is shown on the right axes. The symbol size in this figure is indicative of the height of the peak from Fig. 4.2.

In this middle temperature regime, the $(11n)$ facet peak was moderately broader than the initial (115) peak but remained sharp, reflecting a well-defined yet continuously changing orientation as the (104) and (014) facets grew. The widths of the $(11n)$ peaks are given by a combination of the facet size, the small but nonzero distribution of facet orientations, and instrumental resolution (including the effect of scans being performed along the direction of peak motion, see Fig. 4.2). The shifting of the $(11n)$ orientation was due to a gradual bunching of steps on the $(11n)$ facets, with the average step separation changing from 6.64 Å [for Cu(115)] to 4.24 Å [for Cu(113)]. This mode of step formation may help explain the structural disorder found on the O/Cu(113)(3×1) facets (see Sec. 3.4 and Ref. [69]).

Once faceting concluded and the (113) peak had formed, we found that the size of the facets (inversely proportional to the CTR widths) tended to be greater at higher tempera-

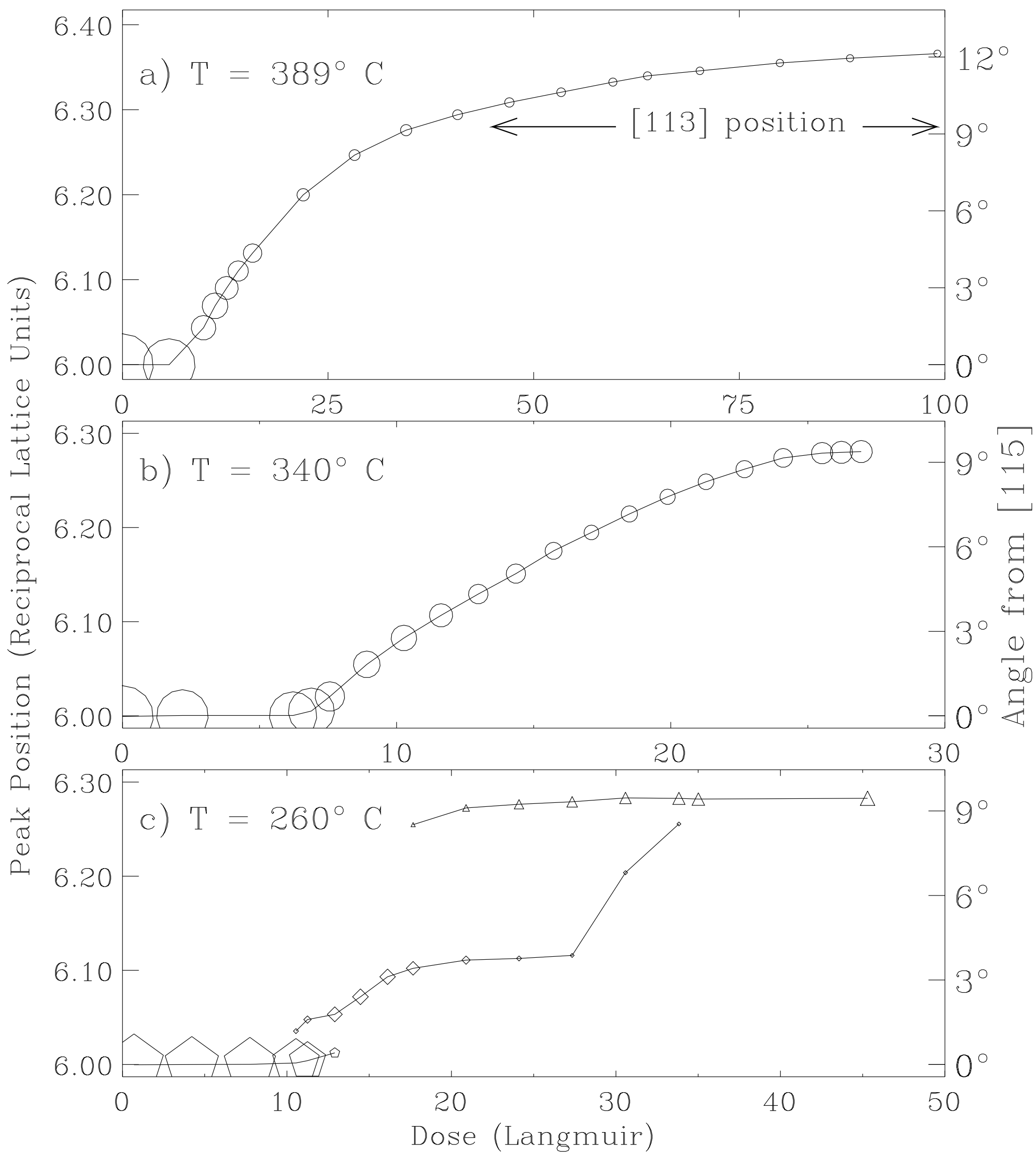

Figure 4.4: Positions of $(11n)$ facets shown in Fig. 4.2 during dosing. The radius of the symbol is proportional to the height of the facet peak. The left axis gives peak position in 115 reciprocal lattice units, and the right gives the angle of the facet from (115) [which is 9.45° for (113)].
For a) and b) (T = 389° C and 340° C respectively), circles represent the position of the one $(11n)$ facet as it changes smoothly from (115) to (113) (and beyond, for T = 389° C). For c) (T = 260° C), pentagons refer to the (115) peak position, diamonds to the $(11n)$ facet, and triangles to the (113) peak.

tures (as long as $T < 370°$ C). This is seen in the significantly broader (113) peak at $T = 260°$ C (Fig. 4.2c) compared to the (113) peak at $T = 340°$ C (Fig. 4.2b), even though the initial (115) peaks at the two temperatures were about equally wide.

4.4.3 High-temperature facet formation

As is the case for medium temperatures, the faceting process at high temperatures ($T \gtrsim 370°$ C) began with the simultaneous appearance of (104) facet CTRs and movement of the (115) CTR towards (113). The change in orientation through the ($11n$) facets was smooth, as before (the scans in Fig. 4.2a are not equally spaced in time); the difference is that the facet continued well past the (113) position! Even after a dose of 100 L, the orientation of the facet continued to tilt away from (115), although the rate of peak motion had slowed considerably. In terms of the Wulff plot, this behavior demonstrates the removal of the cusp at (113), as discussed in detail below.

4.4.4 Low-temperature facet formation

The formation of (113) facets at low temperatures ($T \lesssim 310°$ C) differed significantly from the previous cases. After a dose of 10 L, the {104} facets formed suddenly, as above, but the ($11n$) facet did not slowly and smoothly shift in orientation, as seen in Fig. 4.2c. Instead, a shoulder appeared on the high-h side of the (115) peak, which grew and shifted as the (115) peak disappeared. The shoulder became the ($11n$) peak but did not proceed continuously to $n = 3$. It moved less than halfway to the (113) position and then dropped in intensity while the (113) peak abruptly appeared. In sharp contrast to the results at higher temperatures, no well-defined peak was observed for the range of orientations around $h = 6.2$ (due to an increase in the surface free energy of these orientations). Two peaks were present for part of the dosing time; thus, the faceting surface at lower temperatures consisted of two coexisting domains of (113) and ($11n$) orientation, with the (113) facets growing at the expense of the

(11n) facets.

The (113) CTR did not change orientation once the (11n) facet had disappeared, but a moderate increase in intensity and narrowing of width was typically observed. This effect, more pronounced in the low temperature regime, reflects the slow ordering which took place on this moderately disordered (Sec. 3.4) surface. The ordering was slowest and least complete at lowest temperatures, where surface diffusion was slowest. No corresponding effect was observed for the (104) CTRs, which did not seem to change in intensity or width once the (11n) facet peak disappeared.

4.4.5 Reversal of faceting

Once the (113) facets had formed and surface evolution had ceased, we observed that the faceted surface was stable even when oxygen gas was removed from the chamber. Facets decomposed only upon annealing at 500° C, at which point O desorption from the fully faceted surface became significant. We also performed a few experiments wherein the O supply was cut off after faceting had begun, but well before (113) facets had formed. Specifically, during a dose at T = 263° C and $P_{O_2} = 8 \times 10^{-9}$ Torr, the O_2 supply was cut off when the (11n) peak had reached $h = 6.08$ (as in Fig. 4.2); faceting did not continue or even cease, but immediately *reversed*, reverting to the (115) orientation without the development of any other facets. This (115) surface was moderately well-ordered, as judged by CTR intensities and widths, but was not as good as a freshly prepared (115) surface. In another case, O-dosing in the high-temperature regime (T = 389° C, $P_{O_2} = 1.5 \times 10^{-8}$ Torr) was cut off with the (11n) peak at $h = 6.36$ (just after the last scan in Fig. 4.2a); reversal of orientation was again immediate, and we note that this surface showed no tendency to stabilize at the (113) facet, but continued back towards (115). The immediate reversal of facet formation is directly attributable to oxygen desorption. But as a surface with crystallographically inequivalent facets is not well-suited for a quantified study of desorption kinetics, this series of experiments was not pursued further.

4.5 Stability and evolution of facets

4.5.1 Equilibrium surface free energies of facets

The real-time experiments described in Sec. 4.4 dramatically demonstrate the sensitivity of the O/Cu(115) faceting process to temperature, but its relative insensitivity to O_2 partial pressure. From these results we are able to qualitatively describe the relative stabilities of a number of orientations near the O/Cu(115) pole, and quantitatively determine the long-time evolution of the faceting surface. Such results are possible because the surface structure remains, locally, in equilibrium as the surface undergoes spinodal decomposition from (115) to (104), (014), and ($11n$) facets. While the oxygen in vapor form is not in equilibrium with the oxygen adsorbed on the surface, we argue that the surface morphology is always in equilibrium for a given oxygen coverage.

Several observations show that adsorbate-induced faceting in this system is not merely a kinetic effect. First of all, Sec. 4.4.1 demonstrates that, for all temperatures and pressures investigated, faceting begins after a nonzero O_2 dose, i. e., after a certain amount of oxygen had adsorbed onto Cu(115). A kinetically activated process would likely be observed to begin immediately, or exhibit a temperature-dependent time (not dose) delay. Second, continued oxygen adsorption was essential for faceting to continue. As described in Sec. 4.4.5, the removal of O_2 from the vacuum chamber immediately caused the facets to decompose; a kinetic effect might cause facet evolution to stall without O_2 but would not reverse the process. We also note that the role of oxygen is not primarily that of a surfactant, i. e., to increase the mobility of Cu adatoms; previous experiments [157, 158] have demonstrated the high mobility of Cu on low-symmetry Cu surfaces without oxygen present, at substantially lower temperatures. The oxygen, then, changes the surface free energies of various facet orientations, forcing the surface to undergo spinodal decomposition as O coverage increases.

The primary effect of O on the Cu(115) surface, then, is to lower the surface free energy of the (104) facet, which results in an increase in the anisotropy of the Wulff plot. As discussed in Sec. 4.2, faceting can become energetically favorable for a sufficiently anisotropic Wulff plot, despite the accompanying increase in surface area. In the present series of experiments, O/Cu(104) facets were observed for all faceting temperatures and O_2 partial pressures; these facets formed abruptly and were never misoriented. Therefore, we conclude that formation of O/Cu(104) facets drives the faceting of the Cu(115) surface, consistent with previous studies on Cu(115) and other Cu(001) vicinal surfaces. The stability of this facet has been attributed to its structural similarity to a regularly stepped version of the O/Cu(001)$(2\sqrt{2}\times\sqrt{2})$ surface [89]; this concept may be tested rigorously now that the O/Cu(104) structure is known (Section 3.3).

Once the O/Cu(104) facets begin to form and grow, the $(11n)$ facets must evolve in order to maintain a macroscopic (115) orientation. Therefore, O/Cu(115) facets cannot remain on the surface, but it does not necessarily follow that these facets become unstable. Boulliard *et al.* [67] observed a weak LEED pattern from (115) facets after O-induced faceting of Cu(117) at high coverages and low temperatures (200° C). O/Cu(115) could thus be locally stable but, like orientation B in Fig. 4.1, be overwhelmed by nearby orientations with much lower surface free energies.

The evolution of the $(11n)$ facet orientation is thus driven by the growth of the (104) facets (essentially via step bunching). That is, as the (104) facets grow, the $(11n)$ facets must tilt farther and farther from (115) in order to maintain an overall (115) orientation for the macroscopic surface. This tilting involves a significant amount of mass transport of the Cu atoms at and near the surface, which in this UHV experiment occurs by surface diffusion (rather than bulk diffusion or evaporation-condensation). The details of this evolution, however, are sensitive to the surface free energies of the O-covered $(11n)$ facets. Fig. 4.4

displays the contrasting behaviors of $(11n)$ facet evolution in the three temperature regimes; the presence or absence of peaks at a given orientation is an indication of the relative surface free energy of that orientation. For example, the orientation which corresponds to $h = 6.15$ is stable at 340° C (Fig. 4.4b) but not at 260° C (Fig. 4.4c), since essentially no peak is present at that orientation for the lower temperatures. As another example, (113) has a lower surface free energy than its neighboring orientations at 340° C (Fig. 4.4b), since the $(11n)$ facet becomes locked in to that orientation and does not evolve farther; this is caused by the (3×1) reconstruction lowering the surface energy of that specific orientation. But at 389° C (Fig. 4.4a), evolution continues beyond (113), indicating that the free energy of this surface orientation is not substantially different from its neighbors at this high temperature [presumably due to the removal of the (3×1) reconstruction].

To concisely present the variations in surface free energy with orientation and temperature, we propose three Wulff plots around the (115) pole for the O on Cu system, one for each observed temperature regime. The proposed plots are shown in Fig. 4.5a-c; these are actually "beta plots" instead of "gamma plots," i. e., a rectilinear instead of polar plot of surface free energy vs. orientation. The orientational map is shown in Fig. 4.5d: ζ is the angle between (115) and (113) (the right half of Fig. 4.5a-c), and ξ is the angle between (115) and (104) (the left half). Orientations which do not fall along ζ or ξ were never observed, and presumably have much higher surface free energies.

The deep cusps in the Wulff plots on the left side of Fig. 4.5 indicate, for all temperatures, the significantly lower surface free energy of O/Cu(104) relative to any other orientation along ξ. The depths of these cusps decrease with increasing temperature, matching the trend of increased anisotropy in the Wulff plot at lower temperatures [138]. Cusps, not merely local minima, are plotted because the O/Cu(104) facet derives its stability from its regular step spacing; nearby orientations lack this stability, and were never observed here with x-ray diffraction or elsewhere by STM [69]. Other orientations along ζ are assigned to much higher

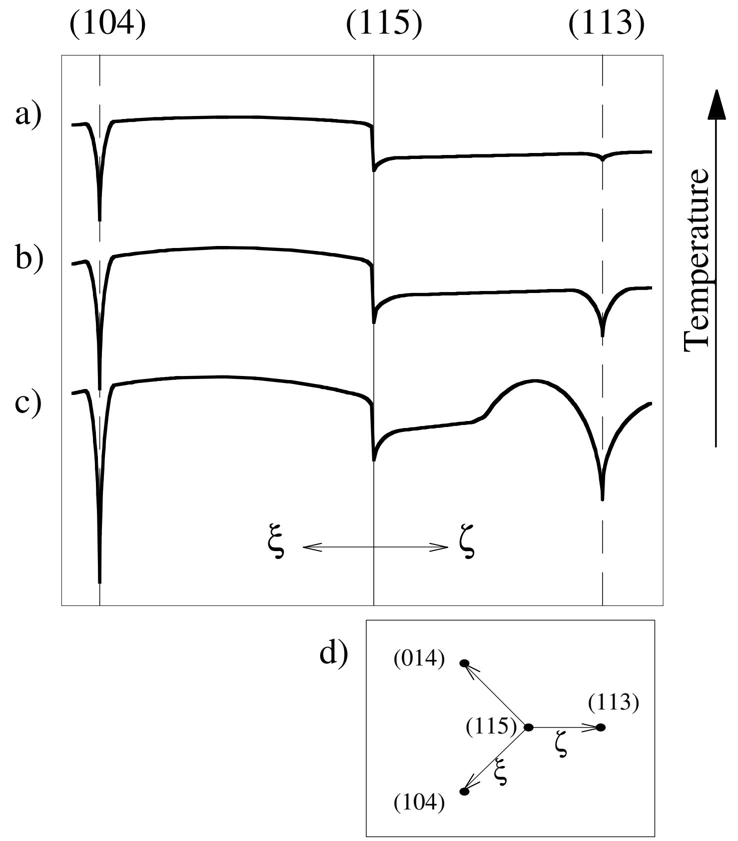

Figure 4.5: Proposed Wulff plots for the O on Cu system around the (115) orientation. a) $T \gtrsim 370°$ C; b) $310°$ C $\lesssim T \lesssim 370°$ C; c) $T \lesssim 310°$ C. Details are discussed in the text. d) Orientational map around the (115) pole.

surface free energies, since the irregularly spaced, <010>-type steps of these facets are not expected to lead to stable orientations. The small minima at (115) indicate the slightly lower surface free energy of this orientation relative to its neighbors, as inferred from its appearance in the LEED patterns of Boulliard *et al.* [67] The more interesting temperature dependence is along ζ, on the right side of Fig. 4.5. In the high temperature regime (Fig. 4.5a), the surface free energy varies little with orientation. The same is true of the medium temperature regime (Fig. 4.5b), except for the cusp at (113); for these temperatures, the (3×1) reconstruction lowers the surface free energy at this particular orientation. The bump at lower temperatures (Fig. 4.5c) represents the higher surface free energies of the orientations close to (113) but not observed. The near or total disappearance of the (113) cusp at high temperature and the bump along ξ at lower temperatures are again consistent with the trend of increased anisotropy in the Wulff plot as temperatures are decreased. We do, however, emphasize the information presented in Fig. 4.5 is necessarily qualitative. The presence or absence of cusps (or other general features) can be linked to the presence or absence of orientations as observed by this and other experiments. However, the relative values of the surface free energies in Fig. 4.5, while consistent with experimental results, are estimations; surface x-ray diffraction is not a direct measure of the Wulff plot. Furthermore, the surface free energies of some orientations may vary with O coverage, which is beyond the scope of Fig. 4.5. Diffraction can be used, however, to measure the state of the faceting surface, which we present in the following section.

4.5.2 Dynamic scaling of facet growth

Beyond the schematic description of the orientational dependence of surface free energies, the measurement of facet orientation vs. O_2 exposure can explore the dynamic scaling of the facets as they undergo spinodal decomposition. Two order parameters can be used to describe the state of the faceting surface and present complementary information on the complex process of facet growth: I_{104}, the intensity of the (104) CTR at a given point, can be related to the surface area covered by (104) facets, and ζ, the $(11n)$ facet orientation relative to (115), can be related to the relative sizes of the (104) and $(11n)$ facets, as described below.

We begin our analysis of dynamic scaling with the evolution of the $(11n)$ facets in the middle- and high-temperature regimes. Indeed, it is not *a priori* clear whether this system should exhibit any form of scaling at all, since the evolution of the $(11n)$ peak will be sensitive to the energy landscape along ζ (see Fig. 4.5). Specifically, the anisotropy of the Wulff plot at low temperatures ($T \lesssim 310°$ C) will destroy any scaling of the $(11n)$ facet evolution. Experiments in the middle temperature range may exhibit scaling over a limited period of time, but such behavior will be abruptly truncated when the facet orientation reaches $(11n)$.

Nevertheless, we can evaluate the relative area of the (104) facets based on the $(11n)$ facet orientation simply by employing two conservation laws [159]. The first is conservation of projected surface area. If S_i is the surface area of facet i projected onto the (115) plane (i. e., the plane of the unfaceted surface), then

$$S_{115} = S_{104} + S_{014} + S_{11n}. \tag{4.3}$$

The second law is conservation of macroscopic orientation. If $\hat{e}_i$ is the unit vector normal to facet i, then the average orientation during and after faceting must remain the same as that before faceting began:

$$S_{115}\hat{e}_{115} = S_{104}\hat{e}_{104} + S_{014}\hat{e}_{014} + S_{11n}\hat{e}_{11n}. \tag{4.4}$$

Comparing the (104) and (014) facets, we can take

$$S_{104} = S_{014} \tag{4.5}$$

since these facets are symmetry equivalents and uniformly tilted with respect to (115); small deviations from eq. 4.5 could occur for a surface significantly miscut from (115) but are negligible here.

Equations 4.3 through 4.5 can be used to solve for S_{104}/S_{115}, i. e., the surface area of the (104) facets (projected onto the initial surface) relative to the starting (115) area, in terms of the $(11n)$ facet orientation:

$$\frac{S_{104}}{S_{115}} = \frac{\sqrt{\sqrt{27}\sqrt{2+n^2} - 2 - 5n}}{\sqrt{67\sqrt{2+n^2}/\sqrt{17} - 4(1+4n)}}. \tag{4.6}$$

n can be written as a function of ζ, the angle of $(11n)$ from (115):

$$n = \frac{10 - 27\sqrt{2}\,\sin(\zeta)\cos(\zeta)}{27\cos^2(\zeta) - 25}. \tag{4.7}$$

And finally, ζ can be expressed in terms of h, the position (in reciprocal lattice units) of the $(11n)$ peak at a given ℓ ($= 0.6$) in Fig. 4.2:

$$\tan\zeta = \frac{a^*(\Delta h)}{c^*\Delta\ell} = \frac{\sqrt{2}\,(h-6)}{2.4}, \tag{4.8}$$

where Δh and $\Delta \ell$ are the displacements from the bulk Bragg point, which in this case is (603) [in the (115) reference system]. Reciprocal lattice parameters a^* and c^* are also in (115) units.

While eq. 4.6 gives the projected area of the (104) facets in terms of $(11n)$ orientation, two conditions must be met in order to turn S_{104}/S_{115} into a useful scaling parameter: first, the entire surface must be faceting at about the same rate; second, the area covered by the faceting pyramids must remain constant during a dosing experiment. The first condition requires that only well-defined (104), (014), and $(11n)$ facets be found on the surface while faceting occurs, with no (115) remaining. This has been experimentally verified for the middle- and high-temperature faceting regimes, as described in Sections 4.4.2 and 4.4.3; it is not met in the low-temperature regime (Sec. 4.4.4) since the distribution of $(11n)$ orientations becomes bimodal about halfway through the faceting process. The second condition is needed to ensure that S_{104}/S_{115} is a measure of the growing size of the (104) facets, instead of the growth in number of (104) facets. Although some small amount of ripening probably occurs, we observed the (104) facet peak to always cease evolving when the $(11n)$ facet reached (113). This proves that the (104) facets grow in size mainly at the expense of the $(11n)$ orientation, not at the expense of other (104) or (014) facets.

The results of scaling based on $(11n)$ orientation are shown in Fig. 4.6. The normalized area S_{104}/S_{115} is plotted against elapsed dose (i. e., O_2 exposure beyond the "starting dose" as defined in Sec. 4.4.1) for four dosing experiments at medium and high temperatures. These experiments were performed at different but relatively low oxygen partial pressures, since slower changes in morphology could be traced with higher resolution. In addition, we have plotted the best fits of logarithmic and power-law scaling over the later stages of faceting. Dose = 0 was included as a fitting parameter, since it could not be precisely measured. We find that both scaling forms produce very good fits to the available data, with very nearly equal R factors such that we cannot prefer one form to the other. Furthermore, for the power-law fits, there is a rather large range in the fit to the exponent ϕ, from 0.11 to 0.25. The limited information that can be derived from these fits is directly due to the relatively short time spans over which faceting occurs: except for the high temperature experiment (Fig. 4.6d), faceting is abruptly truncated when the (113) facet is reached, necessarily limiting the fittable range. Interestingly, the fitted exponent ϕ is lowest for the one high-temperature experiment where dosing continues for the longest time, but logarithmic scaling still provides an acceptable fit too.

Although the scaling in Fig. 4.6 was performed with respect to calculated area of the (104) facets, these results essentially represent the growth of the facets in linear size. That is, $S_{104} \propto L_x L_y$ where L_x and L_y are the length and width of the (104) facets (with the directions x and y as defined in Sec. 3.3), but Fig. 4.6 mainly reflects evolution of L_x. This is because the (104) facet growth is extremely anisotropic: a given facet grows very quickly along its <010>-type rows (parallel to the O–Cu–O rows), but much slower across the rows. While the widths of the (104) CTRs were quite broad in x (the direction perpendicular to the <010> steps), the widths in y were much narrower (indicative of longer-ranged order) and were not observed to change while faceting occurred. Therefore, the evolution of L_y finished rapidly, and the facets grew in area mainly by the increase in L_x. Such growth rate anisotropies have been previously observed experimentally [131] and theoretically [152].

As a separate measure of the size of the (104) facets, we have investigated the evolution of I_{104}, the scattered intensity at a point on the (104) CTR. Specifically, in Fig. 4.7 we plot the peak intensity (above background) at the point $(5.8285, -0.0572, 0.6)_{115} = (5, 1, 1.06)_{104}$ against elapsed dose. (See Fig. 3.6d to locate this point on the CTR.) For the four experiments in the low- and middle-temperature regimes, the intensity is fit about equally well by either logarithmic or power-law scaling. Again, this scaling only holds up to the point at which the (113) orientation is reached and faceting ceases, whereupon I_{104} saturates. We note that the evolution of I_{104} with dose is smooth (if relatively noisy) and gives no sign of

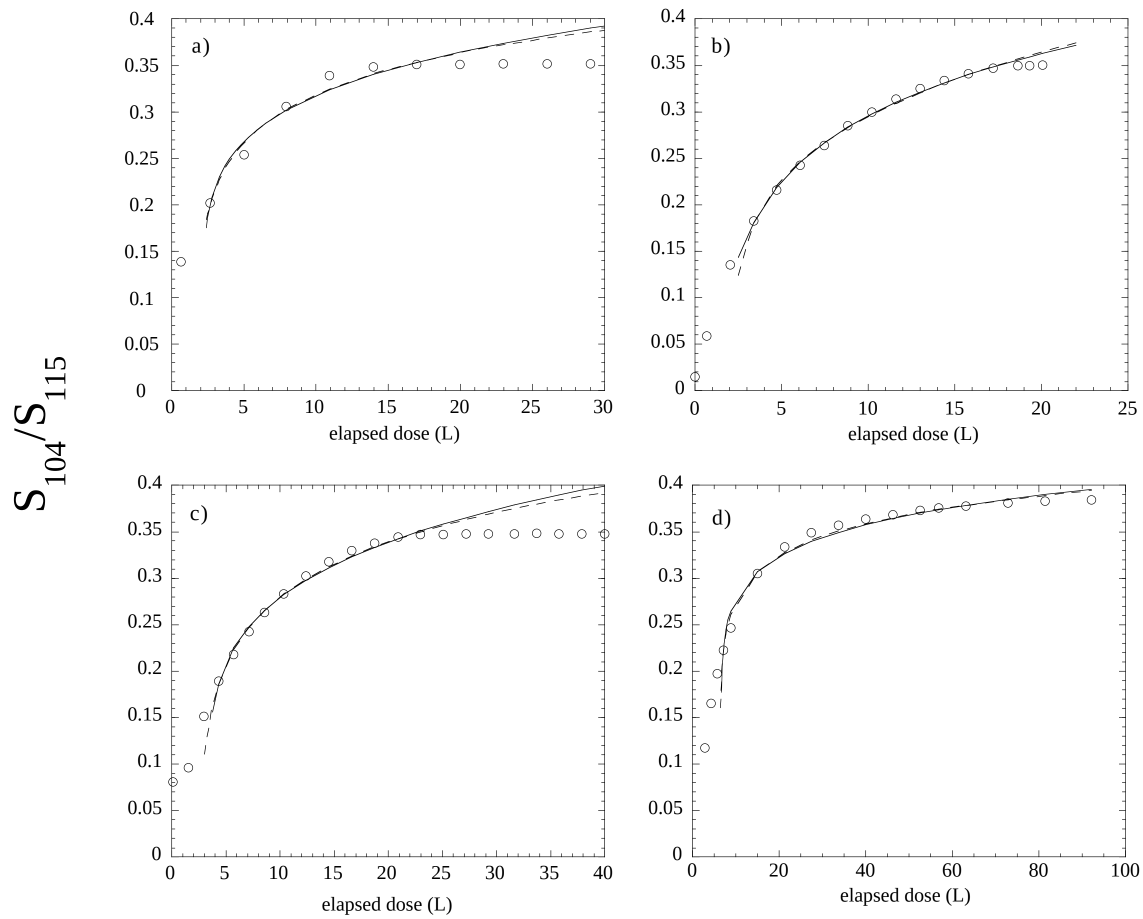

Figure 4.6: Projected area of (104) facets vs. O_2 exposure, for several dosing experiments in the middle- and high-temperature regimes. Circles are measured areas, derived from eqs. 4.3 to 4.8; solid and dashed lines are best fits to logarithmic and power-law scaling, respectively, both of which fit about equally well.
a) Dosing with experimental conditions of $T = 336°$ C and $P_{O_2} = 2 \times 10^{-8}$ Torr. The resulting power-law fit yields $\phi = 0.17 \pm 0.04$.
b) $T = 340°$ C, $P_{O_2} = 3 \times 10^{-9}$ Torr; $\phi = 0.26 \pm 0.02$.
c) $T = 355°$ C, $P_{O_2} = 1.5 \times 10^{-8}$ Torr; $\phi = 0.21 \pm 0.02$.
d) $T = 389°$ C, $P_{O_2} = 1.5 \times 10^{-8}$ Torr; $\phi = 0.11 \pm 0.01$.

the discontinuous evolution of the $(11n)$ orientation at low temperatures (in, e. g., Fig. 4.4c). Although the mix of $(11n)$ and (113) orientations prohibits reliable calculation of S_{104}/S_{115} in the low-temperature regime, we can use I_{104} to study dynamical scaling in this regime.

I_{104} can be related to the number of (104) facets on the surface, N_f, and to the average length and width of the facets (L_x and L_y respectively) by

$$I_{104} \propto |F_{104}|^2 N_f (L_x L_y)^2 \tag{4.9}$$

and will be a useful scaling parameter if certain conditions are met. First, eq. 4.9 assumes coherent scattering across a facet (i. e., the amplitude is proportional to the size of the facet), but incoherent faceting between facets (i. e., the intensity is proportional to the number of facets). This assumption is verified from our investigation of the O/Cu(104) surface structure (Sec. 3.3), where we found the roughness parameter $\beta = 0$. β is essentially a measure of the height variation of a rough surface, since atoms at different heights will scatter with destructive interference (albeit coherently) [9]. Because a given (104) facet can be atomically smooth (see the micrographs of Reiter and Taglauer [69]), but the faceted surface is certainly not smooth on a length scale greater than the facet size, then β can only be zero if the scattering between the (104) facets is completely incoherent. Next, the condition that I_{104} reflect the evolution of facet size and not facet structure requires F_{104}, the structure factor of the (104) CTR at one given point, to be unchanging. That is, the surface structure of the (104) facets must be constant. This condition is certainly met, since it is the growth of the extremely stable O/Cu(104) facets which drives the spinodal decomposition of the surface in the first place; the formation of intermediate structures on (104) facets would be difficult to reconcile with the present description of the faceting process.

As we argued above for the case of scaling of S_{104}/S_{115}, N_f and L_y change little in the later stages of faceting (due to the uniform faceting across the surface and to the anisotropic growth of the (104) facets, respectively). Therefore, it is reasonable that the growth of I_{104} scales as L_x^2, and the power-law exponents measured in Fig. 4.7 are thus equal to 2ϕ. The

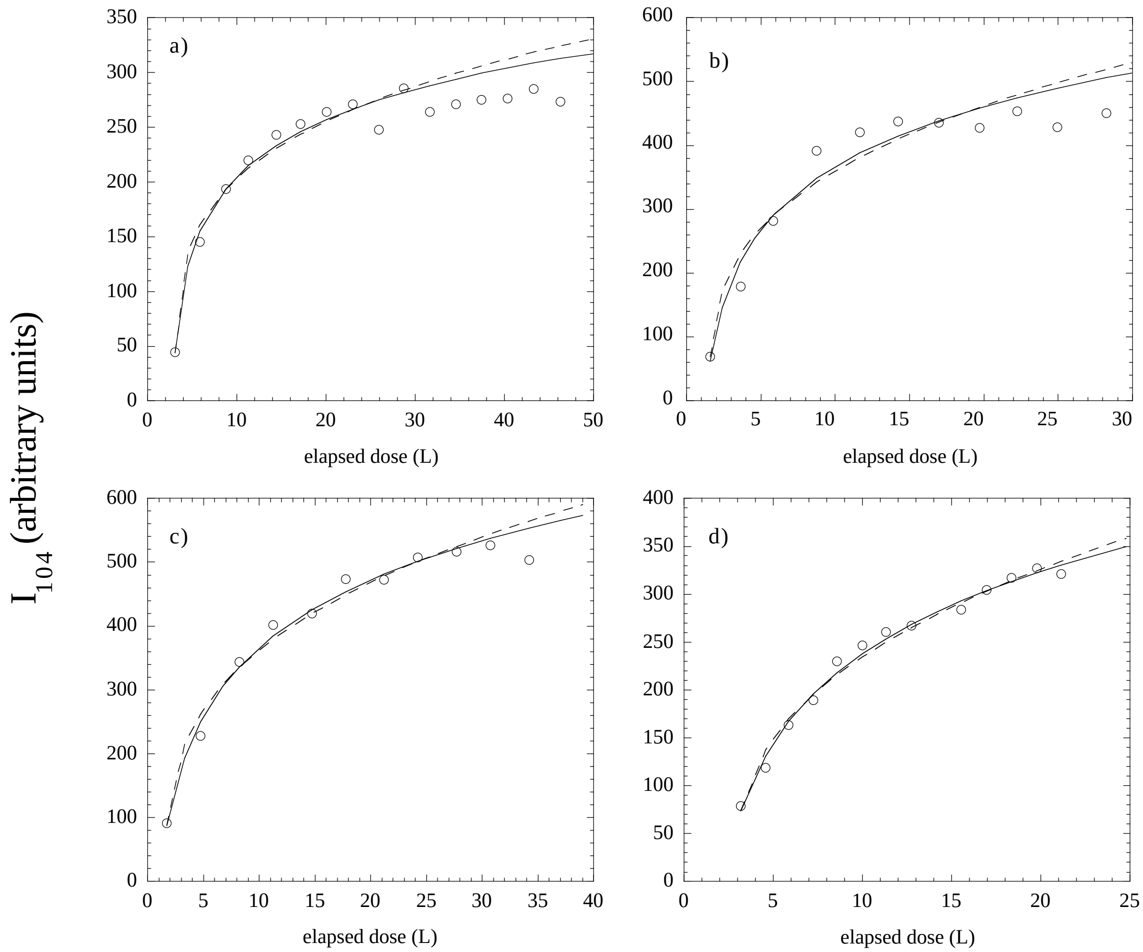

Figure 4.7: Variation of intensity from a point on a O/Cu(104) CTR during O_2 dosing, during experiments in the low- and middle-temperature regimes. Circles are measured intensities; solid and dashed lines are best fits to logarithmic and power-law scaling, respectively.
a) Dosing with $T = 222°$ C and $P_{O_2} = 7 \times 10^{-9}$ Torr. The resulting power-law fit (see text for interpretation) yields $2\phi = 0.25 \pm 0.03$.
b) $T = 252°$ C, $P_{O_2} = 6 \times 10^{-9}$ Torr; $2\phi = 0.32 \pm 0.06$.
c) $T = 260°$ C, $P_{O_2} = 8 \times 10^{-9}$ Torr; $2\phi = 0.33 \pm 0.03$.
d) $T = 340°$ C, $P_{O_2} = 3 \times 10^{-9}$ Torr; $2\phi = 0.38 \pm 0.03$.

average value of ϕ is, by this scaling method, 0.16, and the data may show a trend of ϕ increasing with temperature (but we note that the statistics are too limited to draw a strong conclusion there). The one experiment in which both S_{104}/S_{115} and I_{104} were measured gave a power-law fit with moderately comparable values of ϕ: 0.26 (Fig. 4.6b) vs. 0.19 (Fig. 4.7d) respectively. If we combine the results of the power-law scaling of S_{104}/S_{115} and I_{104}, then the best estimate of the exponent (given the limited range of dynamic scaling for each dosing experiment) is 0.17 ± 0.03. This low value is consistent with other faceting experiments [129, 116] performed on other, very different low-symmetry surfaces. We note, however, the difficulty in differentiating power-law scaling with small exponents from logarithmic scaling. While S_{104}/S_{115} scales very well as a logarithm, implying that L_x could as well, I_{104} vs. dose can not be fit as a logarithm squared, implying that either L_x does not exhibit logarithmic dynamic scaling, or that some of the assumptions in eq. 4.9 and its accompanying discussion are not justified. Logarithmic scaling would be consistent with one-dimensional diffusion [149] and with diffusion lengths which grow with the facet size [151], either of which could be expected for faceting on this vicinal surface.

To conclude, we have used surface x-ray diffraction to observe the process of oxygen-induced faceting of Cu(115) in real time, finding a dose of about 10 L initiates the spinodal decomposition of this surface into (104), (014), and $(11n)$ facets. We interpret the complex temperature dependence of the $(11n)$ facet evolution as due to changes in the relative surface free energies as a function of orientation, and thus present a temperature-dependent Wulff plot. The dynamic scaling of the facet lengths illustrates the similar manner in which the (104) facets grow, independent of the complexities of the Wulff plot along $(11n)$. The low symmetry of this faceted surface (i. e., three-sided facet pyramids with two crystallographically inequivalent sides) may not permit a direct comparison of these results to existing models and theories, but does present a case of adsorbate-induced faceting whose dynamics are consistent with theories which predict slow facet evolution.

References

[1] B. E. Warren, *X-ray Diffraction* (Dover, New York, 1990).

[2] *International Tables for Crystallography*, edited by A. J. C. Wilson (Kluwer Academic, Dordrecht, 1992).

[3] C. J. Sparks and J. L. Robertson, in *Resonant Anomalous X-ray Scattering*, edited by G. Materlik, C. J. Sparks, and J. L. Robertson (Elsevier Science, Amsterdam, 1994), p. 653.

[4] F. J. Walker, E. D. Specht, and R. A. McKee, Phys. Rev. Lett. **67**, 2818 (1991).

[5] E. D. Specht and F. J. Walker, Phys. Rev. B **47**, 13743 (1993).

[6] Y. S. Chu, H. You, J. A. Tanzer, T. E. Lister, and Z. Nagy, Phys. Rev. Lett. **83**, 552 (1999).

[7] G. M. Watson, D. Gibbs, G. H. Lander, B. D. Gaulin, L. E. Berman, H. Matzke, and W. Ellis, Phys. Rev. Lett. **77**, 751 (1996).

[8] S. Ferrer, P. Fajardo, F. de Bergevin, J. Alvarez, X. Torrelles, H. A. van der Vegt, and V. H. Etgens, Phys. Rev. Lett. **77**, 747 (1996).

[9] I. K. Robinson, Phys. Rev. B **33**, 3830 (1986).

[10] L. G. Parratt, Phys. Rev. **95**, 359 (1954).

[11] Y. P. Zhao, G.-C. Wang, and T.-M. Lu, Phys. Rev. B **55**, 13938 (1997).

[12] H. L. Meyerheim, I. K. Robinson, and R. Schuster, Surf. Sci. **370**, 268 (1997).

[13] Y. S. Chu, I. K. Robinson, and A. A. Gerwith, Phys. Rev. B **55**, 7945 (1997).

[14] I. K. Robinson, R. T. Tung, and R. Feidenhans'l, Phys. Rev. B **38**, 3632 (1988).

[15] P. H. Fuoss and I. K. Robinson, Nucl. Instrum. Methods B **222**, 171 (1984).

[16] W. R. Busing and H. A. Levy, Acta Cryst. **22**, 457 (1967).

[17] R. Fleming *et al.*, "Super" computer code, ©Bell Laboratories.

[18] I. K. Robinson, Rev. Sci. Instrum. **60**, 1541 (1989).

[19] E. Vlieg, J. F. van der Veen, J. E. Macdonald, and M. Miller, J. Appl. Cryst. **20**, 330 (1987).

[20] G. H. Vineyard, Phys. Rev. B **26**, 4146 (1982).

[21] M. Lohmeier and E. Vlieg, J. Appl. Cryst. **26**, 706 (1993).

[22] P. A. Bennett *et al.* (unpublished).

[23] M. J. Regan, E. H. Kawamoto, S. Lee, P. S. Pershan, N. Maskil, M. Deutsch, O. M. Magnussen, B. M. Ocko, and L. E. Berman, Phys. Rev. Lett. **75**, 2498 (1995).

[24] M. J. Regan, P. S. Pershan, O. M. Magnussen, B. M. Ocko, M. Deutsch, and L. E. Berman, Phys. Rev. B **54**, 9730 (1996).

[25] M. Zhao, D. S. Chekmarev, Z.-H. Cai, and S. A. Rice, Phys. Rev. E **56**, 7033 (1997).

[26] J. A. Morgan and G. M. Nathanson (unpublished).

[27] W. J. Huisman, J. F. Peters, M. J. Zwanenburg, S. A. de Vries, T. E. Derry, D. Abernathy, and J. F. van der Veen, Nature **390**, 379 (1997).

[28] J. Donohue, *The Structures of the Elements* (John Wiley & Sons, New York, 1974).

[29] X. Gong, G. L. Chairotti, M. Parrinello, and E. Tosatti, Phys. Rev. B **43**, 14277 (1991).

[30] O. Züger and U. Dürig, Phys. Rev. B **46**, 7319 (1992).

[31] M. Bernasconi, G. L. Chairotti, and E. Tosatti, Phys. Rev. Lett. **70**, 3295 (1993).

[32] M. Bernasconi, G. L. Chairotti, and E. Tosatti, Surf. Sci. **307-309**, 936 (1994).

[33] M. Bernasconi, G. L. Chairotti, and E. Tosatti, Phys. Rev. B **52**, 9988 (1995).

[34] M. Bernasconi, G. L. Chairotti, and E. Tosatti, Phys. Rev. B **52**, 9999 (1995).

[35] F. Laves, Z. Kristallog. **84**, 256 (1933).

[36] R. Powell, Proc. Roy. Soc. A **209**, 525 (1951).

[37] A. Defrain, J. Chim. Phys. **74**, 851 (1977).

[38] V. Heine, J. Phys. C **1**, 222 (1968).

[39] O. Hundery and R. Rydberg, J. Phys. F **4**, 2084 (1974).

[40] R. Kofman, P. Cheyssac, and J. Richard, Phys. Rev. B **16**, 5216 (1977).

[41] U. Häussermann, S. Simak, I. Abrikosov, and S. Lidin, Chem. Eur. J. **3**, 904 (1997).

[42] L. Bosio, J. Chem. Phys. **68**, 1221 (1978).

[43] P. Hofmann, Y. Cai, C. Grütter, and J. Bilgram, Phys. Rev. Lett. **81**, 1670 (1998).

[44] G. A. Somorjai and M. A. Van Hove, Prog. Surf. Sci. **30**, 201 (1989).

[45] T. N. Rhodin and G. Broden, Surf. Sci. **60**, 466 (1976).

[46] U. Bardi, Rep. Prog. Phys. **57**, 939 (1994).

[47] J. M. Carpinelli, H. W. Weitering, E. W. Plummer, and R. Stumpf, Science **381**, 398 (1996).

[48] H. Ibach, Surf. Sci. Repts. **29**, 193 (1997).

[49] F. Besenbacher and J. K. Nørskov, Prog. Surf. Sci. **44**, 5 (1993).

[50] R. Feidenhans'l, F. Grey, R. L. Johnson, S. Mochrie, J. Bohr, and M. Nielsen, Phys. Rev. B **41**, 5420 (1990).

[51] R. Feidenhans'l, F. Grey, M. Nielsen, F. Besenbacher, F. Jensen, E. Laegsgaard, I. Stensgaard, K. W. Jacobsen, J. K. Norskov, and R. L. Johnson, Phys. Rev. Lett. **65**, 2027 (1990).

[52] I. K. Robinson, E. Vlieg, and S. Ferrer, Phys. Rev. B **42**, 6954 (1990).

[53] W. Liu, K. C. Wong, H. C. Zeng, and K. A. R. Mitchell, Prog. Surf. Sci. **50**, 247 (1995).

[54] F. Jensen, F. Besenbacher, E. Lægsgaard, and I. Stensgaard, Surf. Sci. **259**, L774 (1991).

[55] F. Jensen, F. Besenbacher, and I. Stensgaard, Surf. Sci. **260/270**, 400 (1992).

[56] M. Polcik, J. Haase, M. Ondrejcek, and J. H. Petersen, Surf. Sci. **412/413**, 580 (1998).

[57] A. T. S. Wee, J. S. Foord, R. G. Egdell, and J. B. Pethica, Phys. Rev. B **58**, 7548 (1998).

[58] K. Morgenstern, H. Niehus, and G. Comsa, Surf. Sci. **338**, 1 (1995).

[59] Y. G. Shen, D. J. O'Connor, and K. Wandelt, Surf. Sci. **410**, 1 (1998).

[60] C. Ammer, K. Meinel, H. Wolter, and H. Neddermeyer, Surf. Sci. **401**, 138 (1998).

[61] G. Witte, J. Braun, D. Nowack, L. Bartels, B. Neu, and G. Meyer, Phys. Rev. B **58**, 13224 (1998).

[62] W. Berndt, Z. Naturforsch. **22a**, 1655 (1967).

[63] L. Trepte, C. Menzel-Kopp, and E. Menzel, Surf. Sci. **8**, 223 (1967).

[64] J. Perdereau and G. E. Rhead, Surf. Sci. **24**, 555 (1971).

[65] E. Legrand-Bonnyns and A. Ponslet, Surf. Sci. **53**, 675 (1975).

[66] J. C. Boulliard, C. Cohen, J. L. Domange, A. V. Drigo, A. L'Hoir, J. Moulin, and M. Sotto, Phys. Rev. B **30**, 2470 (1984).

[67] J. C. Boulliard, J. L. Domange, and M. Sotto, Surf. Sci. **165**, 434 (1986).

[68] G. W. Lloyd and D. P. Woodruff, Surf. Sci. **285**, L503 (1993).

[69] S. Reiter and E. Taglauer, Surf. Sci. **367**, 33 (1996).

[70] P. J. Knight, S. M. Driver, and D. P. Woodruff, J. Phys.: Condens. Matter **9**, 21 (1997).

[71] M. Sotto, Surf. Sci. **260**, 235 (1992).

[72] S. Reiter and E. Taglauer, Surf. Rev. Lett. **4**, 1325 (1997).

[73] B. Lang, R. W. Joyner, and G. A. Somorjai, Surf. Sci. **30**, 454 (1972).

[74] Z.-J. Tian and T. S. Rahman, Phys. Rev. B **47**, 9751 (1993).

[75] S. Durukanoglu, A. Kara, and T. S. Rahman, Phys. Rev. B **55**, 13894 (1997).

[76] H.-J. Ernst, R. Folkerts, and L. Schwenger, Phys. Rev. B **52**, 8461 (1995).

[77] M. A. Albrecht, R. Blome, H. L. Meyerheim, W. Moritz, I. K. Robinson, and D. A. Walko (unpublished).

[78] B. Loisel, D. Gorse, V. Pontikis, and J. Lapujoulade, Surf. Sci. **221**, 365 (1989).

[79] K. D. Hammonds and R. M. Lynden-Bell, Surf. Sci. **278**, 437 (1992).

[80] I. Y. Sklyadneva, G. G. Rusina, and E. V. Chulkov, Surf. Sci. **416**, 17 (1998).

[81] G. Witte, J. Braun, A. Lock, and J. P. Toennies, Phys. Rev. B **52**, 2165 (1995).

[82] J. S. Pedersen, Surf. Sci. **210**, 238 (1989).

[83] P. N. Keating, Phys. Rev. **145**, 637 (1966).

[84] S. Wei and M. Y. Chou, Phys. Rev. B **50**, 4859 (1994).

[85] K. A. Thompson and C. S. Fadley, Surf. Sci. **146**, 281 (1984).

[86] A. J. Algra, E. Suurmeijer, and A. L. Boers, Surf. Sci. **128**, 207 (1983).

[87] C. Cohen, A. L'Hoir, J. Moulin, D. Schmaus, M. Sotto, J.-L. Domange, and J.-C. Boulliard, Surf. Sci. **339**, 41 (1995).

[88] K. W. Jacobsen and J. K. Nørskov, Phys. Rev. Lett. **65**, 1788 (1990).

[89] R. H. Milne, Surf. Sci. **121**, 347 (1982).

[90] S. S. Fu and G. A. Somorjai, Surf. Sci. **262**, 68 (1992).

[91] E. Vlieg *et al.*, unpublished.

[92] M. Flytzani-Stephanopoulos and L. D. Schmidt, Prog. Surf. Sci. **9**, 83 (1979).

[93] J. Falta, R. Imbihl, and M. Henzler, Phys. Rev. Lett. **64**, 1409 (1990).

[94] G. A. Somorjai, J. Mol. Catal. A **107**, 39 (1996).

[95] V. P. Zhdanov and B. Kasemo, Phys. Rev. Lett. **81**, 2482 (1998).

[96] S. Johansson, K. Wong, V. P. Zhdanov, and B. Kasemo, J. Vac. Sci. Tech. A **17**, 297 (1999).

[97] P. Marcus, Electrochimica Acta **43**, 109 (1998).

[98] H. Schubert, U. Tegtmeyer, D. Herein, X. Bao, M. Muhler, and R. Schlögel, Catal. Lett. **33**, 305 (1995).

[99] A. Berkó, G. Ménesi, and F. Solymosi, J. Phys. Chem. **100**, 17732 (1996).

[100] H. Graoui, S. Giorgio, and C. R. Henry, Surf. Sci. **417**, 350 (1998).

[101] M. Wortis, in *Chemistry and Physics of Solid Surfaces VII*, edited by R. Vanselow and R. Howe (Springer-Verlag, Berlin, 1988), p. 367.

[102] N. A. Gjostein, Acta Metall. **11**, 957 (1963).

[103] N. A. Gjostein, Acta Metall. **11**, 969 (1963).

[104] A. Shi, Phys. Rev. B **36**, 9068 (1987).

[105] J. K. Nørskov, Rep. Prog. Phys. **53**, 1253 (1990).

[106] G. R. Darling and S. Holloway, Rep. Prog. Phys. **58**, 1595 (1995).

[107] J. L. Whitten and H. Yang, Surf. Sci. Repts. **24**, 55 (1996).

[108] M. Papoular, Europhys. Lett. **33**, 211 (1996).

[109] J. C. Tracy and J. M. Blakely, Surf. Sci. **13**, 313 (1968).

[110] J. S. Ozcomert, W. W. Pai, N. C. Bartelt, and J. E. Reutt-Robey, Phys. Rev. Lett. **72**, 258 (1994).

[111] R. J. Phaneuf and E. D. Williams, Phys. Rev. Lett. **58**, 2563 (1989).

[112] J. Wei, X. S. Wang, N. C. Bartelt, E. D. Williams, and R. T. Tung, J. Chem. Phys. **94**, 8384 (1991).

[113] G. E. Poirier, B. K. Hance, and J. M. White, J. Vac. Sci. Tech. B **10**, 6 (1992).

[114] W. Weiss, K. Kasper, K. H. Herrmann, D. Schmeisser, and W. Gopel, Surf. Sci. **268**, 319 (1992).

[115] J. R. Heffelfinger, M. W. Bench, and C. B. Carter, Surf. Sci. **343**, L1161 (1995).

[116] J. R. H. C. B. Carter, Surf. Sci. **389**, 188 (1997).

[117] R. J. Phaneuf, N. C. Bartelt, E. D. Williams, W. Swiech, and E. Bauer, Phys. Rev. Lett. **67**, 2986 (1991).

[118] M. Horn-von Hoegen, F. J. M. Z. Heringdorf, D. Kahler, T. Schmidt, and E. Bauer, Thin Solid Films **336**, 16 (1998).

[119] G. Comsa, G. Mechtersheimer, and B. Poelsema, Surf. Sci. **119**, 159 (1982).

[120] C. Voss and N. Kruse, Surf. Sci. **409**, 252 (1998).

[121] V. K. Medvedev, Y. Suchorski, C. Voss, T. Visart de Bocarme, T. Bär, and N. Kruse, Langmuir **14**, 6151 (1998).

[122] K. Pelhos, T. E. Madey, and R. Blaszczyszyn, Surf. Sci. **426**, 61 (1999).

[123] B. M. Ocko and S. G. J. Mochrie, Phys. Rev. B **38**, 7378 (1988).

[124] Q. Shen, J. P. Chang, G. Navrotski, and J. Blakely, Phys. Rev. Lett. **64**, 451 (1990).

[125] G. M. Watson, D. Gibbs, D. M. Zehner, M. Yoon, and S. G. J. Mochrie, Phys. Rev. Lett. **71**, 3166 (1993).

[126] M. Yoon, S. G. J. Mochrie, D. M. Zehner, G. M. Watson, and D. Gibbs, Surf. Sci. **338**, 225 (1995).

[127] G. M. Watson, D. Gibbs, S. Song, A. R. Sandy, S. G. J. Mochrie, and D. M. Zehner, Phys. Rev. B **52**, 12329 (1995).

[128] G. M. Watson, D. Gibbs, D. M. Zehner, M. Yoon, and S. G. J. Mochrie, Surf. Sci. **407**, 59 (1998).

[129] S. Song, S. G. J. Mochrie, and G. B. Stephenson, Phys. Rev. Lett. **74**, 5240 (1995).

[130] S. Song, M. Yoon, S. G. J. Mochrie, G. B. Stephenson, and S. T. Milner, Surf. Sci. **372**, 37 (1997).

[131] M. Yoon, S. G. J. Mochrie, M. W. Tate, S. M. Gruner, and E. F. Eikenberry, Surf. Sci. **411**, 70 (1998).

[132] A. J. Steinfort, P. M. L. O. Scholte, A. Ettema, F. Tuinstra, M. Nielsen, E. Landemark, D.-M. Smilgies, R. Fiedenhans'l, G. Falkenberg, L. Seehofer, and R. L. Johnson, Phys. Rev. Lett. **77**, 2009 (1996).

[133] M. Nielsen, D.-M. Smilgies, R. Fiedenhans'l, E. Landemark, G. Falkenberg, L. Lottermoser, L. Seehofer, and R. L. Johnson, Surf. Sci. **352-354**, 430 (1996).

[134] F. B. Rasmussen, J. Baker, M. Nielsen, R. Fiedenhans'l, and R. L. Johnson, Phys. Rev. Lett. **79**, 4413 (1997).

[135] E. Lundgren, J. Alvarez, X. Torrelles, K. F. Peters, H. Isern, and S. Ferrer, Phys. Rev. B **59**, 2431 (1999).

[136] G. Wulff, Z. Krist. **34**, 449 (1901).

[137] H. P. Bonzel and K. Dueckers, in *Chemistry and Physics of Solid Surfaces VII*, edited by R. Vanselow and R. Howe (Springer-Verlag, Berlin, 1988), p. 429.

[138] E. D. Williams and N. C. Bartelt, Ultramicroscopy **31**, 36 (1989).

[139] J. W. Cahn, Acta Met. **10**, 179 (1962).

[140] C. Herring, Phys. Rev. **82**, 87 (1951).

[141] J. W. Cahn and J. E. Hilliard, J. Chem. Phys. **31**, 688 (1959).

[142] J. Stewart and N. Goldenfeld, Phys. Rev. A **46**, 6505 (1992).

[143] M. Touzani and M. Wortis, Phys. Rev. B **36**, 3598 (1987).

[144] A. Shi and M. Wortis, Phys. Rev. B **37**, 7793 (1988).

[145] J. W. M. Frenken and P. Stoltze, Phys. Rev. Lett. **82**, 3500 (1999).

[146] W. W. Mullins, J. Appl. Phys. **30**, 77 (1959).

[147] W. W. Mullins, Phil. Mag. **6**, 1313 (1961).

[148] J. D. Shore, M. Holzer, and J. P. Sethna, Phys. Rev. B **46**, 11376 (1992).

[149] F. Liu and H. Metiu, Phys. Rev. B **48**, 5808 (1993).

[150] D. G. Vlachos, L. D. Schmidt, and R. Aris, Phys. Rev. B **47**, 4896 (1993).

[151] J. D. Shore and D. J. Bukman, Phys. Rev. E **51**, 4196 (1995).

[152] H. Jeong and J. D. Weeks, Phys. Rev. B **57**, 3939 (1998).

[153] M. Drechsler, Surf. Sci. **266**, 1 (1992).

[154] J. C. Boulliard and M. P. Sotto, Surf. Sci. **177**, 139 (1986).

[155] H. Jeong and J. D. Weeks, Surf. Sci. **432**, 101 (1999).

[156] E. Taglauer, S. Reiter, A. Liegl, and S. Schoemann, Nucl. Instrum. Meth. B **118**, 456 (1996).

[157] L. Schwenger, R. L. Folkerts, and H.-J. Ernst, Phys. Rev. B **55**, 7406 (1997).

[158] I. K. Robinson, K. H. Whiteaker, and D. A. Walko, Physica B **221**, 70 (1996).

[159] N. Cabrera, in *Symposium on Properties of Surfaces* (ASTM, Philadelphia, 1963), p. 24.

Vita

Donald Alan Walko was born on December 28, 1970, in Schenectady, New York, to Steven and Ruth Walko. He graduated from Shenendehowa High School in June 1989 as salutatorian, entering Cornell University the following fall. While at Cornell, he spent the fall of 1991 and the following summer as an engineering co-op student at Oak Ridge National Lab, Oak Ridge, TN. There he worked in the Metals and Ceramics Division with Dr. Eliot Specht, Dr. Cullie Sparks, Dr. Fred Walker, and Dr. Rodney McKee. His projects included measurement, analysis, and interpretation of surface x-ray reflectivity of Cr-implanted sapphire; interpretation of alloy powder diffraction patterns; and investigation of equilibrium energies and interfacial structures of thin, epitaxial oxide films for use as waveguides. Don graduated from Cornell in May 1993, earning a Bachelors of Science with Distinction from the College of Engineering, and winning the Paul Hartman Prize in Experimental Physics.

Following graduation, Don worked at the Cornell High Energy Synchrotron Source. In collaboration with Dr. Sarvjit Shastri, Dr. Ken Finkelstein, Dr. Qun Shen, and Prof. Bob Batterman, he helped design and carry out an experiment to produce and characterize elliptically polarized x rays using perfect crystal optics. This experiment was performed with radiation from the CHESS-APS undulator.

Don then attended the University of Illinois at Urbana-Champaign as a graduate student in the Department of Physics. From August 1993 to May 1994, and from January 1997 to May 1997, he was a graduate teaching assistant for discussion and lab sections of introductory physics courses. In October 1994, Don received the Masters of Science degree in physics from the University of Illinois. Since May 1994, Don has been a graduate research assistant working with Professor Ian K. Robinson in the Materials Research Laboratory. Don has participated in many surface x-ray diffraction experiments in this time, which were performed at the National Synchrotron Light Source, Brookhaven National Laboratory, New York. A list of published articles and talks presented at conferences is listed below. Also during this time, Don was award a Graduate Assistant in an Area of National Need (GAANN) fellowship from the Department of Physics for August 1996 to July 1997.

Don has been a member of the InterVarsity Christian Fellowship chapters of his undergraduate and graduate schools, having served as a small group Bible study leader and on the executive committee. Don is also an accomplished intramural referee, having won awards in several sports for his officiating.

Publications

D. A. Walko and I. K. Robinson, "Structure of Cu(115): Clean surface and its oxygen-induced facets structure of α-Ga(010)," Physical Review B vol. 59, p. 15446 (1999).

D. A. Walko, I. K. Robinson, Ch. Grütter, and J. H. Bilgram, "Surface structure of α-Ga(010)," Physical Review Letters vol. 81, p. 626 (1998).

Chinkyo Kim, D. A. Walko, and I. K. Robinson, "Refined structure of $(\sqrt{3} \times \sqrt{3})$ Sb/Si(111)," Surface Science vol. 388, p. 242 (1997).

I. K. Robinson, K. L. Whiteaker, and D. A. Walko, "Cu island growth on Cu(110)," Physica B vol. 221, p. 70 (1996).

S. D. Shastri, K. D. Finkelstein, Qun Shen, B. W. Batterman, and D. A. Walko, "Undulator test of a Bragg reflection elliptical polarizer at $\sim$ 7.1 keV," Review of Scientific Instruments vol. 66, p. 1581 (1995).

E. D. Specht, D. A. Walko, and S. J. Zinkle, "Amorphization of Al_2O_3 by ion induced density reduction," Nuclear Instruments and Methods in Physics Research B vol. 84, p. 323

(1994).

Conferences

D. A. Walko and I. K. Robinson, “Surface structure of α-Ga(010),” Physical Electronics Conference (State College, PA, 1998).

D. A. Walko, I. K. Robinson, Ch. Grütter, and J. H. Bilgram, “Surface structure of α-Ga(001),” Bulletin of the American Physical Society vol. 42, #1, p. 136 (Kansas City, 1997).

D. A. Walko, K. L. Whiteaker, and I. K. Robinson, “Scaling of submonolayer Cu islands grown on Cu(110),” International Union of Crystallography (Seattle, 1996).

D. A. Walko, “Characterizing ion-implanted crystals with x-ray reflectivity,” Sixth National Conference on Undergraduate Research (Minneapolis, 1992).

Proceedings/Activity Reports

D. A. Walko and I. K. Robinson, “Evolution of O-induced facet formation on Cu(115),” NSLS Activity Report (1997).

P. A. Bennett, I. K. Robinson and D. A. Walko, “Formation of copper silicide using surface x-ray diffraction,” NSLS Activity Report (1997).

G. Glass, I. K. Robinson, D. A. Walko, and J. E. Greene, “Ultra-high doping in Si(001): B pairing and diffusion,” NSLS Activity Report (1997).

D. A. Walko, I. K. Robinson, Ch. Grütter, and J. H. Bilgram, “Surface structure of α-Ga(001),” NSLS Activity Report (1996).

I. K. Robinson, D. A. Walko, H. L. Meyerheim, and M. Albrecht, “Oxygen-induced faceting of Cu(115),” NSLS Activity Report (1996).

P. A. Bennett, D. A. Walko, and I. K. Robinson, “Structure of the incommensurate Au/Si(100)-5×1 surface,” NSLS Activity Report (1996).

D. A. Walko, K. L. Whiteaker, and I. K. Robinson, "Growth of Cu islands on Cu(110)," NSLS Activity Report (1995).

Chinkyo Kim, D. A. Walko, and I. K. Robinson, "Sb/Si(111) $(\sqrt{3} \times \sqrt{3})R\,30^\circ$ structure determination," NSLS Activity Report (1995).

B. W. Batterman, K. D. Finkelstien, S. D. Shastri, Q. Shen and D. A. Walko, "The production and Application of elliptically polarized x rays derived from a standard undulator," Bulletin of the American Physical Society vol. 39, #1, p. 530 (Pittsburgh, 1994).

E. D. Specht, D. A. Walko, and S. J. Zinkle, "Density reduction: a mechanism for amorphization at high ion doses," Materials Research Society Symposium Proceedings vol. 321, p. 399 (1994).

R. A. McKee, F. J. Walker, E. D. Specht, and D. A. Walko, "Layer-by-layer strain relief for the growth of alkaline earth oxides on Si(001)," Materials Research Society (1993).